PONTIFÍCIA UNIVERSIDADE CATÓLICA
DO RIO DE JANEIRO

Eduardo Enes Cota

Toughness Evaluation and Fracture Predictions in Elastoplastic Materials

Dissertação de Mestrado

Dissertation presented to the Programa de Pós–graduação em Engenharia Mecânica da PUC-Rio in partial fulfillment of the requirements for the degree of Mestre em Engenharia Mecânica.

Advisor: Prof. Jaime Tupiassú Pinho de Castro

Rio de Janeiro
February 2019

Eduardo Enes Cota

Toughness Evaluation and Fracture Predictions in Elastoplastic Materials

Dissertation presented to the Programa de Pós–graduação em Engenharia Mecânica da PUC-Rio in partial fulfillment of the requirements for the degree of Mestre em Engenharia Mecânica. Approved by undersigned Examination Committee.

Prof. Jaime Tupiassú Pinho de Castro
Advisor
Departamento de Engenharia Mecânica – PUC-Rio

Prof. Marco Antonio Meggiolaro
Departamento de Engenharia Mecânica – PUC-Rio

Prof. Gustavo Henrique Bolognesi Donato
Centro Universitário – FEI

Rio de Janeiro, February 21st, 2019

Eduardo Enes Cota

The former author graduated in Mechanical Engineering from Pontifícia Universidade Católica do Rio de Janeiro in 2015

Acknowledgement

First of all, I would like to thank my advisor Prof. Jaime Tupiassú Pinho de Castro for the opportunity, motivation, and guidance during my thesis.

To Prof. Marco Antonio Meggiolaro, Prof. Gustavo Donato, and Prof. Luis Fernando Martha for the interest in the work and the given advice.

To Prof. Ivan Menezes and Prof. José Freire for all the support.

To my friends from the university João Carlos Virgolino, Rodrigo Bianchi, Thiago Almeida, Bruno Calasans, and André Xavier.

To my friends from childhood Bruno Fraga, Ian Lange, José Ricardo Garcia, and Raul Valverde.

To Jullian, Gean, Adrian, Elias, and Euclides for all the help during my experiments at the laboratories.

To Rodrigo Landin for the specimens machining.

To CNPq for financial support.

To USIMINAS for supplying the material used in the experiments.

To my colleagues and relatives that somehow helped me during this time. I would also like to do a special thanks to my parents Manuel Julio José Cota Janeiro, and Rosa Claudia Garrido Enes Cota for all the support and inspiration. Also, to my sister Larissa, and to my brothers Victor and Raphael Enes Cota.

Abstract

Enes Cota, Eduardo; Tupiassú Pinho de Castro, Jaime (Advisor). **Toughness Evaluation and Fracture Predictions in elastic- plastic Materials**. Rio de Janeiro, 2019.110p. Dissertação de mestrado – Departamento de Engenharia Mecânica, Pontifícia Universidade Católica do Rio de Janeiro.

Understanding how to analyze cracks is essential for the petrochemical industry to avoid accidents or incidents in a safe and economical way. Structural Integrity standards provide conservative procedures to assess the actual strength of cracked components like pipes and pressure vessels. Therefore, critical loads predictions were computed on a plate with a through-wall crack following level 2 and 3 of the fitness-for-service guide API 579. For comparison, experimental tests were performed to evaluate the standard conservatism on a ductile tearing type of failure. Furthermore, the fracture toughness of the steel was measured through standard J_{Ic} tests and material's resistance curves (J-R curve). The technique used during the fracturing process was the elastic compliance method with unloading/reloading sequences. Additionally, the effects of the specimen's geometry and the type of loading, which can significantly change the value of its toughness, were also analyzed using concepts of elastoplastic fracture mechanics. The material used in this work was the API 5L X80, which is a High Strength Low Alloy (HSLA) dual-phase steel developed for deepwater pipelines. The fracture toughness measurement tests using SE(B) specimens, which have a medium-to-high plastic constraint, followed the ASTM E1820-17 procedures. The experiments with SE(T) specimens, which present a low plastic restriction, considered literature procedures.

Keywords

Fracture Mechanics; EPFM; API 5L X80; Toughness; ASTM E1820; Structural Integrity; API 579

Resumo

Enes Cota, Eduardo; Tupiassú Pinho de Castro, Jaime (Advisor). **Avaliação da Tenacidade e Previsões de Fraturas em Materiais Elastoplásticos**. Rio de Janeiro, 2019.110p. Dissertação de mestrado – Departamento de Engenharia Mecânica, Pontifícia Universidade Católica do Rio de Janeiro.

Compreender como analisar trincas é essencial para a indústria petroquímica evitar qualquer incidente de uma forma econômica. Normas de Integridade Estrutural fornecem procedimentos conservadores para avaliar componentes trincados como tubulações e vasos de pressão. Portanto, previsões de cargas criticas foram calculadas assumindo uma placa com trinca passante seguindo procedimentos dos níveis 2 e 3 da API 579. Para comparação, testes experimentais foram realizados para avaliar o conservatismo da norma em falha por rasgamento dúctil. Além disso, a tenacidade à fratura foi medida por meio do J_{Ic} e curva $J\text{-}R$. A técnica usada durante o processo de fratura foi o método de flexibilidade elástica com descarregamento e carregamentos sequenciais. Adicionalmente, efeito de geometria e tipo de carregamento, os quais possuem grande influência nas medições de tenacidade, também foram avaliados usando conceitos da mecânica da fratura elastoplástica. O material utilizado nesse trabalho foi o API 5L X80, que é um aço de Alta Resistencia e Baixa Liga (ARBL) bifásico desenvolvido para tubulações aplicáveis em aguas profundas. Os ensaios experimentais de medição de tenacidade usando corpos de prova SE(B), que possuem média-alta restrição plástica, foram testados seguindo procedimentos da ASTM E1820-17. Já os experimentos usando corpos de prova SE(T), que possuem baixa restrição plástica, foram realizados considerando procedimentos da literatura.

Palavras-chave

Mecânica da Fratura; MFEP; API 5L X80; Tenacidade; ASTM E1820; Integridade Estrutural; API 579

Table of contents

List of figures

List of tables

Nomenclature

Δa crack extension

Δa_{ic} crack extension at the initiation of ductile crack growth

δ crack tip opening displacement

δ_c crack tip opening displacement at unstable crack extension

δ_{Ic} crack tip opening displacement at stable crack extension

Γ path integral contour

$\mathcal{G}$ Griffith energy release rate

$\mathcal{G}_{Ic}$ Griffith energy release rate at stable crack extension

Φ plasticity interaction factor

σ_b bending stress

σ_f critical stress

σ_m membrane stress

σ_n nominal stress

σ_Y effective yield stress

σ_{ij} stress tensor

σ_{ref} reference stress

σ_{us} ultimate strength

σ_{ys} yield strength

υ Poisson ratio

a crack size

a_{oq} initial crack size

A	area
A_{pl}	plastic area
B_e	effective thickness
B_N	side groove thickness
b	remaining ligament
b_o	original remaining ligament
C	unloading compliance
E	Young's modulus
E_p	stored elastic energy and work done by external loads
E_T	potential energy
f_w	finite width correction factor
H	Distance between loading points on SE(T) specimens
J	J-Integral, energy release rate
J_c	J-Integral at instability with significant stable crack extension
J_u	J-Integral at instability without significant stable crack extension
J_{Ic}	J-Integral at the initiation of ductile crack growth
K	stress intensity factor
K_t	stress concentration factor
K_{Ic}	critical stress intensity factor in mode I
K_{JIc}	stress intensity factor in mode I corresponding to J_{Ic}
K_I^P	primary stress intensity factor
K_I^{SR}	secondary and residual stress intensity factor
L	length
L_r	load ratio

P	load
P_m	maximum fatigue load
P_Y	effective yield load
R	fatigue load ratio
r	radius
S	support span
T_i	component traction vector
U	strain energy density
u	normalized unloading compliance
u_i	displacement vector components
W	width
W_s	energy required to create new crack surface

1.
Introduction

Engineering structures can fail under service loads due to damage caused by several mechanisms such as corrosion, creep, fatigue, plastic collapse, and/or fracture. The consequences of such structural failures can be catastrophic, with the loss of significant amounts of money, and sometimes even of lives. Most of these failures are caused or much affected by cracks, which can grow until they break the component unless properly repaired in due time. Hence, to prevent structural failures, it is essential to analyze crack effects by understanding the concepts of Fracture Mechanics and by using them to answer the following questions [1].

- What is the critical crack size?

- How long does it take to reach the critical size?

- What is the residual strength of the structure as a function of the crack size?

- Will crack growth stop?

- What is the proper inspection frequency?

- What is the admissible initial flaw size the structure can safely tolerate at the start of its service life?

Fracture Mechanics is the field of study that deals with the effects of cracks on fracture behavior of a given structure. Such effects depend on stress levels, crack sizes, and material properties, as well as on the mechanism(s) that drive the fracture [2]. It is divided into two domains, Linear Elastic Fracture Mechanics (LEFM), suitable for modeling brittle fractures. And Elastoplastic Fracture Mechanics (EPFM), needed to model ductile structural components. The main difference between these groups is the relative size of the plastic zone in front of the crack tip. If the plastic zone has a negligible size in relation to the component's dimensions, it is possible to use LEFM concepts. Otherwise,

it is necessary to use EPFM procedures. Moreover, if the plastic zone runs through the entire residual ligament of the component, the failure mechanism is ductile overload. In other words, plastic collapse [3]. Fig. 1.1 shows a schema of the failure behavior of a plate with a central crack under tension, indicating which methodology to use, depending on the size of the plastic zone.
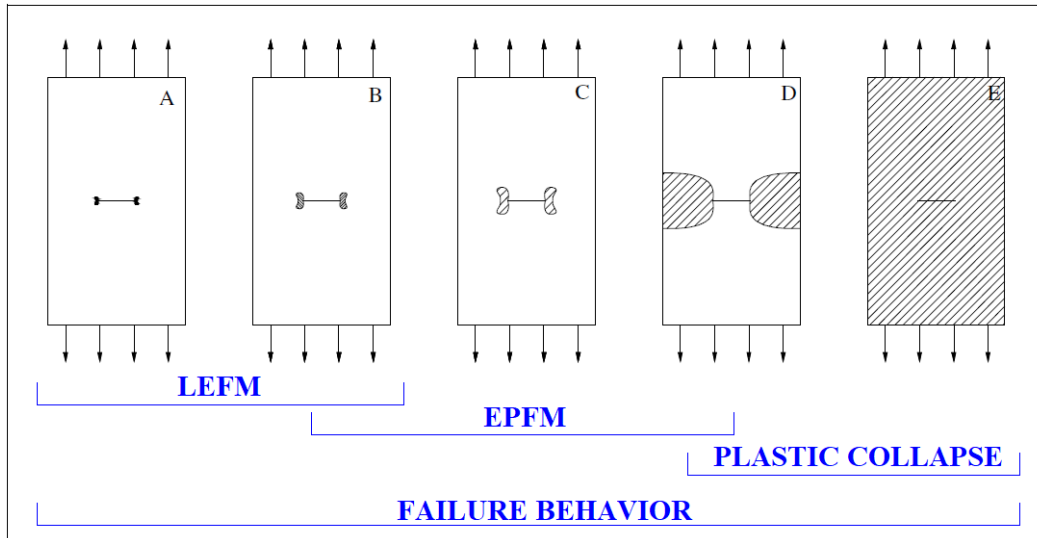
Figure 1.1: Failure behavior [4].

The most important material property for Fracture Mechanics purposes is the fracture toughness, which quantifies the crack resistance of a material, or its capacity to tolerate cracks without fracturing [4]. In LEFM, the toughness, or the resistance to brittle fractures, can be quantified by the critical stress intensity factor K_{Ic}, or by the equivalent critical value of the strain energy release rate (or the crack driving force) G_{Ic}. In EPFM, fracture toughness can be quantified e.g. by the energy required to initiate ductile crack growth J_{Ic}, the elastoplastic (EP) version of G_{Ic}. Using these properties, engineers can select the material(s) for the construction of the structure(s), or evaluate the effect of any cracks found in their structures. However, EP fracture toughness measurements must be used with great care since they are not mechanical properties. Indeed, the actual toughness of a given structural component it can vary a lot depending on its geometry and on the type of load applied to it, as well as on the type of material. In any way, it is recommended to follow standardized procedures to measure fracture toughness, for instance ASTM E399 [5], ASTM E1290 [6], ASTM E1820 [7], BS 7448 [8], or EFAM GTP [9].

The American Society for Testing and Materials (ASTM) issued its E1820 standard to provide normalized procedures to measure fracture toughness both in LEFM and EPFM conditions. Among these procedures, it is possible to measure the linear-elastic parameter K_{Ic}, and the elastoplastic parameters J_{Ic}, J_u, J_c, δ_c, *J-R* and δ*-R* curves based on SE(B), C(T), and DC(T) specimens [10]. The basic procedure for measuring J_{Ic} requires multiple specimens to evaluate a single parameter. Another procedure uses the elastic compliance technique that can generate an entire *J*-resistance or *J-R* curve from unloading/reloading sequences during the fracturing process (see chapter 3.1.2). This procedure deserves attention, because it uses a single specimen on the test, resulting in a significant economy of time and material.

The SE(B), C(T), and DC(T) specimens recommended by the standard are highly constrained. In other words, they inhibit plastic deformation in front of the crack tip, due to the highly triaxial stress state acting there. Hence, they guarantee or tend to characterize plane strain conditions around the crack tip. Because of that, a material that in theory is ductile may present a more brittle behavior in that region, resulting in lower values of its measured fracture toughness, a safety requirement for most structural design applications. However, some engineering structures such as pipelines and pressure vessels work under much lower constraint conditions, making the standard conservative, but also leading to uneconomic designs. With this in mind, the clamped SE(T) specimen provides more similar constraints conditions when compared with pipelines and pressure vessels [11]. This specimen generally develops lower stress triaxiality in front of the crack tip when compared to SE(B), C(T), and DC(T) specimens.

It is basically impossible to claim that structures do not have any flaw, especially when they work under variable loadings in long-term operations. Therefore, it is necessary to check if the structure can operate under the presence of any flaw. For that reason, groups of engineers came together to develop accurate assessments of Structural Integrity for safety analysis of engineering structures, which include pipelines and pressure vessels, for example. The American Petroleum Institute (API) developed its API-579 Fitness-For-Service (FFS) guide [12], which recommends engineering procedures for structural

integrity evaluations on the petrochemical industry. The primary objective of the FFS assessment is to prevent failures. There are other similar standards like the R6 [13], SAQ [14], SINTAP [15], and BS7910 [16], which also issue recommended procedures to evaluate crack effects in structures. Chapter 1.1 shows some examples of disasters caused by cracks in real life.

1.1
Disasters

One of the biggest disasters in the world was at Umm Said NGL Plant in 1977, where a tank containing about 236,000 barrels of refrigerated propane at -44°C failed massively at one of its welds. Experts found that corrosion led to the weld failure due to sulfates that remained inside the tank after a routine hydrostatic test with seawater. The wave of liquid propane swept over the dikes and inundated the process area before igniting. A nearby tank containing 125,000 barrels of refrigerated butane and most of the process area were also destroyed. Figure 1.2 shows how serious the incident was. Six people died, and the damaged properties losses were estimated at 76 million USD (1977).
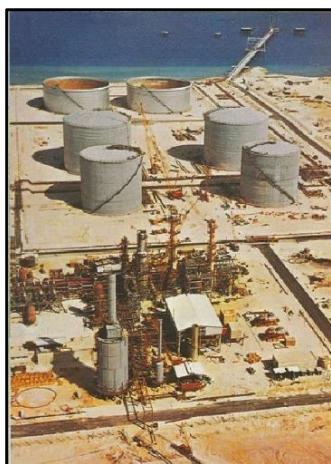
1.2(a): Before   1.2(b): After

Figure 1.2: Umm Said NGL Plant [17].

Another serious incident was a Norwegian semi-submersible oil drilling platform called Alexander L. Kielland, which capsized during a storm in the Ekofisk oil field in March 1980. An investigative report concluded that a fatigue crack had propagated from the double fillet near the hydrophone mounted to

one of the horizontal bracing, which connected the collapsed D-leg to the rest of the rig (see Fig. 1.3). Besides that, lamellar tearing was found in the flange plate and cold cracks in the butt weld. This was the worst disaster in Norwegian waters since World War II, with 123 deaths.
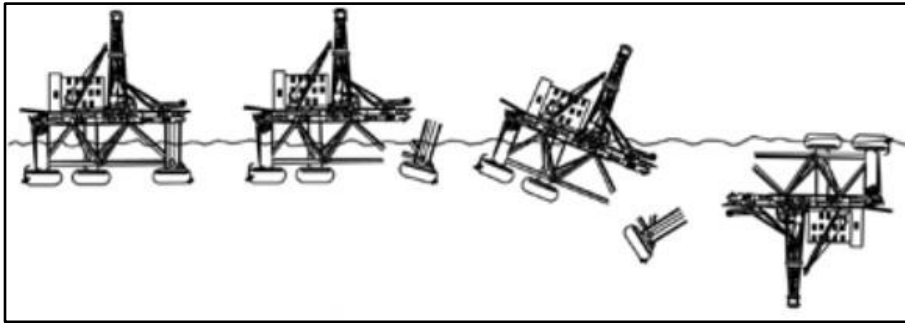
1.3(a): Process of capsize.
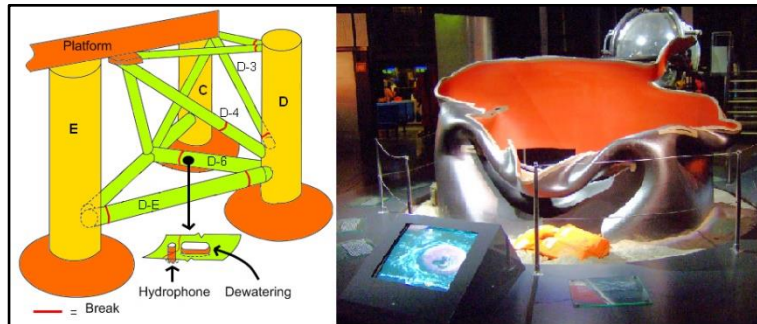
1.3(b): Fracture on the rig.   1.3(c): Part of the bracing that failed.

Figure 1.3: Alexander L. Kielland platform failure [18].

The Liberty ships failures were one of the driving forces for modern fracture mechanics studies. Between the years 1939 and 1945, 2708 such ships were built to fight in World War II. Eventually, 1038 serious incidents or accidents were reported in those ships by April 1946. Fig. 1.4 shows the Schenectady ship that broke in two in calm waters. The failure was caused by a brittle fracture that started at a welded joint, because of the low temperatures and the fault manufacturing process used to build that ship during the early war period. To weld the sections, e.g., they used a methodology that was still in the developing stage at that time. Even though full of defects, the welds were much faster than the previous rivets used in naval construction, a most important requirement in wartime, but they made the ship's structure to be continuous, which allowed the crack to propagate freely once becoming unstable.
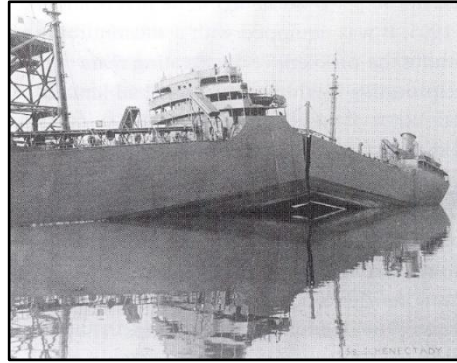
Figure 1.4: The SS Schenectady broke in two [19].

The Havilland Comet disasters were also an important driving force for the development of Fracture Mechanics techniques. During the years 1953 and 1954 three fatal Comet crashes occurred, leading to the permanent grounding of the entire fleet. In order to discover what was happening, the UK Ministry of Civil Aviation decided to execute a pioneer test using the only available technology at that time. They made a flight simulation, with a real plane inside of a tank flooded with water. Along with hydraulic jacks, the wings were moved up and down, to simulate a real flight. The plane tested had already 1230 pressurized flights before the test and suffered more than 1830 simulated flights before failing at the corner of a square window, where a fatigue crack initiated due to the local stress concentration and then propagated until the final failure, as shown in Fig. 1.5.
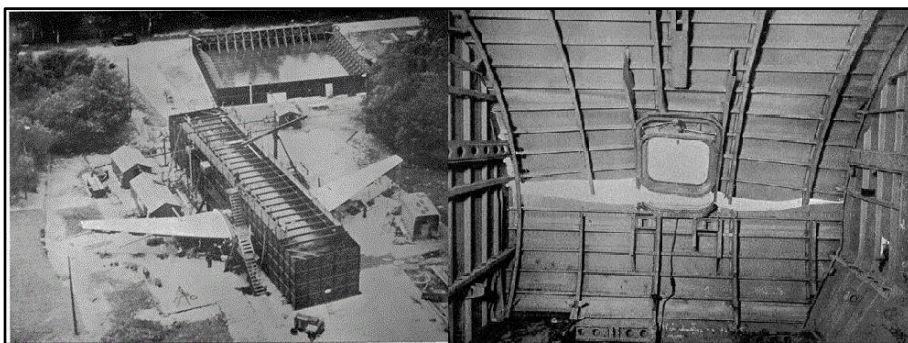
Figure 1.5: Comet airplane test [20].

Besides that, Anderson [3] made a list of other incidents reported over the years, which emphasizes the importance of Fracture Mechanics.

1.2
Aim of this study

This thesis first aims to measure the *J*-integral fracture toughness of the steel API 5L X80, using standard SE(B) specimens and elastic compliance technique procedures normalized by ASTM E1820-17. The toughness is also measured using non-standard clamped SE(T) specimens, following the methodology developed by Cravero and Ruggieri [21]. In this way, this aim is to evaluate the effects of the specimens' geometry and of the type of loading on the fracture toughness measurements, due to their distinct constraint conditions.

Moreover, this thesis aims to use the measured properties to predict the critical loads following the procedures of levels 2 and 3 of the API 579 fitness-for-service recommended practice. Finally, the thesis validates the predictions comparing them with experimental tests on a flat plate with a through-wall crack flaw, to quantify how conservative are these predictions for this situation.

1.3
Motivation

Structural integrity evaluations play a significant role in the petrochemical industry, which uses many piping systems and pressure vessels that are not as constrained as the standard specimens used to measure fracture toughness. Lacking specific procedures for such components, FFS guides must assume some excessively conservative assumptions, to prevent unacceptable accidents. Since there is also conservatism on the measurement of fracture toughness, too conservative procedures can generate uneconomic designs. Hence, it is essential to understand EP fracture mechanics concepts to support decisions such as if it is necessary to replace a whole piping system, or just to make some repairs, or maybe even to do nothing about it.

The steel used on this work was the API 5L X80, since it is a relatively new material that is being considered and used for some severe applications in petrochemical industries. Due to the increased production of petroleum and natural gas, pipeline networks are expanding in the world, and they require steels that can resist aggressive environments on deep ocean waters. The API

5L X80 is a dual-phase High Strength and Low Alloy (HSLA) steel, a class of materials that have been developed to support such requirements. They allow the reduction of pipeline thicknesses, resulting in weight reduction and lower consumption of raw material. Moreover, the API 5L X80 has good weldability and low hardenability. The microstructure is composed of acicular ferrite with a small amount of martensite/austenite, that results in high tensile strength and low ductile to brittle transition temperature. The steel is manufactured with a controlled lamination process, which refines the grains and precipitates carbides and nitrides of the micro-alloyed elements. Because of that, it prevents recrystallization, causing their strength resistance increase without adding carbon or manganese in the alloy. As a result, it hinders the toughness and weldability of the material [22] [23]. These types of steels manufactured for pipeline systems are classified according to the American Petroleum Institute (API). The grade X80 means that the steel has a yield strength of at least 80 ksi or 550MPa.

1.4
Thesis structure

Chapter 1, resumes the importance of this subject, presents the aims of this study, and review the motivations for this work.

Chapter 2 reviews some basic Fracture Mechanics concepts and properties definitions.

Chapter 3 reviews procedures to measure fracture toughness using SE(B) and SE(T) specimens.

Chapter 4 lists the results of the material's properties measurements.

Chapter 5 studies structural integrity procedures proposed in API 579, and presents predictions and experimental tests for the case in question here.

Chapter 6 summarizes all the experimental results obtained in this work.

Chapter 7 presents the conclusions and address future work suggestions.

2.
Theoretical background

This chapter introduces the terminology used in this work and briefly reviews. As well some mechanical property definitions and basic concepts of Fracture Mechanics pertinent to its purposes.

2.1
Tensile strength and ductility

Steels, like most structural metallic alloys, obey a linear relationship between stresses and strains while they remain elastic following Hooke's law until they reach their proportional limit, after which plastic strains are induced in them. Young's modulus (E) defines the ratio between LE stresses and strains, which quantifies the material stiffness. After the proportional limit, the material yields and start to accumulate plastic strains.

Ductility is the capacity to tolerate plastic strains, and it can be measured by the residual elongation of a base of measurement marked on the specimen surface before the tensile test. Or else, by the reduction in the area of the necked section after the test.

Since the proportional limit is difficult to measure, engineers use the Yield Strength (σ_{ys}), which defines the stress required to cause an arbitrary small amount of plastic deformation on standard tensile specimens of the material. ASTM E8/E8M [24] defines σ_{ys} by the intersection of the stress-strain curve with a 0.2% offset line parallel to its linear zone. Hence, the yield strength should not be confused with the proportional limit of the material. Indeed, a stress $\sigma = \sigma_{ys}$ leaves a residual plastic strain $\varepsilon_{pl} = 0.2\%$ after unloading the tensile specimen.

Looking at the engineering stress-strain curve (Fig. 2.1), the Ultimate Strength (σ_{us}) is the highest stress the material can support before breaking, or the stress required to start the necking in a tension test. After that point, the engineering stress decreases until the fracture occurs.
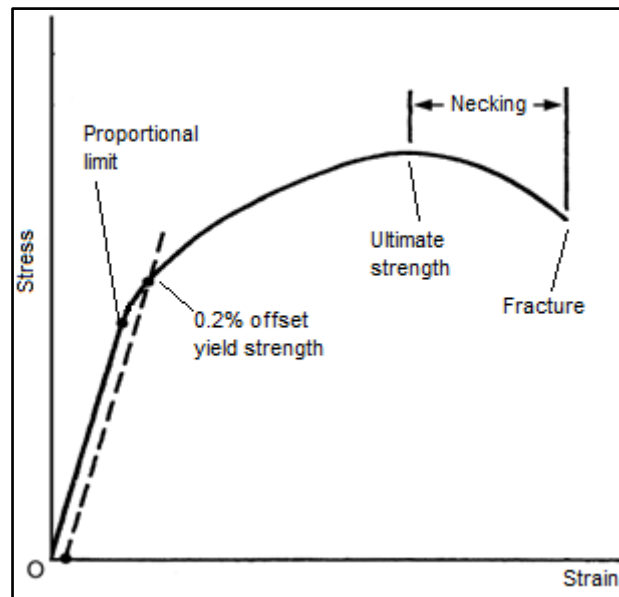
Figure 2.1: Typical engineering stress-strain curve [25].

2.2
Some basic Fracture Mechanics concepts

Fracture Mechanics is the science that studies and models crack effects in solid components, considering how stress concentration at crack tip affects the mechanical behavior of cracked components. It uses theories of elasticity and plasticity to analyze the behavior of flawed structures. Such concepts allow run-repair-replace decisions based on solid mechanical principles to avoid failures of damaged components. Its inputs are the flaw size, the applied stress, the cracked component geometry and the relevant material properties (in particular its fracture toughness). On the other hand, the traditional strength of materials approach requires only the applied stress and basic mechanical properties for design purposes, ignoring localized crack effects. Figure 2.2 illustrates the basic features of the strength of materials and fracture mechanics approaches.
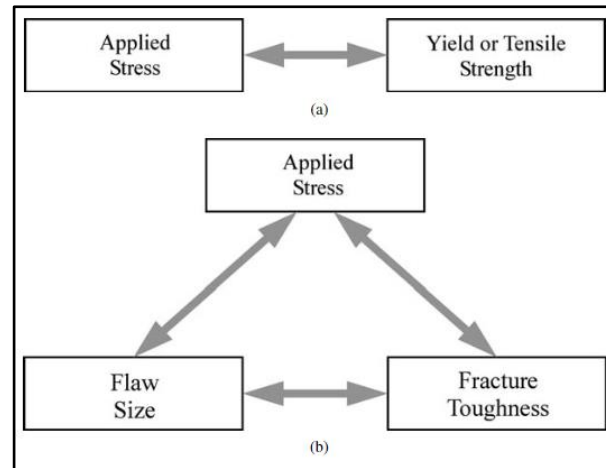
Figure 2.2: Comparison of (a) strength of materials and (b) fracture mechanics approach [3].

Fracture Mechanics concepts can be used as well to model residual lives of cracked structural components [26]. LEFM concepts can deal with cracked brittle components, while EPFM can deal as well with ductile components, in which the plastic zone *pz* is relatively large and invalidates LE stress solutions, as illustrated in Fig. 2.3. LEFM uses linear whereas EPFM uses nonlinear models. There are also Fracture Mechanics concepts that depend on time, useful to model e.g. dynamic, viscoelastic, and viscoplastic crack structural problems, as schematized in Fig. 2.4. However, such time-dependent problems are outside the scope of this thesis.
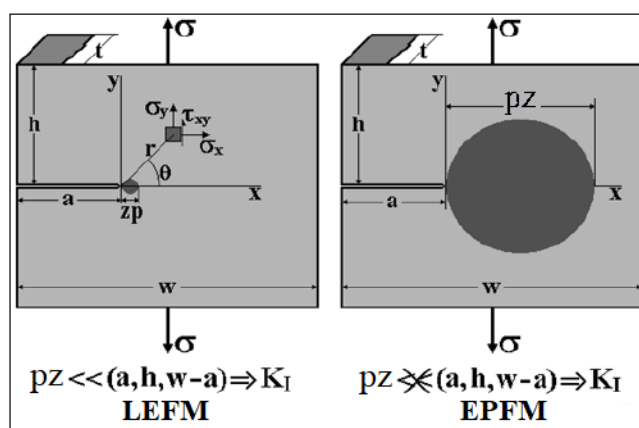
Figure 2.3: Basic difference between the validity of LEFM and EPFM [4].
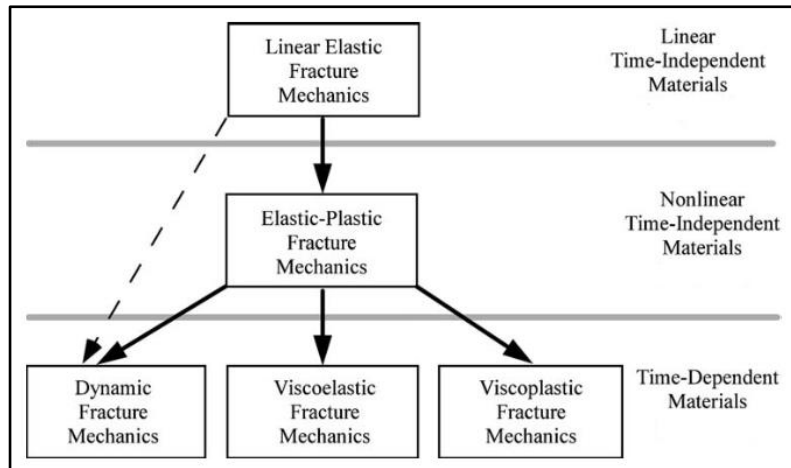
Figure 2.4: Fracture mechanics [3].

2.2.1
Fracture surfaces

Macroscopic and microscopic features of fracture surfaces can give many types of information about the fracture process. They can indicate e.g. crack initiation sites, crack propagation directions, load conditions, geometric constraints, or fabrication imperfections related to the fracture. Ductile and brittle cracking are two extreme types of fracture. Brittle fractures break the components almost instantaneously, while ductile fractures involve some crack tearing before rupture. Figure 2.5 illustrates basic fracture types of tensile test specimens.
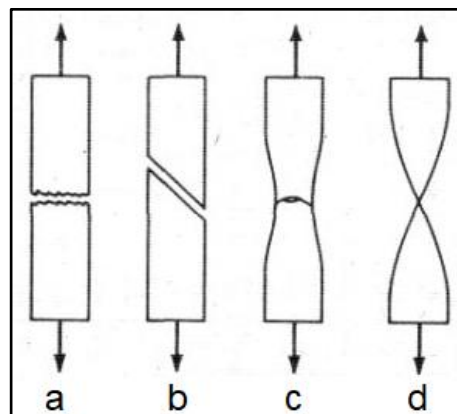
Figure 2.5: Fracture types on tensile tests: a) brittle fracture; b) shear fracture;
c) ductile fracture ; d) perfect ductile fracture [3].

2.2.1.1
Ductile fractures

Ductile metallic alloys tend to neck on tension tests. After reaching the peak stress σ_{us}, a cross-section of tension test specimens becomes unstable and concentrates further plastic strains until final rupture. Instability occurs when the material capacity to strain-hardening, or to increase its resistance due to plastic straining, cannot compensate anymore the cross-section reduction of the test specimen under tensile stresses. Hence, strain-hardening promotes stability in tension tests. However, strain-hardening is not a ductility measure.

There is no necking in compression tests. Necking induces triaxial stresses with tensile hydrostatic components around the necked section, while shear stresses induce slip around inclusions and grain-boundaries, tending to form microvoids in its interior. Hence, the main micromechanism involved in ductile fractures is growth and coalescence of such microvoids, a process helped by compressive but inhibited by tensile hydrostatic components. The material along the specimen surface deforms along shear planes in final fracture stages, creating the cup-cone feature characteristic of ductile fractures, see Fig. 2.6.
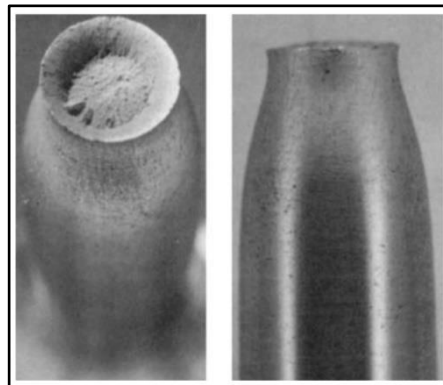
Figure 2.6: Ductile fracture [25].

Ductile fractures tend to absorb a large amount of energy. Therefore, ductile materials tend to be tough. High temperatures and low hydrostatic components enhance ductility, in particular in metallic alloys. However, ductility cannot be confused with toughness, the ability to tolerate cracks under tensile loads. Toughness can be enhanced by any micromechanism capable of absorbing

energy during the fracturing process. In this way, there are non-ductile materials (like wood or fiber-reinforced polymers, e.g.) that are tough.

2.2.1.2
Brittle fractures

Brittle metallic alloys do not neck on tensile tests. Their fracture surfaces are flat, perpendicular to the load direction, and reflect light in a dispersive way, see Fig. 2.7. Brittle fractures are essentially elastic, i.e. they are associated with a small amount of plastic strains ($\varepsilon_{plmax} < 5\%$ is a usual criterion to define a brittle material). Hence, they tend to absorb only a low amount of energy before breaking. The main micromechanism involved in brittle fractures is cleavage, or transgranular fracture by separation across well-defined crystallographic planes [27]. High tensile hydrostatic components and low temperatures, which tend to curb plastic strains, can significantly affect this type of fracture.
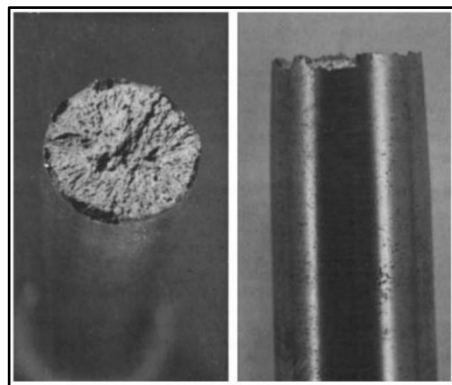
Figure 2.7: Brittle fracture [25].

2.2.2
Fracture toughness

Fracture toughness quantifies the material ability to tolerate cracks [4]. In LEFM, toughness is a mechanical property that can be quantified by a critical value of an energy parameter ($\mathcal{G}_{Ic}$), or by the equivalent critical stress intensity factor (K_{Ic}), both measured at the moment the unstable crack growth that causes the component´s fracture starts. Procedures to measure $\mathcal{G}_{Ic}$ and K_{Ic} are studied in Sections 2.3.2 and 2.3.4, respectively.

In EPFM, fracture toughness usually depends on the cracked component geometry, so it is not a mechanical property. However, the specific energy J_{Ic} in J/m^2 required to start crack tearing, or the Crack-Tip Opening Displacement (CTOD) at that instant, can be under certain conditions, see Section 2.4.2. J_{Ic} is not associated with final fractures, but with the initiation of the crack tearing stage, a stable part of the fracture process that requires an increase in loading to proceed. As mentioned above, ductile materials usually have high fracture toughness, but a high fracture toughness does not mean the material is ductile. Any mechanism that dissipates energy during the fracture process contributes to the material toughness. Hence, care is needed when using the word brittle, which is the antonym of both ductile and tough. In this way, there are brittle (non-ductile) materials that are tough.

2.3
Linear Elastic Fracture Mechanics (LEFM) fundamentals

Failures on ductile materials can be caused by plastic collapse or ductility exhaustion, but brittle materials usually fail by unstable crack propagation. Assuming cracks are notches with a null tip radius, they cannot be modeled by traditional stress analysis techniques. Crack models need Fracture Mechanics tools instead. Cracks can be loaded in three modes. Mode I is the opening mode induced by normal stress; Mode II is the sliding mode, generated by shear loads perpendicular to the crack front; and Mode III is the tearing mode, caused by shear loads parallel to the crack front, see Fig. 2.8. Mode I is the most important one since it does not spend energy on crack surface friction.
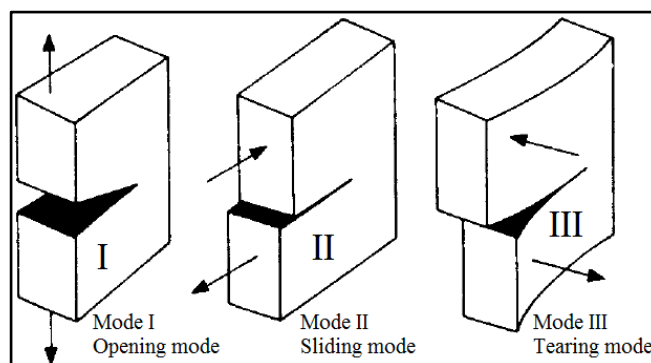
Figure 2.8: Modes of cracking [1].

2.3.1
Stress concentration factor K_t

In 1913, Charles Edward Inglis analyzed a large plate with a small elliptical hole, as shown in Fig. 2.9, where $2a$ and $2b$ are the ellipse axes. He proved that the stress concentration factor K_t of the ellipsis increases as its notch tip radius ρ decreases, according to the following the equation.

$$K_t \;=\; \frac{\sigma_{max}}{\sigma_n} \;=\; 1 + \frac{2a}{b} \;=\; 1 + 2\sqrt{\frac{a}{\rho}} \tag{2-1}$$
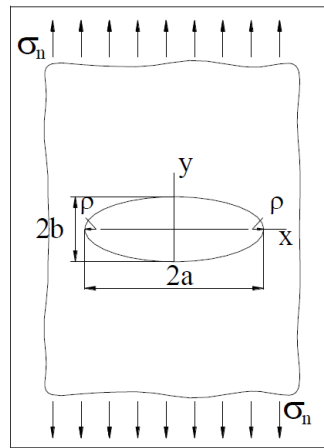
Figure 2.9: Inglis plate [28].

This equation shows that sharp notches should be avoided because they have high K_ts. Since Inglis' equation is LE, it also predicts infinity stresses on crack tips, which are sharp notches with $\rho = 0$, a clear physical impossibility. Griffith was the first to explain how cracks could be tolerated in brittle materials despite their very high stress concentration factor.

2.3.2
Griffith's energy approach

Based on the first law of thermodynamics, Griffith provided the first analysis of crack stability in 1920. He balanced the decrease in potential energy (E_T) of a body, related to the release of stored elastic energy and work done by movement of the external loads (E_P), and the energy needed to create new

surfaces (W_s), due to the crack propagation in ideally brittle materials. Griffith energy balance under static conditions, for an incremental increase in crack area *dA*, can be expressed in the following way:

$$\frac{dE_T}{dA} = \frac{dE_p}{dA} + \frac{dW_s}{dA} = 0 \qquad (2\text{-}2)$$

Brittle fracture occurs when the strain energy released rate associated with crack extension is larger than the energy spent to create new crack surfaces. Based on the analysis developed by Inglis, the potential energy of the plate with an elliptic hole is given by:

$$E_p = \frac{\pi \sigma^2 a^2 B}{E} \qquad (2\text{-}3)$$

where *E* is Young's modulus, and *B* is the plate thickness. The energy required to create new surfaces W_s is defined as:

$$W_s = 4aB\gamma_s \qquad (2\text{-}4)$$

where γ_s is the specific surface energy. Rewriting Eq. 2-2, taking into account Eq. 2-3 and 2-4, it is possible to define the critical stress (σ_f) for plane strain:

$$\sigma_f = \sqrt{\frac{2E\gamma_s}{\pi a}} \qquad (2\text{-}5)$$

Irwin and Orowan [4] independently modified the Griffith expression to account for materials that are not ideally LE, taking into account the plastic work per unit area of surface created γ_p. They re-defined the fracture energy by $w_f = \gamma_s + \gamma_p$, considering elastic and plastic, viscoelastic, or viscoplastic effects, depending on the material.

2.3.3
Energy release rate

Irwin [13] developed the modern version of Griffith's energy approach, defining the potential energy release rate per unit area $\mathcal{G}$ by:

$$\mathcal{G} = -\frac{\partial E_p}{\partial A} \qquad (2\text{-}6)$$

For a wide plate with a central crack, $\mathcal{G}$ is given by:

$$\mathcal{G} = \frac{\pi\sigma^2 a}{E} \tag{2-7}$$

He assumed that fracture occurs when $\mathcal{G}$ reaches $\mathcal{G}_{Ic}$, the critical value of the potential energy release rate, or the toughness of the material in mode I.

$$\mathcal{G}_{Ic} = \frac{dW_s}{dA} \tag{2-8}$$

2.3.4
Stress intensity factors

In 1957, Irwin and Williams independently analyzed 2D LE stress-strain fields around crack tips. Considering polar coordinates with origin at the crack tip (Fig. 2.10), the stress field in Mode I is given by

$$\sigma_{ij} = \frac{K_I}{\sqrt{2\pi r}} f_{ij}(\theta) \tag{2-9}$$

where σ_{ij} are the stresses, r and θ are polar coordinates, $f_{ij}(\theta)$ are dimensionless functions, and K_I is the Mode I Stress Intensity Factor (SIF), which depends on the cracked body geometry and its loading conditions.

Since the stresses vary with $1/\sqrt{r}$, this equation is singular ($\sigma \to \infty$ when $r \to 0$). On the other hand, it predicts $\sigma \to 0$ for large r, instead of the nominal stress. Hence, this equation is valid only for a limited area around the crack tip, and it results in:

$$\sigma_{xx} = \frac{K_I}{\sqrt{2\pi r}}\cos\left(\frac{\theta}{2}\right)\left[1 - \sin\left(\frac{\theta}{2}\right)\sin\left(\frac{3\theta}{2}\right)\right] \tag{2-10}$$

$$\sigma_{yy} = \frac{K_I}{\sqrt{2\pi r}}\cos\left(\frac{\theta}{2}\right)\left[1 + \sin\left(\frac{\theta}{2}\right)\sin\left(\frac{3\theta}{2}\right)\right] \tag{2-11}$$

$$\tau_{xy} = \frac{K_I}{\sqrt{2\pi r}}\cos\left(\frac{\theta}{2}\right)\sin\left(\frac{\theta}{2}\right)\cos\left(\frac{3\theta}{2}\right) \tag{2-12}$$
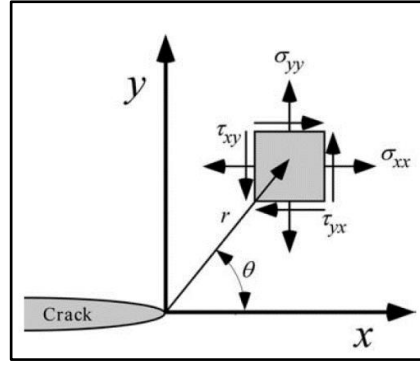
Figure 2.10: Stress field near the tip of a crack [3].

Real materials are not LE under higher stresses, so they yield at crack tips, inducing a plastic zone around them. However, if the plastic zone is relatively small, the stress field around the crack tip remains predominantly LE, then Eqs. (2.9)-(2.11) and the SIF *K* can be used to make reasonable predictions about the crack behavior. If it is not, *K* no longer controls the stress field, thus cannot make such predictions. SIFs control LE stress/strain field amplitudes around crack tips, and in general can be written as:

$$K_I = \sigma\sqrt{\pi a}\cdot f(a/W) \tag{2-13}$$

where σ is the nominal stress applied on the cracked component, *a* is the crack length, and *f(a/W)* is a dimensionless function that depends on the cracked body geometry and its loading conditions.

Since Eq. (2.9) is LE, once *f(a/W)* is found for a given load/cracked body configuration, it can be listed (because LE solutions are unique). Assuming that material fails at a critical combination of stresses and strains, then LE cracks become unstable at a critical value of *K*. The cracked body thickness affects this K_{crit}, where thick specimens are subject to plane strain condition. Contrarily, thin specimens are under predominant plane stress condition. K_{crit} decreases with specimen thickness until it reaches a plateau (Fig. 2.11). In mode I, this plateau is defined as K_{Ic}, which is a measure of fracture toughness in MPa$\sqrt{m}$. Therefore, the size and geometry of the cracked body do not influence K_{Ic}.
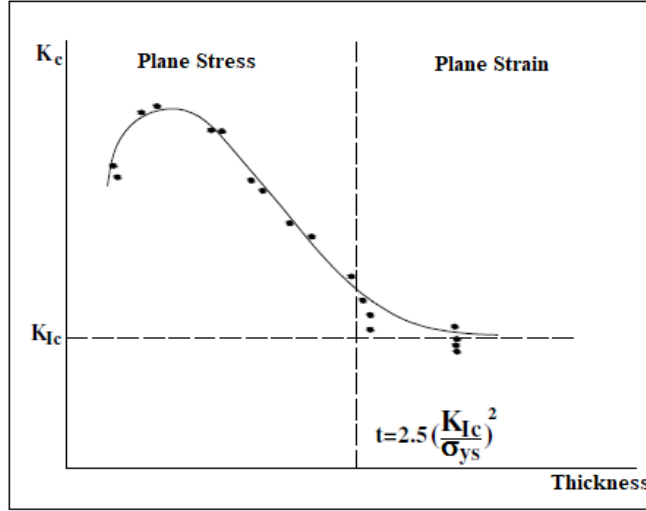
Figure 2.11: Critical SIF in function of thickness [4].

To summarize, K and G are parameters that describe the crack's behavior under LE conditions. The first one characterizes the stresses, strains, and displacements near the crack tip, while the second quantifies the potential energy release rate per crack extension area. Therefore, K is a local parameter whereas G is global, and it is possible to correlate one with the other. For example, assuming a crack in an infinite plate subject to uniform tensile stress, K is given by Eq. 2-13 with *f(a/W)* equals to 1 and G is given by Eq. 2-7. Combining these two equations, the relationship can be written as:

$$G = \frac{K_I^2}{E} \tag{2-14}$$

where E for plane strain conditions is replaced by $E/(1 - \upsilon^2)$.

2.3.5
Crack-tip plasticity

The plastic zone (*pz*) size at the crack tip defines when the LE stress solution is valid or not. Therefore, different methodologies were developed to estimate its size e.g. Irwin and Dugdale. Assuming that the *pz* boundary occurs when the stress given by Eq. 2-9 reaches σ_{ys}, Irwin considered the *pz* as circular with a diameter $r_p = r_y$ under a plane stress state, where r_y is defined as:

$$r_y = \frac{1}{2\pi}\left(\frac{K_I}{\sigma_{ys}}\right)^2 \qquad (2\text{-}15)$$

Irwin neglected strain hardening, resulting in a stress distribution represented by a horizontal red line at σ_{ys} as illustrated in Fig. 2.12, which shows a plot of LE stress solution versus distance from the crack tip (r). However, this is not valid for EP material considering that the stress cannot be higher than σ_{ys} represented by the cross-hatched region of the plot. It violates the equilibrium equation because it does not redistribute the stress in this area when the material yields at the crack tip.
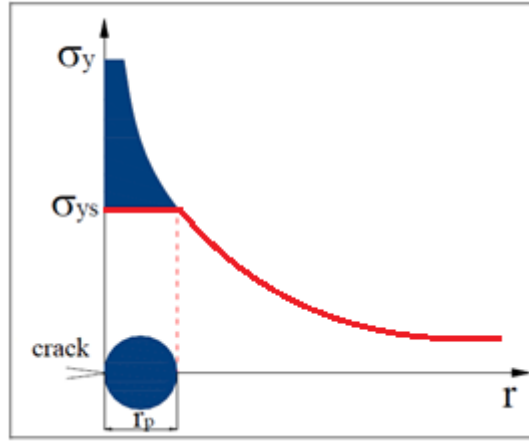
Figure 2.12: Plastic zone size [28].

Therefore, the plastic zone needs to increase in size to balance the forces. Thus, Irwin proposed a deeper virtual crack, with effective size $a_{eff} = a + \delta$, where δ is the correction for the plastic zone size given by:

$$r_p = r_y + \delta \qquad (2\text{-}16)$$

Fig. 2.13 shows this adjusted method, where it indicates the cross-hatched region A and B. Assuming that these two areas are equals to balance the stress, then $\delta = r_y$ resulting in $r_p = 2r_y$. By adjusting the crack size on the stress fields equations for LE solution under plane stress condition, the *pz* size that considers plasticity at the crack tip is given by:

$$r_y = \frac{1}{\pi}\left(\frac{K_I}{\sigma_{ys}}\right)^2 \qquad (2\text{-}17)$$
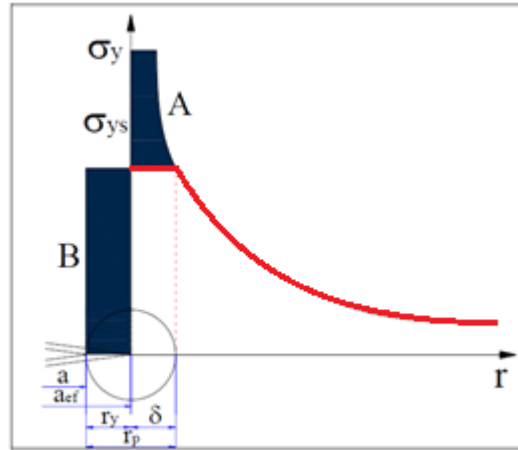
Figure 2.13: Adjusted plastic zone size [28].

On plane strain condition, the yielding occurs when the stress reaches $\sigma_{ys}/(1-2\nu)$. Thus, the yield strength is 2 to 3 times on plane strain than plane stress for steel. Therefore, Irwin divided the *pz* diameter by a factor of 3.

2.3.6
Crack-tip triaxiality

The triaxial stress state inhibits plastic deformation at the crack or notch front. To point out, consider two bar specimens under tensile load in the *y*-direction, where one is flat, and the other has a notch. The flat bar is under plane stress condition, as well the material sufficiently far from the notch on the other bar. The material near the notch has a significant stress concentration, which makes it try to contract in the *x* and *z*-direction. However, the surrounding material prevents this deformation, that generates a triaxial state and ensuring plane strain condition.

Fig. 2.14 illustrates these bar specimens, showing the constraint effect on the material yield strength and ductility. Under high stress triaxiality, the material behaves as it was brittle. Eventually, it reaches the plateau when the stress becomes hydrostatic that prevents any material yielding.
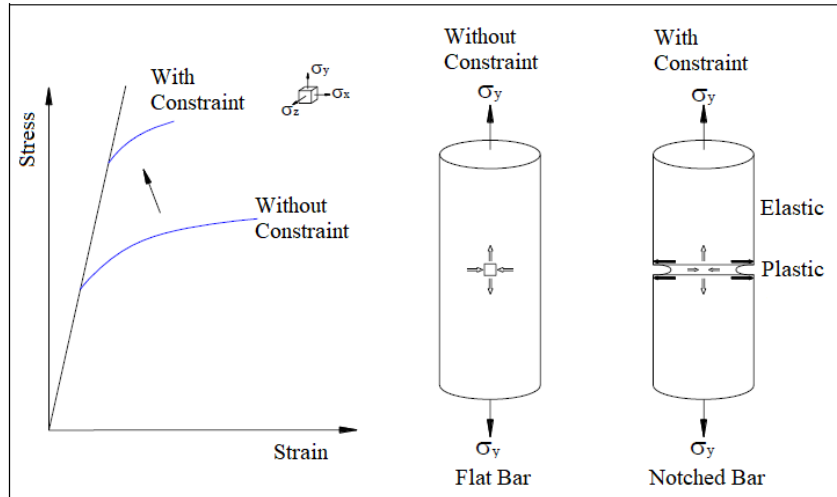
Figure 2.14: Plastic constraint effect on yield strength [28].

Fig. 2.15 shows the thickness effect on the stress state at the crack front. The central region of the crack front is predominantly under plane strain, whereas the region near the surface is under plane stress. An increase of thickness means an increase of the region under plane strain that increases the constraints at the crack tip. Because of these constraints, ductile materials with significant thickness and crack depth can fail due to brittle fracture.
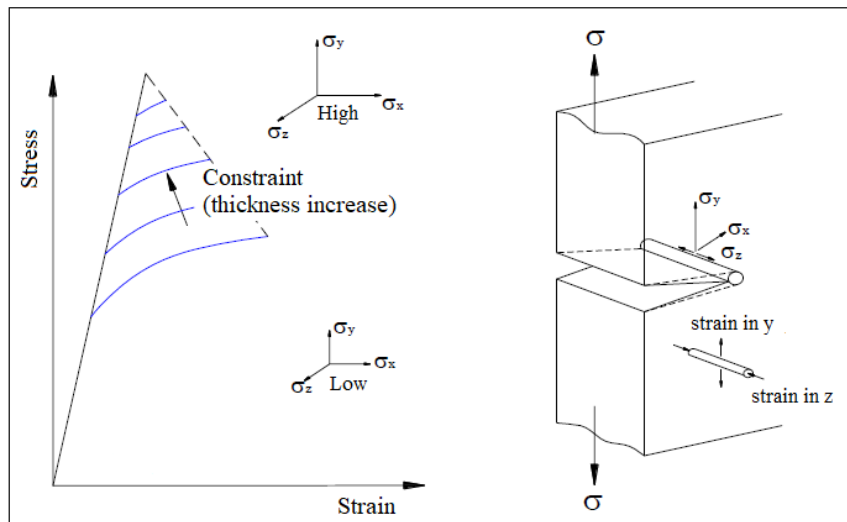
Figure 2.15: Specimen thickness effect on plastic constraint [28].

2.4
Elastic-Plastic Fracture Mechanics (EPFM) fundamentals

Elastic-plastic fracture mechanics extends the studies of fracture behavior beyond the LE regime. The EPFM applies to materials that have a significant plastic deformation, resulting in a nonlinear elastic region at the crack-tip. The two main parameters are the Crack Tip Opening Displacement (CTOD) and the J contour integral. Both describe crack-tip conditions in EP materials and have critical values that can be used to quantify fracture toughness under moderate-to-high crack tip plasticity. The EPFM also has a limitation, since it does not treat the occurrence of plastic collapse.

2.4.1
Crack-Tip Opening Displacement (CTOD)

Wells analyzed that the crack faces move apart and the crack tip blunts before the onset of extension, as illustrated in Fig. 2.16. This extent of the opening depends on the material's toughness and can be associated with CTOD. Wells related the CTOD (δ) to the SIF in the small-scale yielding limit using Irwin plastic zone, with the assumption of an effective crack length $a + r_y$ resulting in the following equation:

$$\delta = \frac{4K_I^2}{\pi E \sigma_{ys}}$$

(2-18)
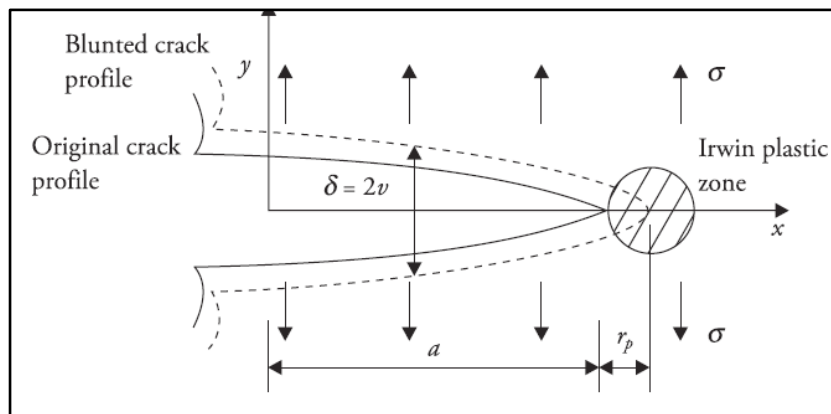
Figure 2.16: Crack tip opening displacement [29].

The CTOD parameter is not valid for LEFM, since it requires a plastic zone at the crack tip, that allows the displacement of the two crack faces. Dugdale and Dawes also did studies to measure CTOD. Dugdale used the strip-yield theory by assuming a slender *pz* at the crack tip in nonhardening materials and plane stress that have finite stress. Dawes estimated CTOD by measuring the Crack Mouth Opening Displacement (CMOD) and using similar triangles construction to relate the CMOD with CTOD. He developed a CTOD design curve, which is a semiempirical fracture mechanics methodology for welded steel structures [30].

2.4.2
J-Integral

Rice proposed to use the *J*-integral, developed by Eshelby, as a parameter to define fracture in elasticity and plasticity conditions. This parameter is a path-independent line integral to analyze the crack on nonlinear materials. It can be used on EP materials by assuming they have the same behavior as nonlinear materials when unloading does not occur. Nonlinear materials follow the same loading path during unloading, whereas EP materials have a linear unloading path with a slope equals to Young's modulus as demonstrated in Fig. 2.17.
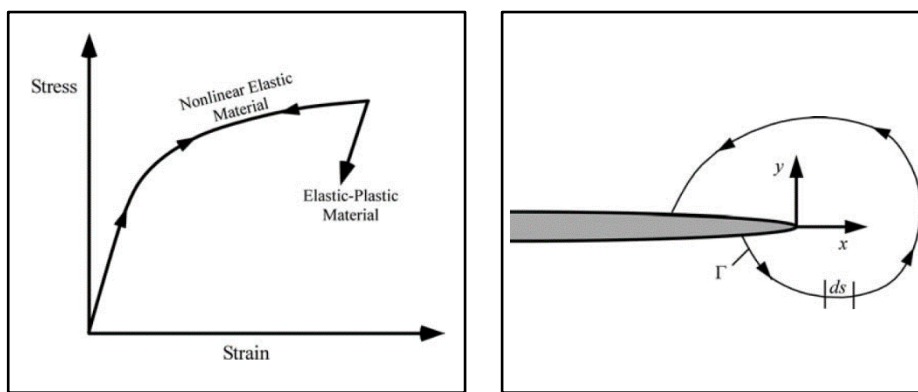
2.17(a): Stress strain behavior.   2.17(b): Path independent contour.

Figure 2.17: *J*-Integral [3].

Hutchinson, Rice and Rosengren (HRR) [31] [32] analyzed that *J*-integral gives energy release rate in a nonlinear elastic materials and it can be expressed in the following way:

$$J = \int_{\Gamma} \left(U dy + \frac{T_i \partial u_i}{\partial x} ds \right) \tag{2-19}$$

where U is the strain energy density given by Eq. 2-20, T_i are the traction vector components at a point on the contour defined by Eq. 2-21, u_i are displacement vector components, *ds* is the length increment along the contour of the counterclockwise path Γ. The stress and strain tensors are denoted as σ_{ij} and ϵ_{ij} respectively, and n_j are the components of the unit vector normal to Γ.

$$U = \int_0^{\epsilon_{ij}} \sigma_{ij} d\epsilon_{ij} \tag{2-20}$$

$$T_i = \sigma_{ij} n_j \tag{2-21}$$

Both J and $\mathcal{G}$ represents the potential energy that is released from the structure when the crack grows, although $\mathcal{G}$ is only for LE conditions while J can be used on LE and EP materials. Also, it is possible to correlate J with CTOD using the following equation:

$$J = m\sigma_{ys}\delta \tag{2-22}$$

where *m* is a dimensionless constant that depends on the material properties and stress state.

2.4.3
J-R Curve

For EPFM, the fracture toughness J_{Ic} does not characterize a catastrophic failure as K_{Ic} for LEFM. Instead, it indicates the initiation of stable crack growth in EP materials and have a significant variation with the cracked body geometry and loading condition. As the crack size increases, the material resistance also increases, resulting in the *J*-resistance or *J-R* Curve that relates *J* with crack extension (Fig. 2.18). The initial part of the curve has a linear relationship due to crack blunting until the crack initiate. After that, the relation becomes nonlinear up to material failure by tearing instability or plastic collapse.

The actual point of crack initiation is usually ill-defined [3]. Therefore, the arbitrary definition is the intersection of the *J-R* curve with the 0.2% offset yield

strength. Using J_{Ic} as a parameter of project is usually conservative since it does not consider the material resistance growth during the tearing.
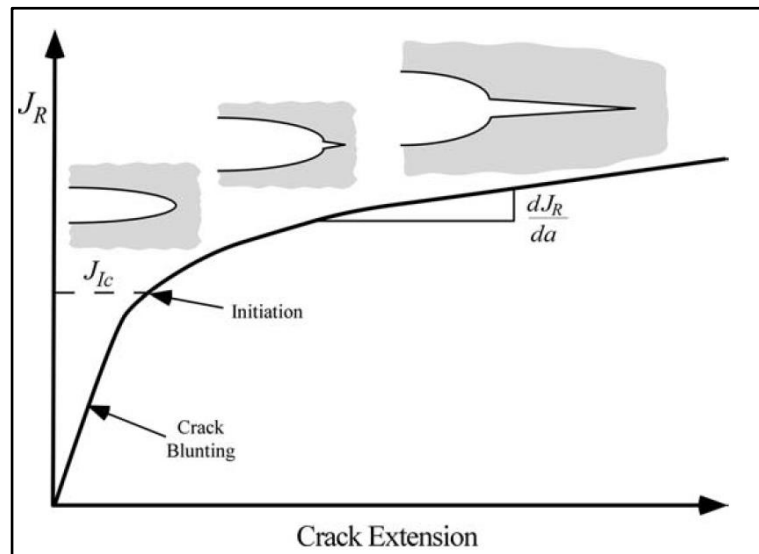
Figure 2.18: *J-R* Curve for ductile material [3].

2.5
Biparametric fracture mechanics fundamentals

The single fracture mechanics parameters (*K*, *J*, or CTOD) is valid only under Small Scale Yielding (SSY) condition, where the fracture criterion can be independent of geometry and loading type. Under Large Scale Yielding (LSY), the fracture toughness changes with the cracked body geometry and loading condition. Therefore, it is necessary for another parameter to characterize the crack tip stresses and strains. Ductile materials can have LE behavior with SSY when they have a large thickness and deep cracks. Because of the high triaxial stress state at the crack front causing plasticity constraint. Fig. 2.19 illustrates the effect of crack size has on fracture resistance.

Fracture toughness measured on highly constrained specimens tend to be conservative in relation to the engineering structures. Standardized specimens have a significant thickness and crack depth to ensure plane strain condition at the crack tip [33]. Besides that, it requires a minimum parameter M [34], which depends on specimen type and hardening properties. This parameter ensures *J* dominance at the crack tip, in order to prevail dominance of the HRR

singularity. Therefore, standardized specimens are under SSY condition, and the fracture toughness can be characterized as a single parameter.
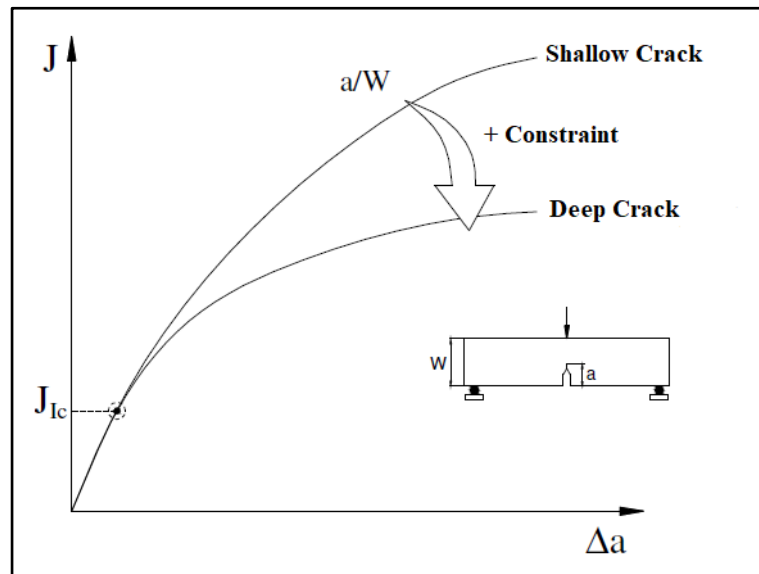
Figure 2.19: Crack size effect on *J-R* curve [28].

Specimens under low constraint and LSY conditions require two parameters to characterize the crack driving force, such as the *T*-stress [35] and *Q*-parameter [36] [37]. Where the first describes the geometrical constraint effect, and the second defines the stress fields on the crack tip. Both parameters measure the triaxiality at the crack tip front and depend on the cracked body geometry and loading condition.

In general, cracks that initiate in pipelines structures are often shallow and under tensile stress [39]. Also, crack tip constraints are lower in tension than in bending [38]. Therefore, cracks in pipes are on different conditions than in the standardized SE(B) specimens with deep crack and bending, making the standard conservative. For a better design, it is necessary to use specimens with similar conditions to the engineering structure. Given that, there is a considerable amount of study on the SE(T) specimen, which provides a more similar constraint condition when compared to pipes, as illustrated in Fig. 2.20 [11]. This specimen generally develops a lower stress triaxiality in front of the crack tip. Chapter 3.2 describes the procedure to calculate fracture toughness on non-standards SE(T) specimens.
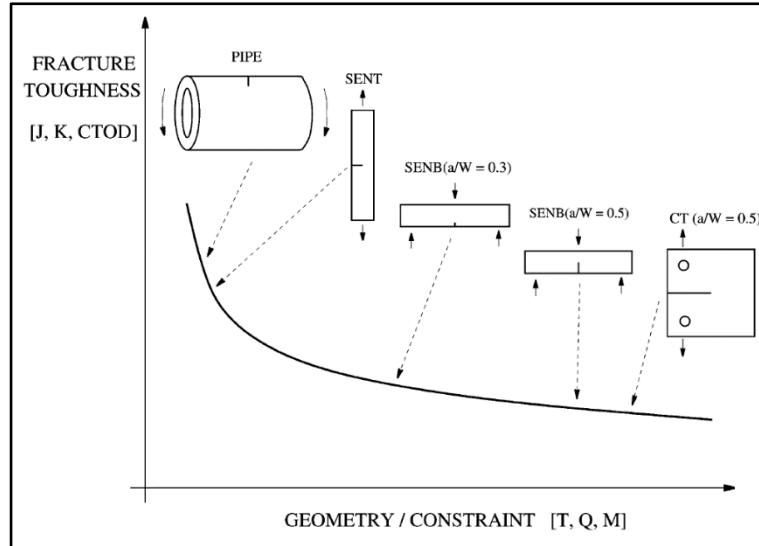
Figure 2.20: Constraint and geometry influence on fracture toughness [40].

2.5.1
T Stress

Williams analyzed the crack tip stress field by using an infinite power series, where the leading term exhibits $1/\sqrt{r}$ singularity and the second term is constant with r [41]. The third and higher terms have positive exponents on r, so they fade at the crack tip. LEFM uses only the first term of this power series that gives the single parameter for fracture mechanic. However, the second term, which has a significant influence on the plastic zone shape and the stress field, remains finite. The stress field considering an isotropic elastic material under plane strain, the first two terms of the series, and Mode I loading is given by:

$$\sigma_{ij} = \frac{K_I}{\sqrt{2\pi r}} f_{ij}(\theta) + \begin{bmatrix} T & 0 & 0 \\ 0 & 0 & 0 \\ 0 & 0 & \nu T \end{bmatrix} \tag{2-23}$$

where T is a uniform stress in the parallel direction to the crack that causes νT on the crack front direction under plane strain condition that influences stresses inside the plastic zone. When $T = 0$, the crack front has SSY behavior, where the plastic zone is negligible when compared with the component's size. Therefore, it is possible to use LE stress solution defined by the first term of the power series. If T is positive, there is an increase of constraints, resulting in an even higher triaxiality at the crack tip. On the other hand, when T is negative,

these constraints significantly decrease, thus it is necessary to use the bi-parameter methodology.

The *T*-stress is an elastic parameter, so this methodology fails under EP conditions. The relationship between T-Stress and SIF is given by the biaxiality ratio of β, given by the following equation:

$$\beta = \frac{T\sqrt{\pi a}}{K_I}$$
(2-24)

Fig. 2-21 shows how β varies for each specimen geometry for a given *a/W*, showing the level of constraint. SE(B) specimens have β as positive for *a/W* higher than 0.4. Therefore, standardized specimens, that require *a/W* > 0.45 have a high level of constraint. Negative β indicates a low level of constraint e.g. SE(T) specimens with *a/W* lower than 0.6.
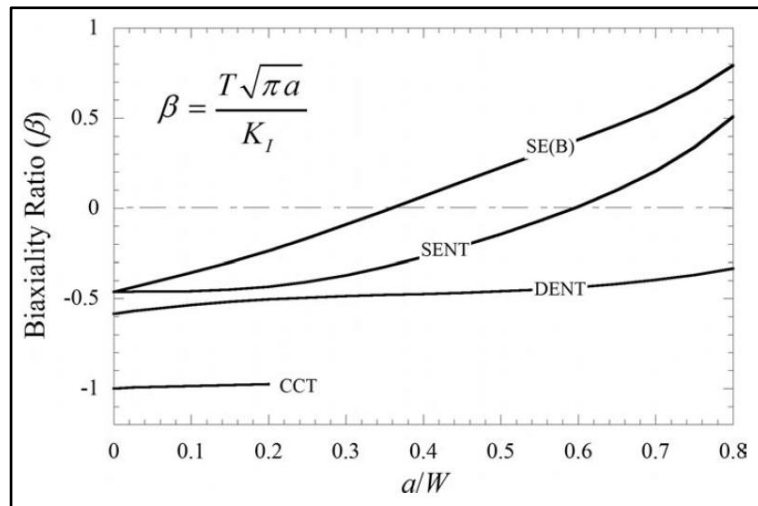
Figure 2.21: Biaxiality ratio [3].

2.5.2
Q Parameter

Another biparametric method is the *J-Q* theory, which says that the critical value of *J* depends on the *Q* parameter. For SSY at the crack-tip when $T = 0$, the *pz* stress field can be described by a power series, where the first term is the HRR solution. The high order terms can be grouped into a difference field,

where it corresponds approximately to an alteration of the stress field in front of the crack tip. The Q parameter represents the amplitude of this approximate difference [3]. The stress field solution is given by:

$$\sigma_{ij} = \left(\sigma_{ij}\right)_{T=0} + Q\sigma_o\delta_{ij} \tag{2-25}$$

$$Q = \frac{\sigma_{yy} - \left(\sigma_{yy}\right)_{T=0}}{\sigma_o} \tag{2-26}$$

where δ_{ij} is the Kronecker delta.

3.
Standard procedures to measure fracture toughness

With the goal to measure fracture toughness under LE or EP conditions, ASTM developed its E1820 standard [7], which lists procedures and guidelines to obtain properties like e.g. J_{Ic}. Its test procedures specify how to load fatigue pre-cracked specimens until forcing unstable or stable crack extension (Section 3.1.1). This work focus is on stable crack extension by crack tearing. Fracture toughness results from the *J-R* curve that relates applied *J*-integral values with crack increments. The standard provides two methods for measuring crack increments, the basic and the resistance curve procedures. The basic procedure requires multiple specimens to develop a plot from which a single toughness value associated with crack tearing initiation can be evaluated. The resistance curve procedure requires only a single specimen in which successive crack increments are measured using the elastic unloading compliance method (see Section 3.1.2). In this thesis, the chosen procedure is the compliance technique, because level 3 of the API 579 fitness-for-purpose guide requires a well-defined crack tearing resistance curve to characterize the material toughness. Finally, it should be mentioned that there are many other standards for measuring fracture toughness, for instance, ASTM E399 [5], ASTM E1290 [6], BS 7448 [8], and EFAM GTP [9].

3.1
Fracture toughness specimens

ASTM E1820 recommends Single Edge Notched Bend SE(B), Compact Tension C(T), and Disk-Shaped Compact Tension DC(T) specimens, see Figs. 3.1, 3.2, and 3.3. The ratio between specimen width (*W*) and thickness (*B*) must be $1 \leq W/B \leq 4$ for SE(B), and $2 \leq W/B \leq 4$ for C(T) and DC(T). For *J-R* curve measurements, these specimens must obey:

- $J_{max} > b_o \sigma_Y/10$ or $J_{max} > B\sigma_Y/10$, whichever is smaller, and

- $\Delta a_{max} = 0.25b_o$

where b_o is the original remaining ligament and σ_Y is the effective yield strength, also known as the flow strength, which is the mean of the 0.2% offset yield strength σ_{ys} and the ultimate tensile strength σ_{us},

$$\sigma_Y = \frac{\sigma_{ys} + \sigma_{us}}{2} \tag{3-1}$$
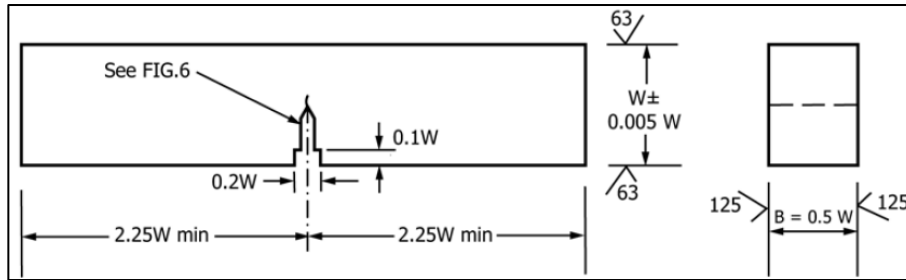

Figure 3.1: Standard SE(B) specimen [7].
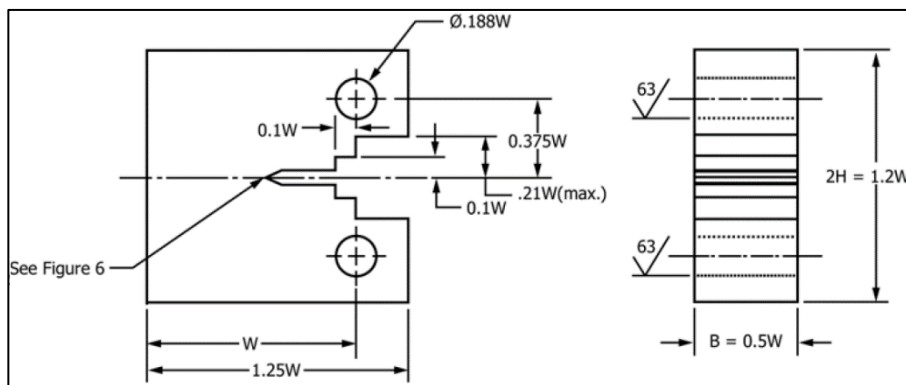
Figure 3.2: Standard C(T) specimen [7].
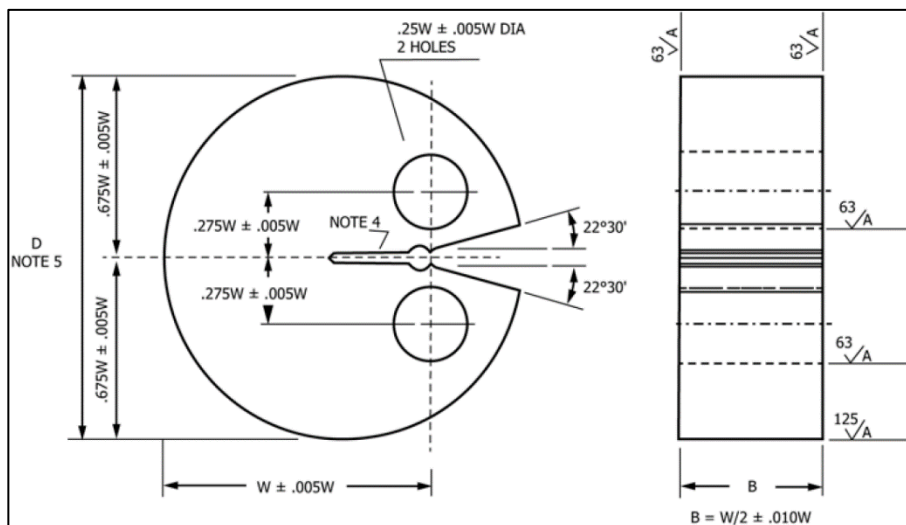
Figure 3.3: Standard DC(T) specimen [7].

3.1.1
Fatigue pre-cracking procedures

All fracture toughness specimens must have a proper fatigue pre-crack. The pre-crack length/specimen width ratio must be $0.45 \leq a/W \leq 0.70$. However, there is an annex on the standard for shallow cracks, which accepts pre-cracks with $0.05 < a/W < 0.45$. The fatigue pre-crack length includes the notch length or part of it, and the fatigue crack itself shall be larger than 0.25 mm to avoid geometry effects caused by the notch. To induce the pre-crack in e.g. SE(B) specimens, ASTM E1820 specifies a maximum fatigue force P_m:

$$P_m = \frac{0.5 B b_o^2 \sigma_Y}{S} \qquad (3\text{-}2)$$

where S is the support span ($S = 4W$), B is the specimen thickness, b_o is the original remaining ligament, which is the distance between the notch plus the pre-crack a_o to the back edge of the specimen, $b_o = W - a_o$. There are similar requirements for the other specimens accepted by the standard.

3.1.2
Resistance curve procedures

Fracture toughness can be measured according to ASTM E1820 procedures by *J-R* or *δ-R* resistance curves, using elastic unloading compliance techniques to evaluate *J* or *δ* and to obtain crack increments during the crack tearing phase of a single specimen. The standard recommends side grooves in the specimens to avoid crack tunneling and shear lips, and to promote a plane strain state and a straight crack front during the test. The thickness reduction for this side groove is limited to $0.25B$. Figure 3.4 shows the grooved specimen thickness B_N, which is the distance between the side groove roots.

Fatigue pre-cracks should be induced before the side-grooving operation. Grooving the side notches before fatigue pre-cracking significantly affects the plastic zone growth. Flat specimens have a *pz* with considerable size variation along the tip front. Near the specimen surfaces, *pz*s grow under predominant plane stress conditions. For the grooved specimens, *pz*s are developed first near the roots of the grooves and then extend along the tip front [42].
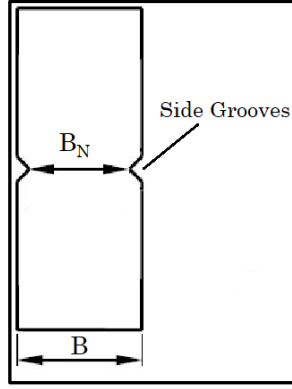
Figure 3.4: Side grooves [28].

The fracture toughness measured using the compliance technique depends on the side grooves and specimen thickness [43]. The resistance curve increases with the decreasing of the thickness, which makes the *pz* relatively larger. On the contrary, the fracture resistance decreases with the use of side grooves, making it a conservative operation.

Compliance procedures require loading the pre-cracked specimen with continuous measurement of the Crack Mouth Opening (CMOD) or Load-Line Displacement (LLD) to evaluate the resistance curve. First, it is necessary to load the specimen to P_m. Then estimate the provisional initial crack size a_{oq} with at least three unloading/reloading sequences with a force range of $0.5P_m$, 50 to 100% P_m. After that, similar unload/reload sequences are used to evaluate crack increments, with an average displacement gap between each one of those sequences $\Delta a \cong 0.005b_o$. At least eight such sequences must be used before reaching the maximum force. The maximum range of the unloading sequence should not exceed either $0.5P_m$ or 50% of the current force. 0.1-$0.2P_m$ on unloading sequences usually provide satisfactory results. From the compliance C measured in such unloading-reloading sequences, it is possible to estimate the crack size in each one of them using Eqs. 3-3, 3-4, and 3-5, see Fig. 3.5.

$$\frac{a_{(i)}}{W} = 0.999748 - 3.9504u + 2.9821u^2 - 3.21408u^3 +$$
$$51.51564u^4 - 113.031u^5 \tag{3-3}$$

$$u = \frac{1}{\left[\dfrac{B_e W E C_{(i)}}{S/4}\right]^{1/2} + 1} \tag{3-4}$$

$$C_{(i)} = \frac{\Delta CMOD}{\Delta P} \tag{3-5}$$

where E is Young's Modulus and B_e is the effective thickness of the side grooved specimens,

$$B_e = B - \frac{(B - B_N)^2}{B} \tag{3-6}$$
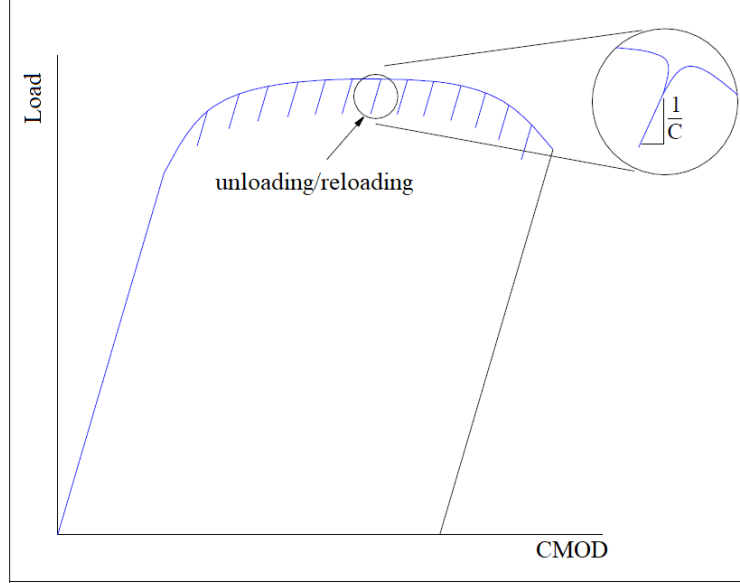
Figure 3.5: Compliance technique [28].

The standard does not specify which data points from an unload-reload cycle should be used to calculate the specimen compliance. It is up to the user to decide whether to use all of the data or some specific portion of it. Chapter 4.5.1 explains in detail the procedure used in this work to calculate compliance. With the crack length and the applied force, it is possible to calculate the stress intensity factor K for each unloading as follows:

$$K_{(i)} = \left[\frac{P_{(i)}S}{(BB_N)^{1/2}W^{3/2}} \right] f(a_{(i)}/W) \tag{3-7}$$

$$f\left(\frac{a_{(i)}}{W}\right) = \tag{3-8}$$

$$\frac{3\left(\frac{a_{(i)}}{W}\right)^{1/2}\left[1.99 - \left(\frac{a_{(i)}}{W}\right)\left(1 - \left(\frac{a_{(i)}}{W}\right)\right)\left(2.15 - 39.3\left(\frac{a_{(i)}}{W}\right) + 2.7\left(\frac{a_{(i)}}{W}\right)^2\right)\right]}{2\left(1 + \left(\frac{a_{(i)}}{W}\right)\right)\left(1 - \left(\frac{a_{(i)}}{W}\right)\right)^{3/2}}$$

Finally, the *J* integral is incrementally calculated in each unloading-reloading sequence, since the crack size increases, by the following equations:

$$J_{(i)} = J_{el(i)} + J_{pl(i)} \tag{3-9}$$

$$J_{el(i)} = \frac{K_{(i)}^2 (1 - v^2)}{E} \tag{3-10}$$

$$J_{pl(i)} = \left[J_{pl(i-1)} + \left(\frac{\eta_{(i-1)}}{b_{(i-1)}} \right) \left(\frac{A_{pl(i)} - A_{pl(i-1)}}{B_N} \right) \right] \times$$
$$\left[1 - \gamma_{pl(i-1)} \left(\frac{a_{(i)} - a_{(i-1)}}{b_{i-1}} \right) \right] \tag{3-11}$$

where v is Poisson's ratio and A_{pl} is the increment of plastic area illustrated in Fig. 3.6, given by Eq. 3-12. The plastic area is a function of plastic displacement v_{pl}, calculated using Eq. 3-13.

$$A_{pl(i)} = A_{pl(i-1)} + \left[P_{(i)} + P_{(i+1)} \right] \left[v_{pl(i)} - v_{pl(i-1)} \right] / 2 \tag{3-12}$$

$$v_{pl(i)} = CMOD_{(i)} - \left(P_{(i)} C_{(i)} \right) \tag{3-13}$$
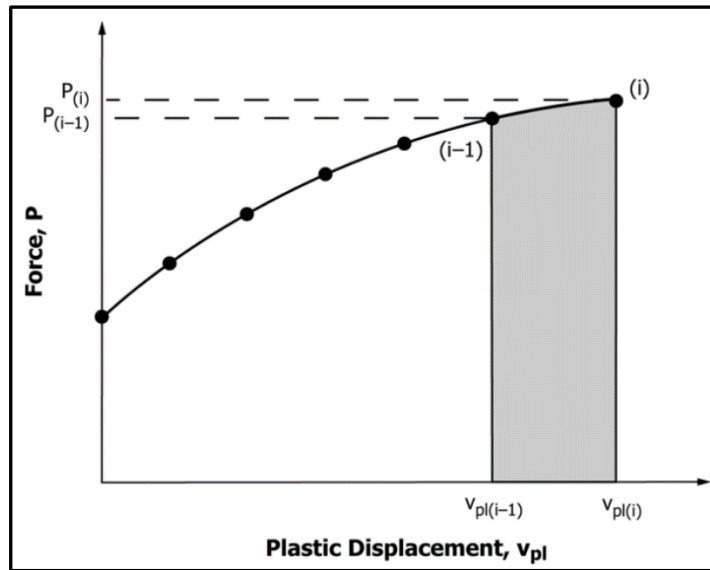
Figure 3.6: Plastic area [7].

The non-dimensional parameters η_{pl} and γ_{pl} relate the plastic work with the *J* integral and the crack growth effect on it as given by Eqs. 3-13 and 3-15:

$$\eta_{pl(i-1)} = 1.9 \tag{3-14}$$

$$\gamma_{pl(i-1)} = 0.9 \tag{3-15}$$

In the case, LLD is used to measure A_{pl},

$$\eta_{pl(i)} = 3.667 - 2.199\frac{a_{(i-1)}}{W} + 0.437\left(\frac{a_{(i-1)}}{W}\right)^2 \qquad (3\text{-}16)$$

If CMOD is used instead,

$$\gamma_{pl(i)} = 0.131 - 2.131\frac{a_{(i-1)}}{W} - 1.465\left(\frac{a_{(i-1)}}{W}\right)^2 \qquad (3\text{-}17)$$

It is necessary to correct the initial crack size a_{oq} estimated by unloading compliance technique to get more accurate crack extension Δa_i estimates. This is important because Δa_i values have a considerable influence on the J_{Ic} result. To adjust a_{oq}, it is necessary to use all J_i and a_i points on Eq. 3-18, where the coefficients $\overline{B}$ and $\overline{C}$ can be found by a least-squares fit procedure.

$$a = a_{oq} + \frac{J}{2\sigma_Y} + \overline{B}J^2 + \overline{C}J^3 \qquad (3\text{-}18)$$

With J integral and adjusted crack extension $\Delta a = a_{(i)} - a_{oq}$ results, it is possible to generate the *J-R* curve as shown in Fig. 3.7. To evaluate J_{Ic}, it is necessary to take into account some construction, exclusion, and offset lines determined by the ASTM E1820. The construction line represents the first subcritical stages of crack growth and it is given by the following equation.

$$J = 2\sigma_Y\Delta a \qquad (3\text{-}19)$$
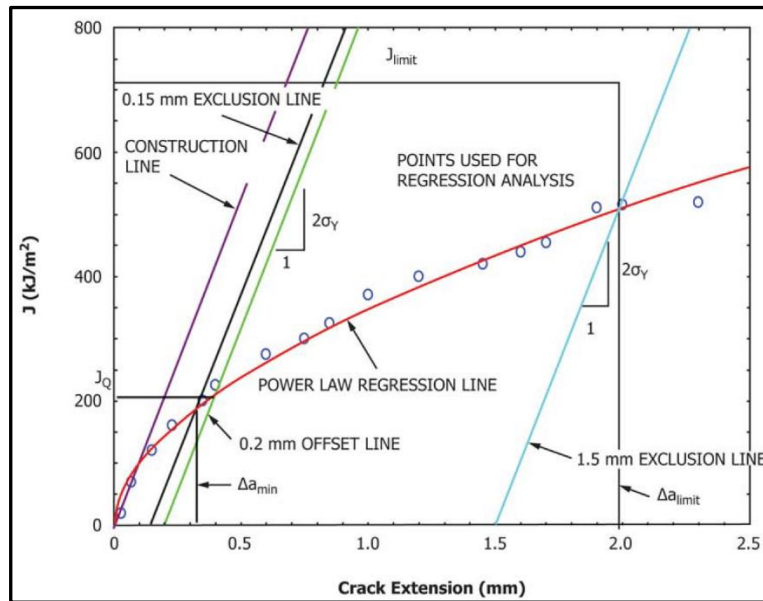
Figure 3.7: *J-R* curve with constructions lines [7].

The exclusion lines are parallel to the construction line and intersect the abscissa at $\Delta a = 0.15$ and $\Delta a = 1.5$ mm. The values of Δa_{min} and Δa_{limit} are defined with the intersection of exclusion lines and the *J-R* curve. The data points outside this range, and above the J_{limit} defined by the Eq. 3-20 are excluded.

$$J_{limit} = b_o \sigma_Y / 7.5 \qquad (3\text{-}20)$$

The offset line is also parallel to the construction line and intersects the abscissa at $a = 0.2$ mm. It is necessary that at least one data point to lie between the 0.15 exclusion line and the 0.5 offset line (Region of qualified data A). Also, at least one data point shall lie between the 0.5 offset and 1.5 exclusion line (Region of qualified data B). The acceptable points are shown in Fig. 3.8.
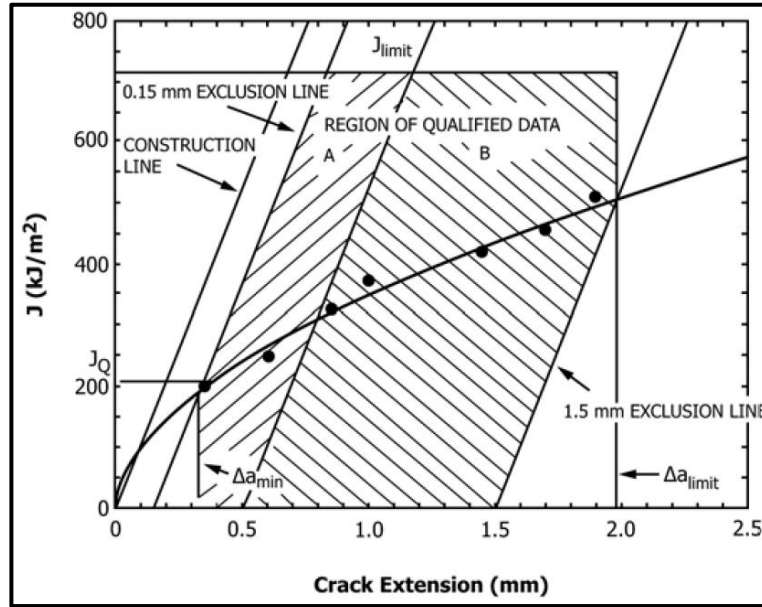
Figure 3.8: Regions for data qualification [7].

At least five data points must remain between Δa_{min}, Δa_{limit}, and J_{limit}. Using the data points inside this region, it is necessary to develop a linear regression line with the least-square method to obtain *J* using the following equation.

$$J = C_1 \left(\frac{\Delta a}{k}\right)^{C_2} \qquad (3\text{-}21)$$

where C_1 and C_2 are constants and $k = 1$ mm. Fig. 3.7 illustrates all construction, offset, and exclusion lines, as well as the regression line. The intersection of the

0.2 offset and the regression lines defines J_{Ic} and Δa_{Ic}. For the qualification of the data, the following requirement must be satisfied:

- $B > 10J_{Ic}/\sigma_Y$

- $b_o > 10J_{Ic}/\sigma_Y$

Finally, it is possible to evaluate K_{JIc} by the following equation.

$$K_{JIc} = \sqrt{\frac{EJ_{Ic}}{1 - v^2}} \qquad\qquad (3\text{-}22)$$

3.1.3
Optical crack size measurements

After finishing the *J-R* test, it is necessary to break the specimen with care to minimize additional deformations, e.g. cooling it in liquid nitrogen to ensure brittle fractures. The crack front must be divided into nine equally spaced points centered about the specimen centerline, extending it to $0.005W$ from the side groove root, or the surface of plane-sided specimens. Next, the size of the fatigue pre-crack a_o and the stable crack extension a_p must be measured in each section. The difference between the measured a_o and the estimated a_{oq} shall not be more than $0.01W$ or 0.5 mm. Using the mean in each section, it is possible to estimate the physical crack increment $\Delta a_p = a_p - a_o$. None of these measurements shall differ by more than $0.05B$.

3.2
Procedure for SE(T) specimens

Standardized specimens have high transversal constraints, and thus yield conservative values of fracture toughness for use in less constrained geometries like cracked pipes or pressure vessels much used in the petroleum industry. It is necessary to use specimens with similar conditions to simulate their fracture process in the laboratory. A good candidate for that is the SE(T) specimen since it has a strong similarity in crack-tip stress and strain fields to the mentioned structures. This specimen is already being widely used in the marine industry to measure toughness.

In this work, less constrained fracture toughness measurements on clamped SE(T) specimens follow the procedures developed by Cravero and Ruggieri [21]. This method also evaluates *J-R* curves using the compliance technique. Using results from finite element analyses and the least square method, these authors proposed a fifth-order polynomial equation (Eq. 3-23) to estimate crack length inside the range $0.1 \leq a/W \leq 0.7$ on pin-loaded and clamped SE(T) specimens. For pin-loaded specimens, the compliance u is independent of *H/W* ratio, where *H* is the distance between loading points. For clamped specimens, it depends on *H/W* ratios for cracks deeper than $0.4a/W$. The normalized compliance is given by Eq. 3-24 [44].

$$a/W = \beta_0 + \beta_1 u + \beta_2 u^2 + \beta_3 u^3 + \beta_4 u^4 + \beta_5 u^5 \qquad (3\text{-}23)$$

$$u = \frac{1}{1 + \sqrt{E'BC}} \qquad (3\text{-}24)$$

where β_i are coefficients given for each type of SE(T) specimen and *H/W* ratio. If side grooves are used, it is necessary to change the value of *B* to B_e as in Eq. 3-24.

Shen et al. [45] also developed a solution to estimate crack lengths that covers crack sizes over the range $0.05 \leq a/W \leq 0.95$. However, its ninth order polynomial equation makes it difficult to use on finite elements analyzes. Moreover, to calculate the elastic SIF K_I by Eq. 3-25, it is necessary to know the non-dimensional geometry factor *f(a/W)* of the specimen. Several studies show how to estimate this geometry factor on SE(T) specimens, but these results have a limited range of *a/W* and *H/W* ratios. Cravero and Ruggieri developed the fifth-order polynomial Eq. 3-26 to cover many geometries and loading eccentricities on pin-loaded and clamped SE(T).

$$K_I = \frac{P}{B\sqrt{(W)}} f(a/W) \qquad (3\text{-}25)$$

$$f(a/W) = \xi_0 + \xi_1(a/W) + \xi_2(a/W)^2 + \xi_3(a/W)^3 + \\ \xi_4(a/W)^4 + \xi_5(a/W)^5 \qquad (3\text{-}26)$$

where ξ_i are coefficients given for each type of SE(T) specimen, *H/W* ratio, and loading point offset (LPO).

Finally, the parameters η_{pl} and γ_{pl}, which depend on the computation of A_{pl} in Eq. 3-11, are also reevaluated for SE(T) specimens. Cravero and Ruggieri analyzed these parameters using numerical experiences to evaluate the effect of loading conditions and hardening properties. They concluded that η_{pl} obtained from load versus CMOD curves is independent of hardening properties, and it is less sensitive to the loading level when compared with η_{pl} obtained from load versus LLD curves. The following equations provide polynomial fits for η_{pl} on clamped SE(T) specimen obtained from load versus CMOD curves (Eq. 3-27) and from load versus LLD curves (Eq. 3-28). The polynomial fit of γ_{pl} (Eq. 3-29) works for both curves.

$$\eta_C^{CMOD} = 1.0398 - 0.6870(a/W) \tag{3-27}$$

$$\eta_C^{LLD} = A + B(a/W) + C(a/W)^2 + D(a/W)^3 \tag{3-28}$$

$$\gamma_C = (A-1) + B(a/W) + C(a/W)^2 + D(a/W)^3 +$$
$$\frac{-B + (B-2C)(a/W) + (2C-3D)(a/W)^2 + 3D(a/W)^3}{A + B(a/W) + C(a/W)^2 + D(a/W)^3} \tag{3-29}$$

4.
Experimental procedures and material characterization

This chapter describes the tests performed on the API 5L X80 steel to measure its mechanical properties needed in structural integrity analyses. All specimens came from the same flat plate with 1100 mm length, 800 mm width, and 21.85 mm thickness, as illustrated in Fig. 4.1. The specimens were cut in a water jet machine to avoid heat-affected zones (HAZ) that could affect the properties. Since the surface finish of the cuts is irregular, it was improved using a milling machine. The experiments conducted in this work were:

- Metallography

- Chemical analysis

- Hardness test

- Tensile test

- J_{Ic} fracture toughness test

4.1
Metallography

A 20×20×21.85 mm sample was cut from the steel plate steel for the metallographic analysis. The sample surface was abraded with 150, 240, 320, 400, and 600 grit sandpaper, and then it was polished with diamond pastes of 6, 3, and 1μm in an Arotec metallographic polishing machine, see Fig. 4.2(a). The sample (Fig. 4.2(b)) was cleaned in alcohol, air dried, etched with 2% nital, and finally analyzed using an Axio ZEISS A1 optical microscope, see Fig. 4.2(c).

The X80 longitudinal and transversal microstructures are shown in Fig. 4.3(a) and (b). Due to the anisotropy caused by lamination, the microstructure is slightly different in these two directions. The longitudinal grains are elongated when compared to the transversal grains. The X80 microstructure is composed by polygonal ferrite, quasi-polygonal ferrite, acicular ferrite,

granular bainite-ferrite, and a small amount of martensite-austenite islands [46]-[47].
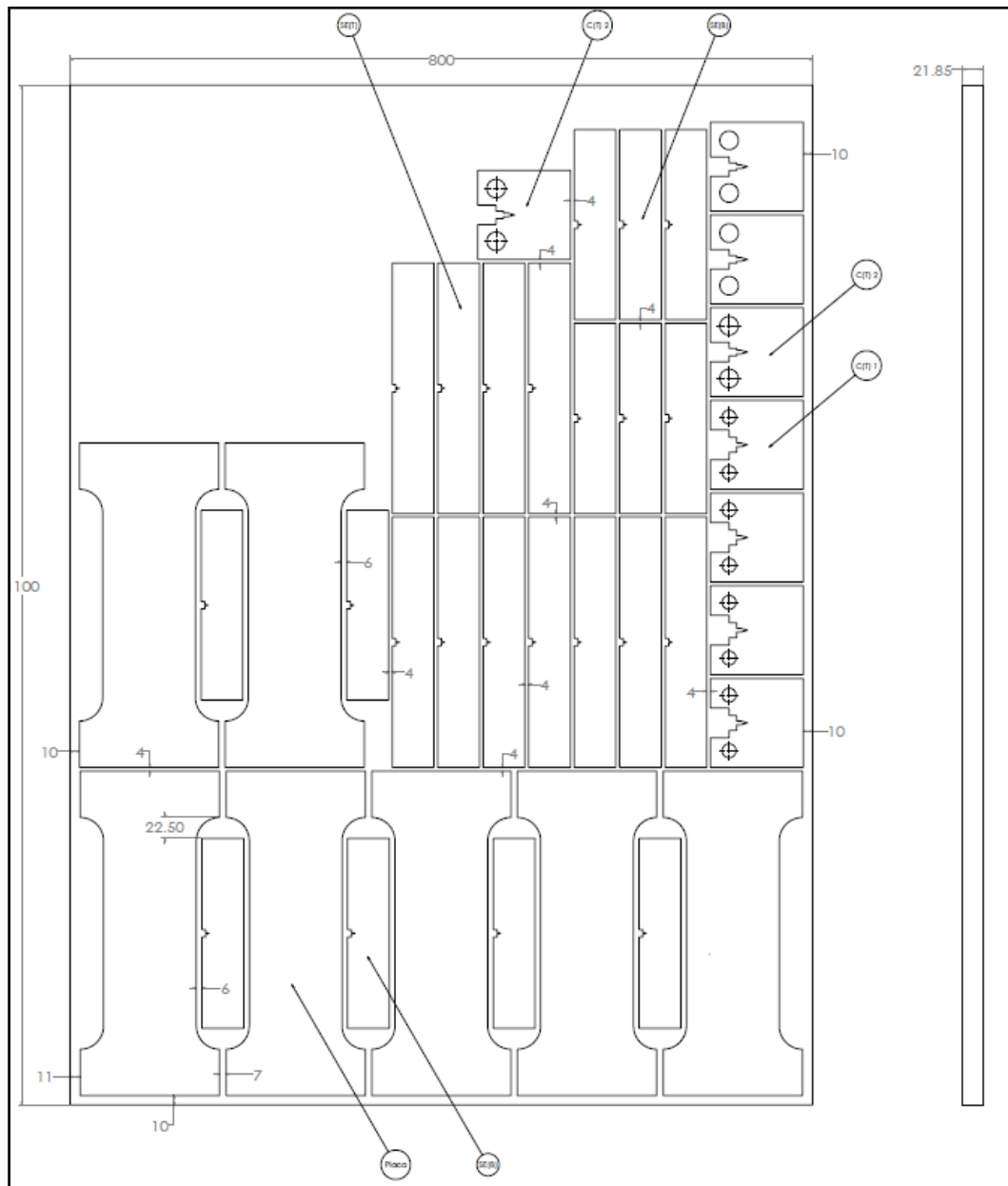
Figure 4.1: API 5L X80 flat plate.

4.2(a): Polishing machine.   4.2(b): Sample.   4.3(c): Axio.

Figure 4.2: Metallographic analysis.

4.3(a): Longitudinal   4.3(b): Transversal
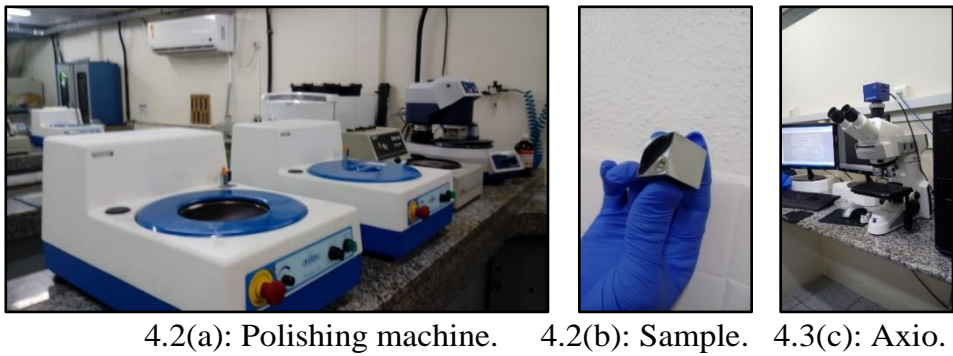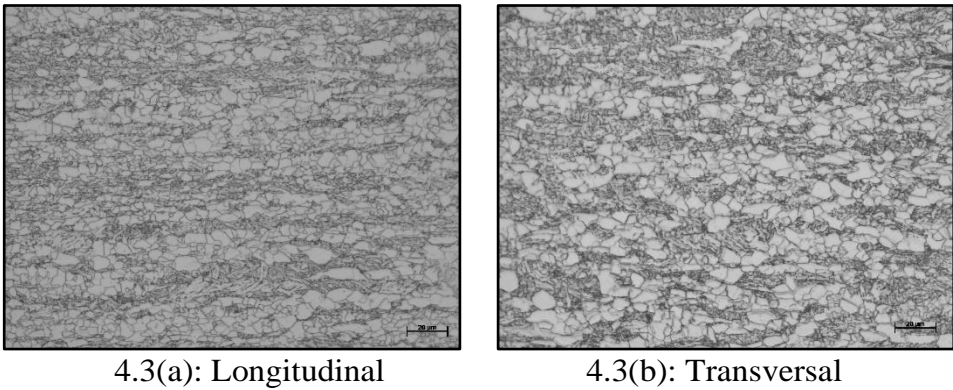
Figure 4.3: Microstructure of API 5L X80 steel (magnification 500x).

4.2
Chemical analysis

A semi-quantitative chemical analysis was performed using a Genius 7000 XRF Handheld Spectrometer, see Fig. 4.4.
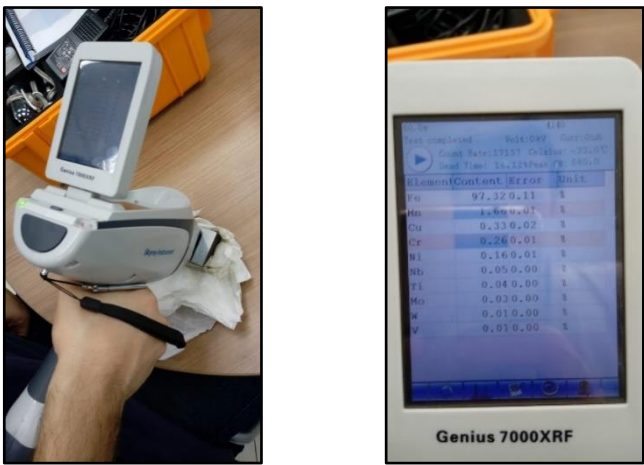

Figure 4.4: Chemical analysis.

Four measurements were taken on the X80 sample. This equipment does not measure the carbon content, which would require a not affordable chemical analysis, but it can identify Fe, Mn, Cr, Ni, Nb, Ti, Mo, W, V, see Table 4.1. Table 4.2 shows the nominal chemical composition of the API 5L X80 provided by USIMINAS and by Confab [48]. Table 4.3 lists the chemicals compositions limits by API for pipe fabrication. The Cu measured with the spectrometer is misleading, that was a consequence of the poor equipment configuration.

Table 4.1: Chemical analysis of the API 5L X80 sample.

Fe	Mn	Cu	Cr	Ni	Nb	Ti	Mo	W	V
97.27	1.68	0.36	0.26	0.15	0.07	0.05	0.04	0.02	0.01

Table 4.2: API 5L X80 nominal chemical composition [48].

Chemical Composition (%mass)											
Cod.	C	Mn	Si	Al	Nb	V	Cr	Ni	Mo	Ti	N	Ceq
45	0,07	1,76	0,18	0,028	0,071	0,005	0,20	0,02	0,16	0,014	0,0062	0,19
46	0,04	1,75	0,17	0,032	0,073	0,005	0,21	0,02	0,16	0,013	0,0035	0,16
51	0,04	1,85	0,18	0,033	0,073	0,005	0,32	0,02	0,03	0,016	0,0037	0,16
52	0,04	1,86	0,19	0,032	0,075	0,006	0,33	0,02	0,03	0,017	0,0049	0,16

Mechanical Properties				
Cod.	σ_{ys} [MPa]	σ_{us} [MPa]	A_T [%]	CVN $_{(-20°C)}$ [J]	Cod. 45 e 46: Nb-Cr-Mo
45	512	662	27	176	
46	543	671	27	224	Cod. 51 e 52: Nb-Cr
51	550	676	27,5	232	
52	523	642	27,5	221	

Table 4.3: API 5L X80 chemical limits provided by API in 2004 [49].

(1)	(2)	(3)	(4)	(5)	(6)
Grade	Carbon, Maximum[a]	Manganese, Maximum[a]	Phosphorus, Maximum	Sulfur, Maximum	Titanium, Maximum
Seamless					
B	0.24	1.20	0.025	0.015	0.04
X42	0.24	1.30	0.025	0.015	0.04
X46, X52, X56, X60[f]	0.24	1.40	0.025	0.015	0.04
X65[f], X70[f] X80[f]	0.24	1.40	0.025	0.015	0.06
Welded					
B	0.22	1.20	0.025	0.015	0.04
X42	0.22	1.30	0.025	0.015	0.04
X46, X52, X56	0.22	1.40	0.025	0.015	0.04
X60[f]	0.22	1.40	0.025	0.015	0.04
X65[f]	0.22	1.45	0.025	0.015	0.06
X70[f]	0.22	1.65	0.025	0.015	0.06
X80[f]	0.22	1.85	0.025	0.015	0.06

4.3
Hardness test

Vickers hardness was measured with the equipment shown in Fig.4.5. Four measurements were performed with an average 226.5HV. Looking at DIN 50150 hardness conversion table [50], this value corresponds to a tensile strength of 720 MPa.

Figure 4.5: Hardness test.

4.4
Tensile test

Tensile properties were measured according to E8/E8M procedures [24]. Three specimens were cut in both directions, transversal and longitudinal to the plate. Fig. 4.6 shows the specimen dimensions.
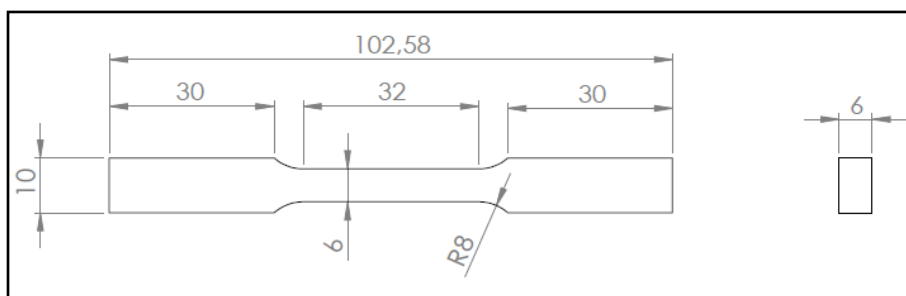

Figure 4.6: Tensile specimens dimensions.

The tests were made the 100kN INSTRON illustrated in Fig. 4.7(a). The test speed was 2 mm/min, and a 25 mm clip gage was used to measure the strains. Fig. 4.7(b) and 4.7(c) show the specimens before and after the tests.

4.7(a): Tensile test machine.

4.7(b): Specimens before the tests.   4.7(c): Specimens after the tests.

Figure 4.7: Tensile test.

Fig. 4.8 shows the engineering and Fig. 4.9 shows the true stress/strain curves measured. Specimens T1 and T3 necked outside the clip gage, resulting in a significant stress drop after the peak engineering stress, see Fig. 4.8.
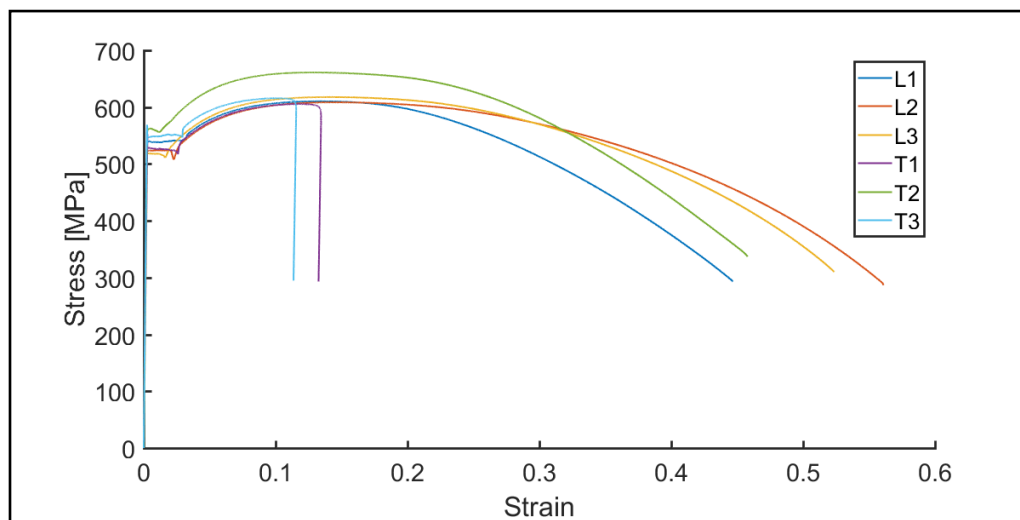

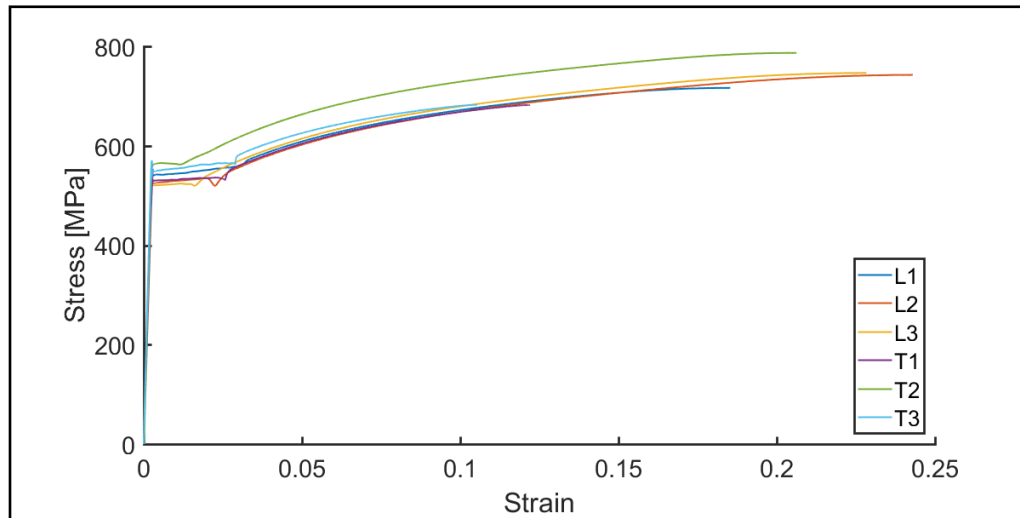Figure 4.8: Engineering stress/strain curves.

Figure 4.9: True stress/strain curves.

Average Young modulus E, yield strength σ_{ys}, ultimate tensile strength σ_{us}, and Ramberg-Osgood (Eq. 4-1) parameters are listed in Table 4.4.

$$\epsilon = \frac{\sigma}{E} + \left(\frac{\sigma}{H}\right)^{1/h} \tag{4-1}$$

Table 4.4: Tensile average properties results of API 5L X80.

	E [GPa]	σ_{ys} [MPa]	σ_{us} [MPa]	H [MPa]	h
Longitudinal	223	527	612	946	0.148
Transversal	231	546	627	954	0.139

Due to uneven distribution of carbide-rich microstructural constituents, the microscopic and macroscopic textures have a subtle influence on the anisotropy of properties of the API 5L X80 steel [51].

4.5
Fracture toughness test

Fracture toughness tests followed ASTM E1820-17 procedures for SE(B) and Cravero and Ruggieri recommendations for SE(T) specimens, which were all taken from the longitudinal direction of the steel plate. Hence, the cracks grew on its transversal direction. The specimen with an ultra-narrow notch was

machined on a wire-cut Electric Discharge Machine (EDM). SE(B)s had length
$L = 205$mm, width $W = 45$mm, and thickness $B = 21.85$mm, see Fig. 4.10. SE(T)
had the same width and thickness but a length $L = 270$mm, see Fig. 4.11. Fig.
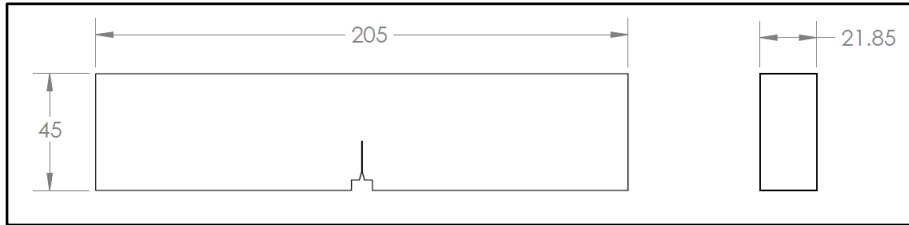4.12 shows specimens ready for the tests.
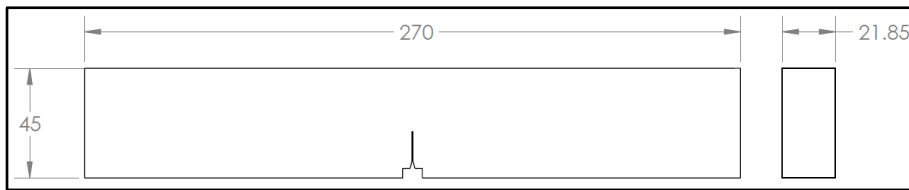

Figure 4.10: SE(B) specimen dimensions in mm.

Figure 4.11: SE(T) specimen dimensions in mm.

Figure 4.12: SE(B) and SE(T) specimens ready for testing.

4.5.1
SE(B) specimens

Initially, four SE(B) specimens were machined with an *a/W* = 0.55 ratio,
which is in the middle of the allowance range given by the standard. The
nominal support span for the experiments is *S* = 180 mm. The EDM notch size
indicated in Figs. 4.10 and 4.11 is 20 mm. All SE(B) tests were performed on a
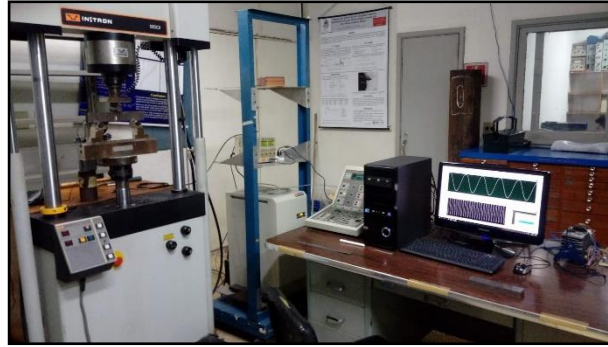100 kN INSTRON 8501 servo-hydraulic testing machine, as shown in Fig 4.13.

Figure 4.13: INSTRON 8501 servo-hydraulic testing machine (100 kN).

To initiate fatigue cracks in three-point bending tests the maximum load was 90% of the P_m given by Eq. 3-2, with an $R = P_{min}/P_{max} = 0.1$, at a frequency of 25 Hz. Once the crack started to grow, the frequency was reduced to analyze its growth with a microscope until the desired a/W ratio. The crack length was measured during the experiment by calculating the number of pixels in a picture using a scale rule near the crack, as shown in Fig. 4.14.

The unloading compliance procedure of the ASTM E1820 was used to measure fracture toughness. The clip gage for these tests on this material should have a 12 mm range. However, such a clip gage was not available, and the initial tests used a clip gage with only a 5 mm range. Besides, the automatic control of the test machine was not working properly. Thus, all experiments were operated manually with Load Line Displacement (LLD) control. The LLD control is not ideal because it is not accurate enough to measure crack increments Δa. LLD is affected by the machine flexibility and oscillations in the hydraulic actuator. Thus, the initial tests under LLD control used a low speed of 0.01 mm/s to allow the reading of CMOD values made by the data acquisition software written in LabVIEW. Every time it reached the desired force or CMOD, the LLD direction was manually changed to apply the unloading or reloading.
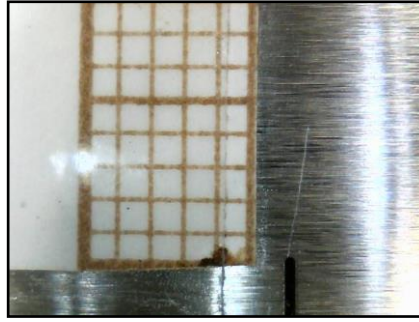
Figure 4.14: Pre-crack measurement.

In the initial tests, the force used to generate the fatigue pre-crack was higher than the P_m allowed by the standard, due to a calculation error. Then, the fatigue pre-cracking could generate a plastic zone at the crack tip that could prevent tearing. The SE(B)-1 data was lost due to this data collection problem. The unloading compliance using the described manual control on SE(B)-2 and SE(B)-3 with $a/W = 0.55$ are shown in Fig. 4.15. A range $\Delta P = 0.75 P_m$ was used in the first sequence of three unloadings, whereas the following partial unloadings used a range $\Delta P = 0.2 P_m$. Such single unloadings were spaced by 0.1 mm CMOD increments. The tests finished when the maximum range of the clip gage (5 mm) was reached.

The region between the two red lines illustrated in Fig. 4.16 was selected to calculate the compliance during the EP toughness tests (Eq. 3-5). This corresponds to the part below the material relaxation, and above the part where the machine stops to change direction. The region of each sequential unloading was visually chosen to minimize the effect of the experimental parameters that can affect the compliance result. The RANSAC method was used to calculate the compliance of each unloading [52], considering all the points of a specified region. With this method, it is possible to define the best line to represent the scatter data. RANSAC is more robust than the least square method, as demonstrated in Fig. 4.17. In that case, the too disperse points do not have a significant impact on the compliance result.
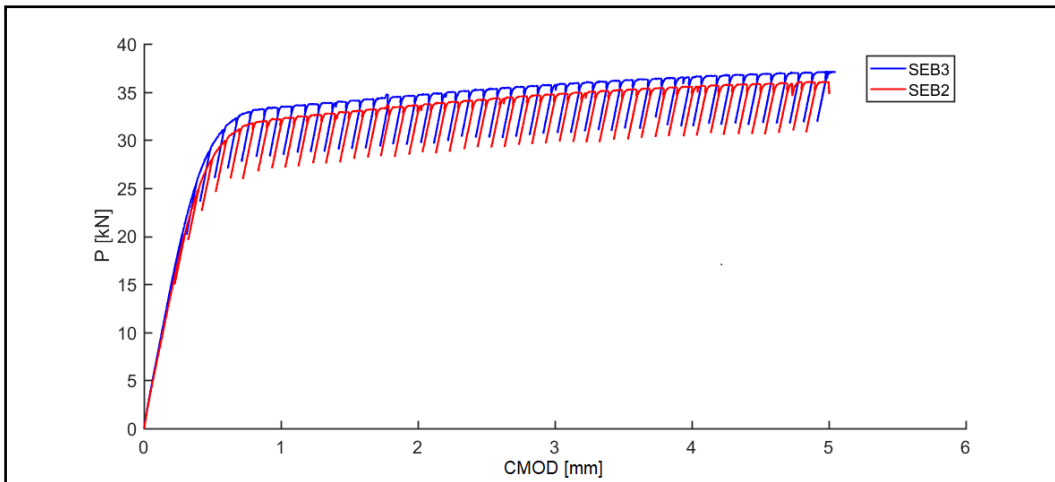
Figure 4.15: Unloading compliance SE(B)-2 and SE(B)-3.
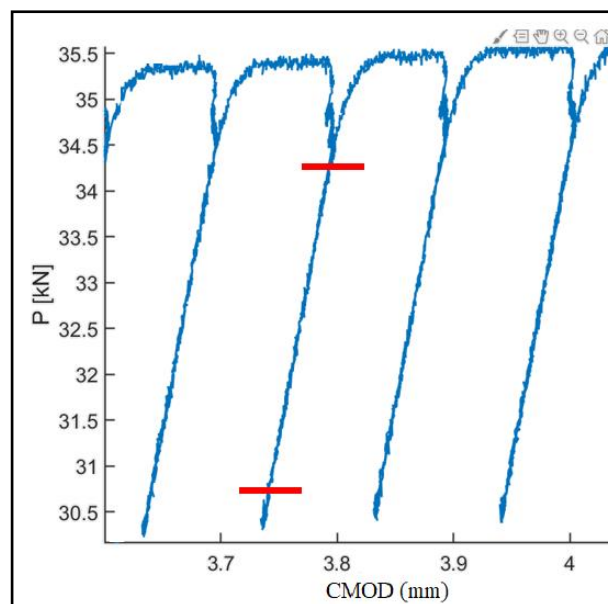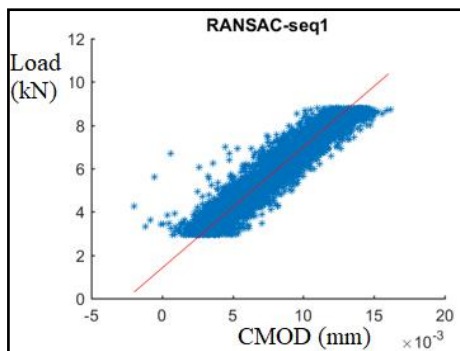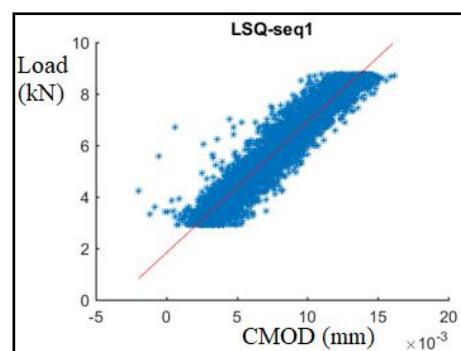

Figure 4.16: Unloading compliance range.

4.17(a): Least square.   4.17(b): RANSAC.

Figure 4.17: Compliance method calculation.

All unloading compliance tests were manually controlled via the machine LLD. Hence, the tests were executed at low speed so that the operator could stop the LLD at the determined load or CMOD calculated by the LabVIEW program. During the unloading, it was necessary to manually calculate the minimum force each time to define when to stop the LLD using the same ΔP (20% of P_m). During the loading, the focus was on the CMOD value, to see when to stop the machine once it reached a CMOD distance of 0.1 mm.

Figures 4.18 and 4.19 show the *J-R* curve of SE(B) 2 and 3, respectively. They show that it was not possible to apply the procedure specified by the ASTM standard to find J_{Ic}. There were not enough points after the 0.2 mm offset line. According to the standard and these graphs, there was no tearing in this material to measure J_{Ic}. Thus, to develop the resistance curve, it was decided to use all the points given by the unloading compliance.
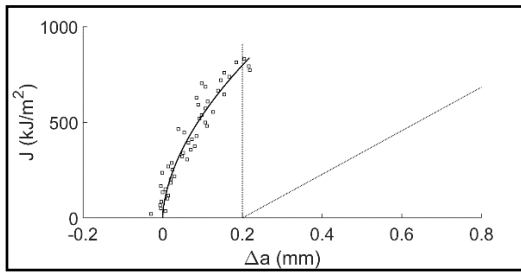

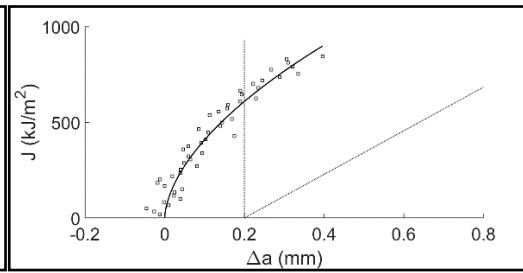Figure 4.18: *J-R* Curve SE(B)-2.   Figure 4.19: *J-R* Curve SE(B)-3.

To confirm if crack initiation occurred or not, the steel specimens were submerged in liquid nitrogen, to embrittle them. Then, using the same servo-hydraulic machine to break the two specimens, it was possible to observe that there was no crack extension. The fatigue pre-crack tip was blunt, but there was no crack tearing. Another substantial factor in this image is that it shows a notable crack front curvature. The crack propagated faster in the center than near the surface. This is caused by the high stress triaxiality at the center section, which promotes void nucleation, growth, and coalescence [53]. This effect is also known as tunneling, and it is common in ductile fracture experiments.
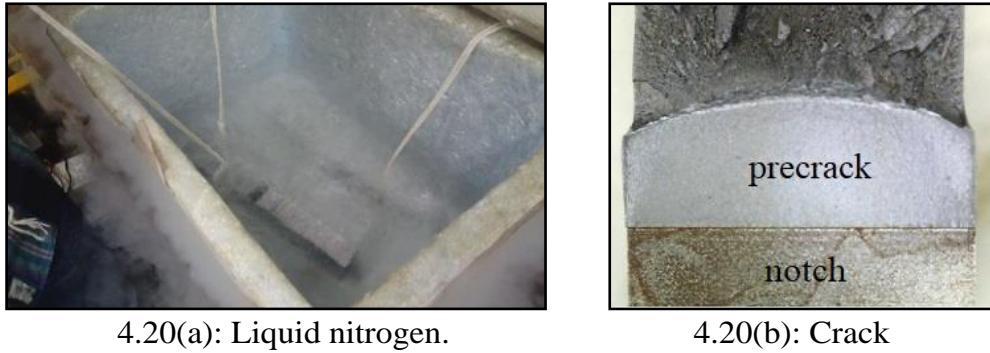
4.20(a): Liquid nitrogen.

4.20(b): Crack

Figure 4.20: Brittle fracture.

The SE(B)-4 specimen used the same procedure applied on SE(B)-2 and 3 to propagate the fatigue pre-crack with $a/W = 0.55$ ratio. Since these previous specimens had no tearing phase, it was necessary to correct the pre-cracking mistake (initially made with a force higher than P_m). The plastic zone generated during the pre-cracking was probably one of the reasons that the cracks did not tear on the previous tests. As an attempt to fix this situation, it was decided to continue fatigue cycling with a maximum load of 90% of P_m, but this time with the right value for P_m. The idea was to increase the crack size to overcome the generated plastic zone. Thus, the new $a/W = 0.65$ ratio is still in the allowable range for the standard.

Furthermore, the clip gage with only 5 mm range was another factor that could affect the results. For this reason, the next experiments used two clip gages instead of one, to obtain a 9 mm range. The idea is to use the first clip gage with an opening from 1 mm to 5 mm. Once it reaches 5 mm, stop the experiment and change the clip gage to another with an opening from 3 mm to 10 mm. This is not the ideal, but it was what was available at the moment. From that time on, the next unloading compliance experiments had a maximum CMOD of 9 mm.

Fig. 4.21 shows the SE(B)-4 unloading compliance. As illustrated, there was a small instantaneous loading drop during the test near 6 mm of CMOD. This pop-in can be justified due to the formation of splits or, to put it another way, secondary cracks parallel to the rolling plane which are typical on high strength steels [54] [55]. Fig. 4.22 shows the *J-R* curve for this specimen. Again,

the curve did not cross the offset line given by the ASTM E1820. Moreover, in this case, the *J* points are more dispersed than in the previous tests.
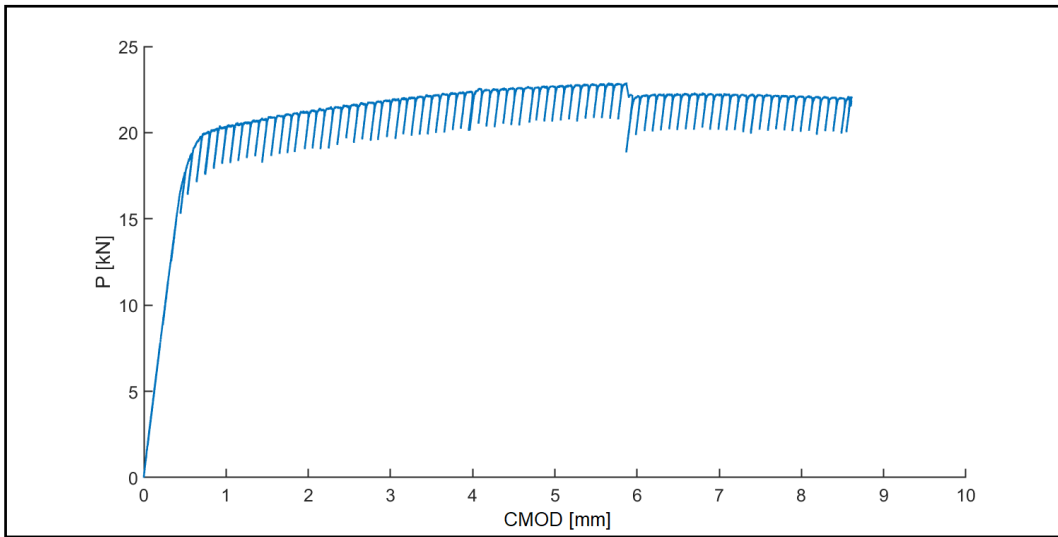
Figure 4.21: Unloading compliance SE(B)-4.

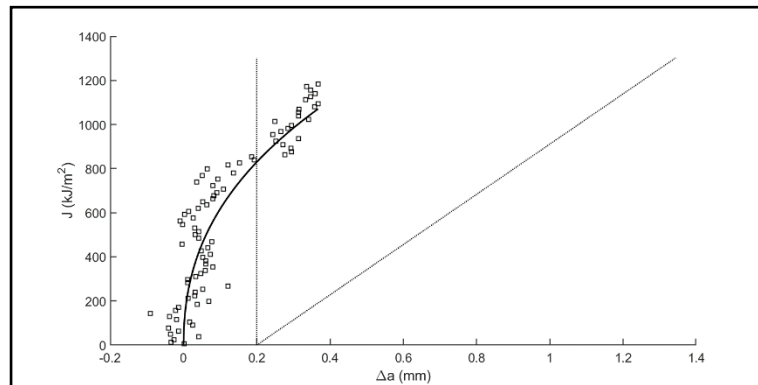Figure 4.22: *J-R* Curve SE(B)-4.

There were two more attempts with an *a/W* = 0.55 ratio without using the recommended side groove, but with the pre-crack propagated following the standard procedure. Fig. 4.23 illustrates the unloading compliance of SE(B)-5 and SE(B)-6. Figures 4.24 and 4.25 show the *J-R* curve of both specimens. Once again, the *J-R* curves did not cross the 0.2 mm offset line.
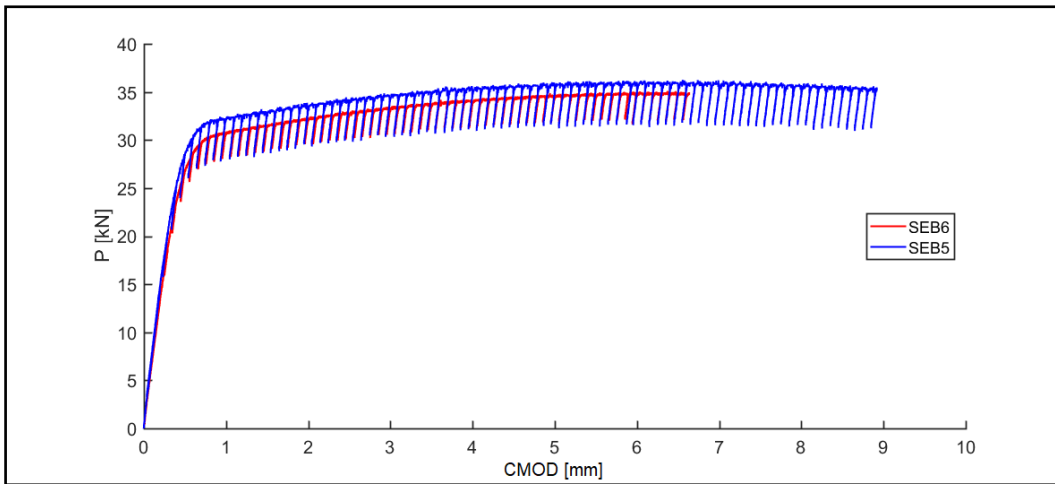
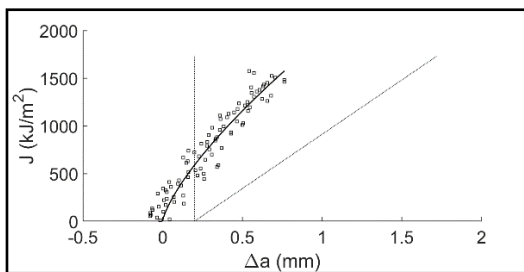Figure 4.23: Unloading compliance SE(B)-5 and SE(B)-6.

Figure 4.24: *J-R* Curve SE(B)-5.   Figure 4.25: *J-R* Curve SE(B)-6.
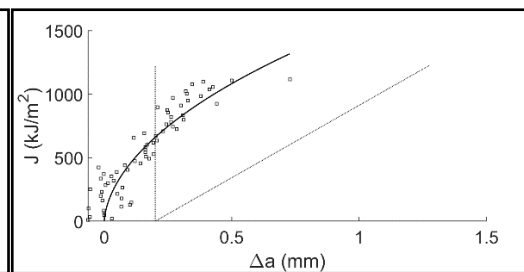
Specimen SE(B)-5 was also submerged in liquid nitrogen to induce brittle fracture, with the objective to do optical measurements on the crack faces. Figure 4.26 shows the crack extension in the shady area above the fatigue pre-crack located at the center. There was no crack tearing near the specimen surface during the experiment, which caused crack tunneling. Using the software *WebPlotDigitizer* with a reference scale in the picture, it is possible to perform an optical crack size measurement following the ASTM E1820 procedure. Dividing the crack into nine equally spaced points along with the thickness and giving some distance from the surface, the standard shows how to calculate the fatigue crack and the final physical crack. The crack size is the average of the 2 measured points near each surface combined with the remaining crack size points. The final physical crack measured is 9.87 mm.
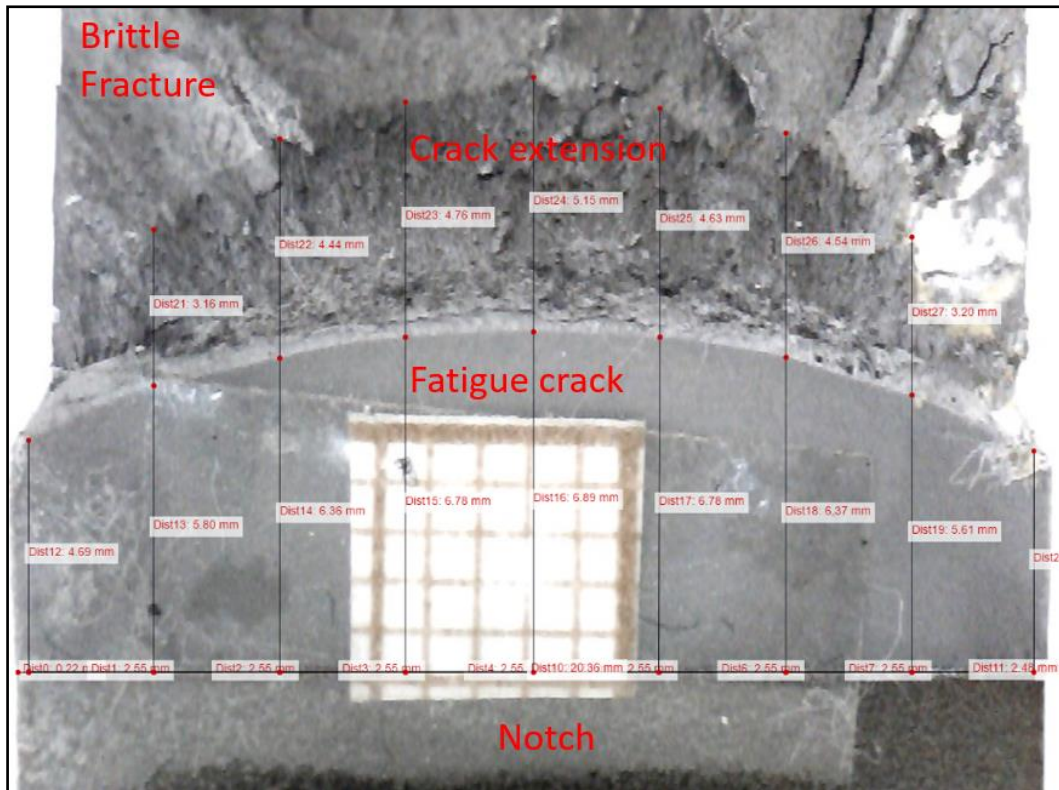
Figure 4.26: Fractography on SE(B)-5 specimen.

The ASTM E1820 says that none of the nine measurements shall differ by more than 0.05·B, which is approximately 1 mm. In this case, the optical crack measurement is not in agreement with the standardized procedure, so it is considered invalid. Unfortunately, this is the last broken specimen to expose the crack due to the availability of liquid nitrogen to execute this measurement.

The following experiments were on SE(B)-7 and SE(B)-8 with the same $a/W = 0.55$. The difference is that these specimens had side grooves to help to force a crack tearing phase. Figure 4.27 shows the unloading compliance measurements made in this configuration. Additionally, Fig. 4.28 and 4.29 show the corresponding *J-R* curves. In these cases, the *J-R* curves crossed the 0.2 offset line, but as shown in the figures, there were not enough points to measure J_{Ic} following the standard procedure.
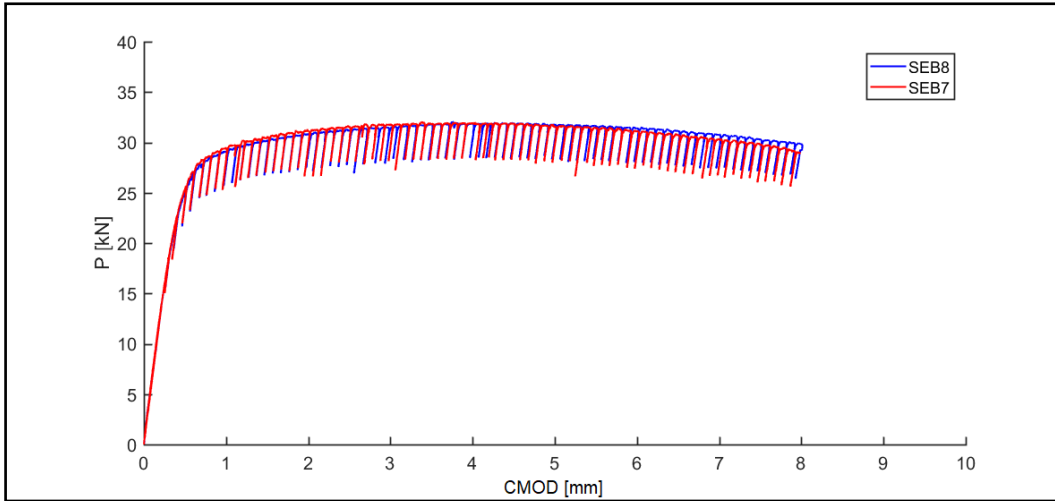
Figure 4.27: Unloading compliance SE(B)-7 and SE(B)-8.
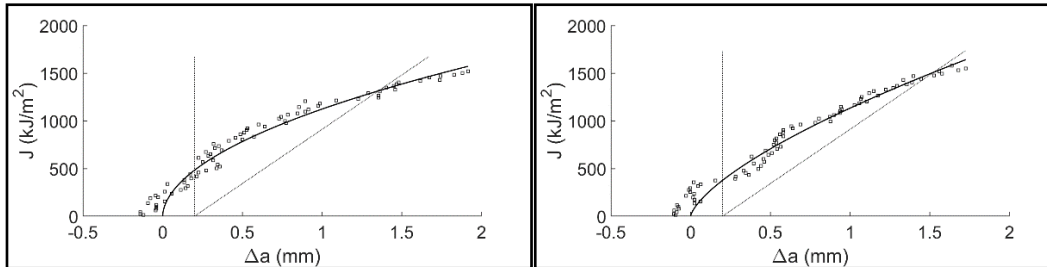
Figure 4.28: *J-R* Curve SE(B)-7.   Figure 4.29: *J-R* Curve SE(B)-8.

The last two toughness tests with SE(B)s were executed with *a/W = 0.3*. SE(B)-9 had side grooves, while SE(B)-10 had not. It was expected that the force in these experiments with lower *a/W* ratios would be around 100 kN. For precaution, these tests were performed using a 250kN MTS 810 servo-hydraulic testing machine, see Fig. 4.30. Figure 4.31 shows the unloading compliance of both specimens. As shown, parallel delamination occurred twice in the SE(B)-9 with side groove, while it did not happen in the SE(B)-10. Another detail is that because of the side groove, the loading on SE(B)-9 was slightly lower than the load needed to tear SE(B)-10. Figures 4.32 and 4.33 show the *J-R* curves of both specimens. Only the specimen with the side groove crossed the 0.2 mm offset line, and all the data points were not as dispersed like in the previous tests.

Figure 4.30: MTS 810 servo-hydraulic testing machine (250 kN).

Figure 4.31: Unloading compliance SE(B)-9 and SE(B)-10.

Figure 4.32: *J-R* Curve SE(B)-9.   Figure 4.33: *J-R* Curve SE(B)-10.

4.5.2
SE(T) specimens

The SE(T) tests were performed in an MTS 311.11 servo-hydraulic testing machine with a capacity of 1000 kN as demonstrated in Fig. 4.34. The
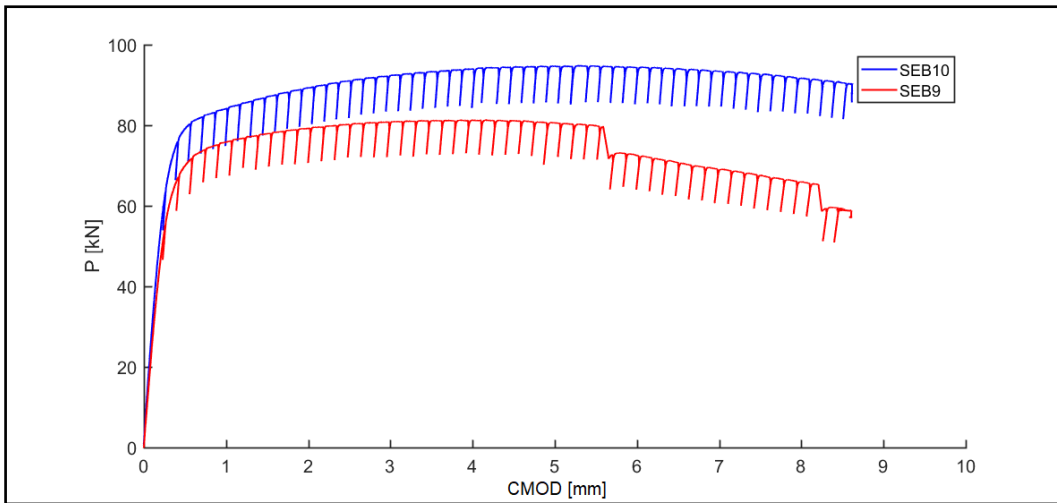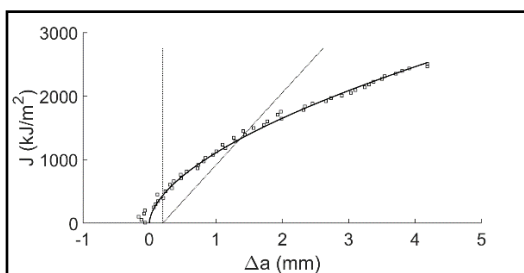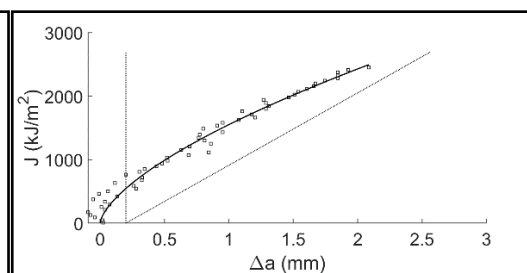
experiment was executed using a hydraulic wedge grip to clamp the specimens with H/W ratio equals 4. The CMOD measurement was done in the same way as the SE(B) experiments with two clip gages. Also, the tests were controlled manually by LLD to compare the results between both specimens. The *J-R* curve was developed following the Cravero and Ruggieri [21] procedure.

Figure 4.34: MTS 1000 kN servo-hydraulic testing machine.

The SE(T)-1 and SE(T)-2 have the precrack propagated with force higher than P_m (the same case as the initials SE(B) specimens). These two first specimens have an *a/W* ratio of 0.6. The SE(T)-1 was lost during the experiment due to the configuration of the machine. Fig. 4.35 shows the SE(T)-2 unloading compliance, where it has a maximum load of approximately 225 kN, which is more than seven times than the maximum load on SE(B). Also, once the load reaches the maximum, it starts dropping. A phenomenon that is not so visible on SE(B) specimens. The spaces between unloading were increased during the test to make it faster since the time available to operate the machine was limited. The first sequence of three unloading range was 30% of effective yield load (P_Y) given by Eq. 4-2, instead of 75% of P_m. Initially, the unloading force range was the same for SE(B), which were small compared to the curve. For this reason, from a certain point, the unloading range was 15% of the actual load.

$$P_Y = \sigma_Y b(W - a) \qquad (4-2)$$
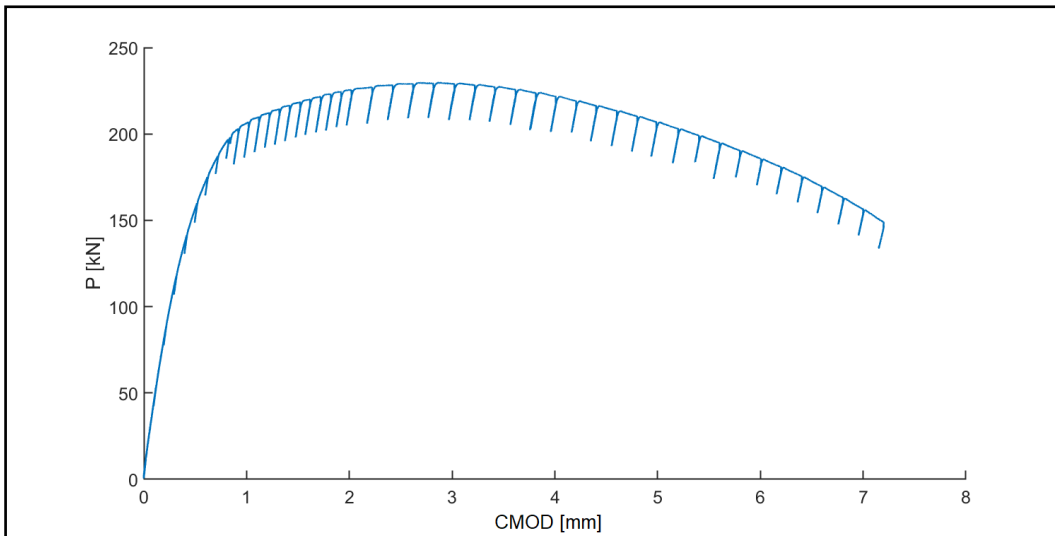
Figure 4.35: Unloading compliance SE(T)-2.

Fig. 4.36 shows the *J-R* curve using all the partial unloading to estimate crack increment given by this compliance. As demonstrated, the *J*-integral calculated from all the data points in the plot formed this kind of "S" shape (the square points in the plot). Doing the linear regression, including all the points, it generates an exponential resistance curve, which is illogical. The material resistance does not increase exponentially as the crack extension increases. Looking at this "S" shape, the values started to change direction when the spaces between the unloading increased during the experiment. With the intention to obtain a more reliable *J-R* curve, only the points before this curvature were assumed to develop the resistance curve. The *J* points after the beginning of the direction change were not considered. Thus, the outcome was that the data points indicated in Fig. 4.37, where the *J-R* curve came from a linear regression of these points. This curve is more similar to the expected resistance curve, and it crosses the offset line of 0.2 mm.
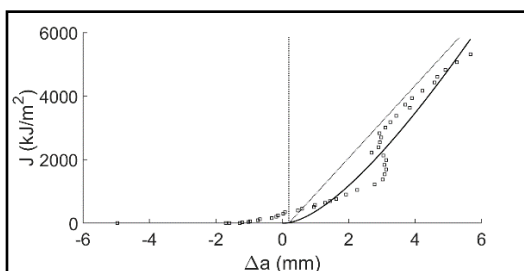
Figure 4.36: SE(T)-2 *J-R* original.   Figure 4.37: SE(T)-2 *J-R* adjusted.
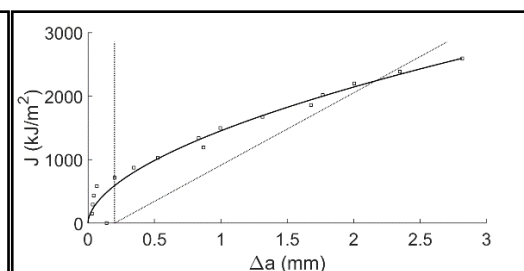
The SE(T)-3 had also the crack propagated with force higher than P_m that generated a *pz*. As an attempt to avoid the effect of that *pz*, the fatigue test continued in accordance with the standard to increase the crack length. The new *a/W* ratio of SE(T)-3 for the fracture toughness test is 0.65. The test started with a range of unloading force of 20% of the actual load. However, each unloading after 1 mm of CMOD came up with a hysteresis loop (see Fig. 4.38), and this would hinder the compliance estimation. Hence, the unload range was decreased during the experiment and the *J-R* curve given by this compliance is illustrated in Fig. 4.39. The *J* points calculated are very dispersed after a certain point resulting again in a power curve for the resistance curve. As an attempt to evaluate the material resistance, only the initials points were considered in the calculation of the *J-R* curve. Fig. 4.39 shows the result of this endeavor, where the curve crosses the 0.2 mm offset line with less than 100 kJ/m^2 contradicting the others test results. For this reason, this specimen test was considered invalid.
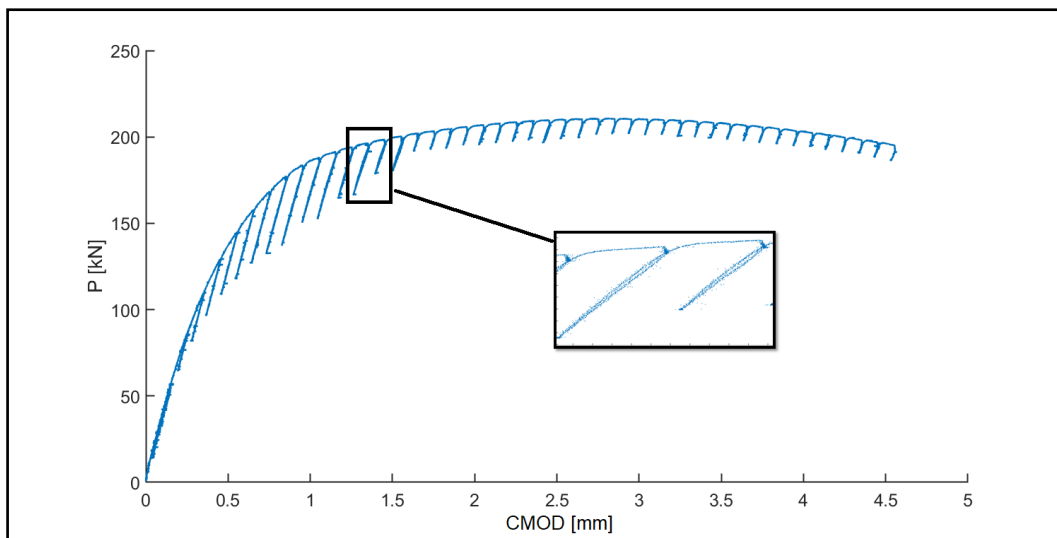
Figure 4.38: Unloading compliance SE(T)-3.
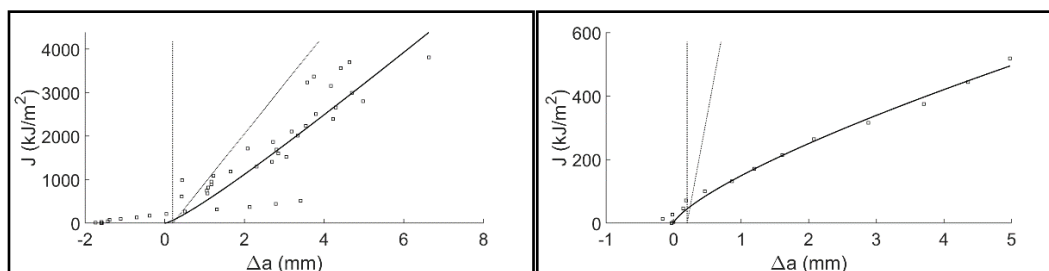
Figure 4.39: SE(T)-3 *J-R* original.   Figure 4.40: SE(T)-2 *J-R* adjusted.
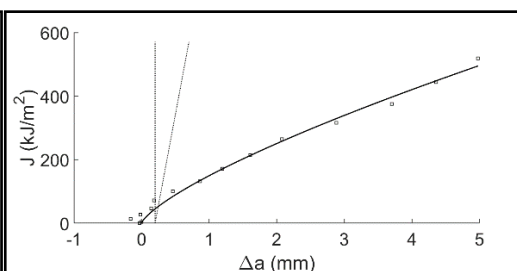
The SE(T)-4 was lost during the experiment due to unexpected malfunction. The SE(T)-5 has side groove and *a/W* ratio of 0.3. Fig. 4.41 shows the unloading compliance curve, which has an unloading range of 10% of the current load. The space between unloadings is 0.15 mm of CMOD. This time, it did not generate a hysteresis loop as on the previous experiment. Fig. 4.42 shows the *J-R* curve of this specimen. Only the first five initial points are dispersed compared with the majority. Because of that, they were neglected in the calculation of the resistance curve demonstrated in Fig. 4.43.
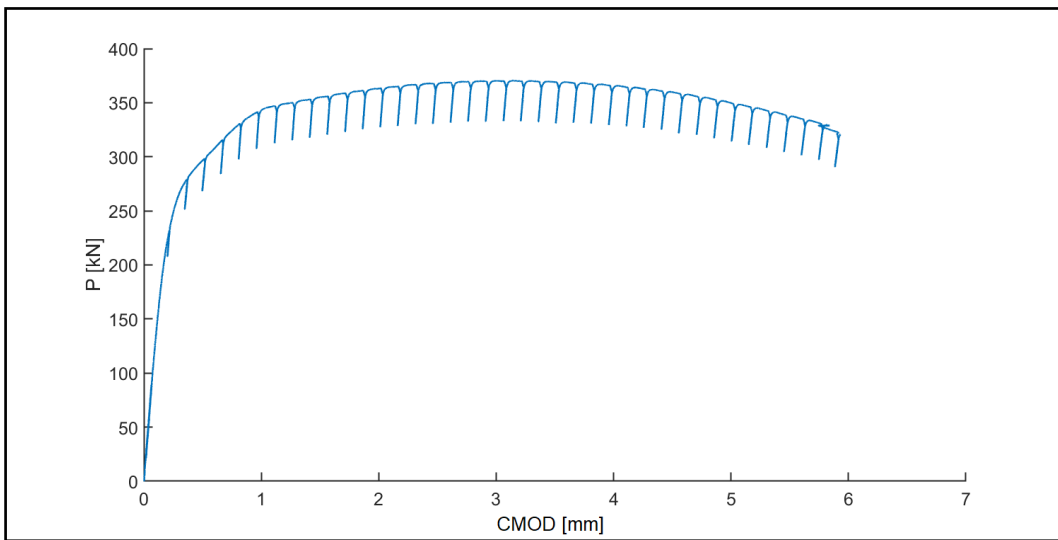
Figure 4.41: Unloading compliance SE(T)-5.
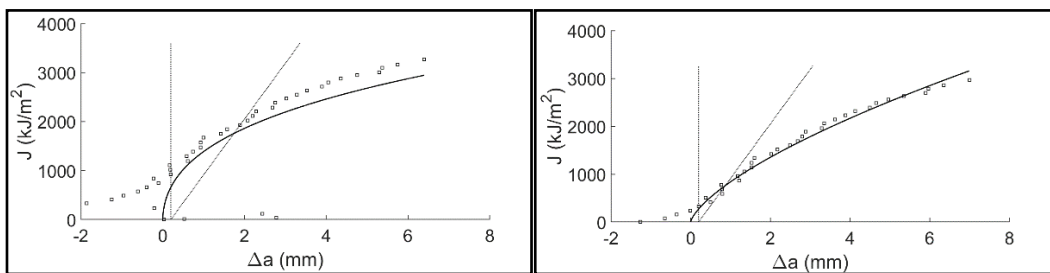
Figure 4.42: SE(T)-5 *J-R* original.   Figure 4.43: SE(T)-5 *J-R* adjusted.

The SE(T)-6 is a flat specimen with 0.3 *a/W* and was lost due to a data collection error. The SE(T)-7 has side groove and *a/W* ratio of 0.55. Fig. 4.44 shows the unloading compliance during the experiment. The unloading range and space between each unloading were the same as the previous experiment. Fig. 4.45 demonstrates the *J* points calculated using all the unloading

compliance points. Again, the resistance curve behaves as an exponential. As mentioned before, this can not be true. As an attempt to find a more reliable curve, it was considered only the points before the curvature at 3 mm of crack increment. Fig. 4.46 illustrates the resistance curve from these selected points. As demonstrated, the plot still represents something that does not comply with reality, so this test is considered invalid.
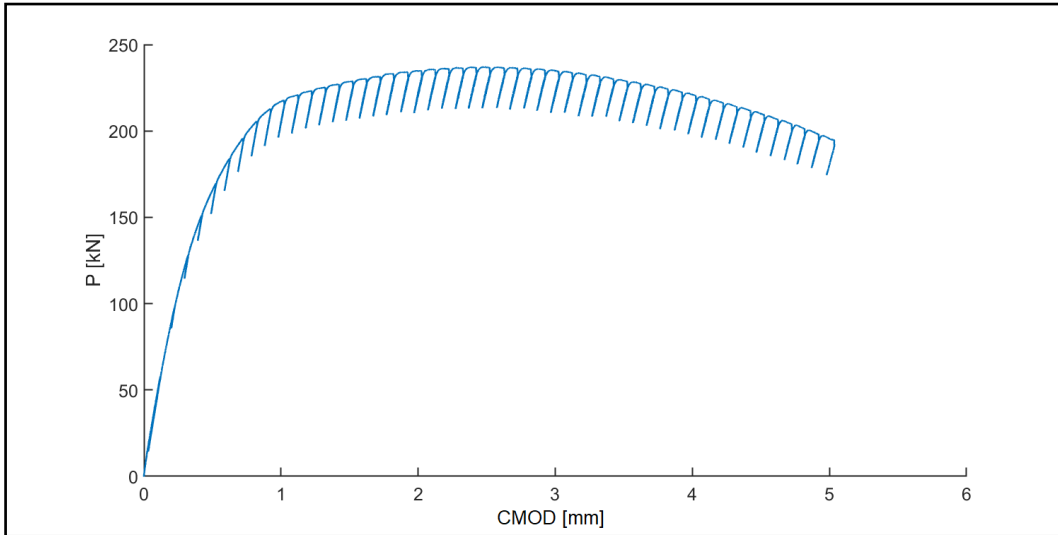
Figure 4.44: Unloading compliance SE(T)-7.
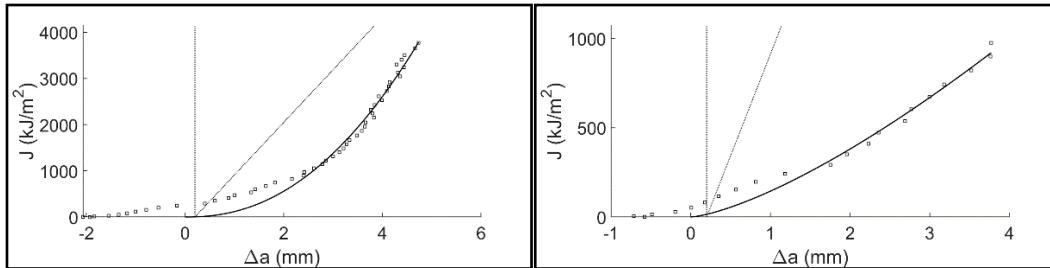
Figure 4.45: SE(T)-7 *J-R* original.   Figure 4.46: SE(T)-7 *J-R* adjusted.

The SE(T)-8 does not have a side groove, and the *a/W* ratio is the same as SE(T)-7. The objective of this experiment is to evaluate the side groove effect. Fig. 4.47 illustrates the unloading compliance obtained during the experimental test. It was used the same CMOD interval and load range of unloading as before. Fig. 4.48 shows the resistance curve generated using all the unloading from the compliance curve. The initial points were dispersed compared with the rest, so

this curve was adjusted to ignore these first points. Fig. 4.49 demonstrates the adjusted resistance curve.
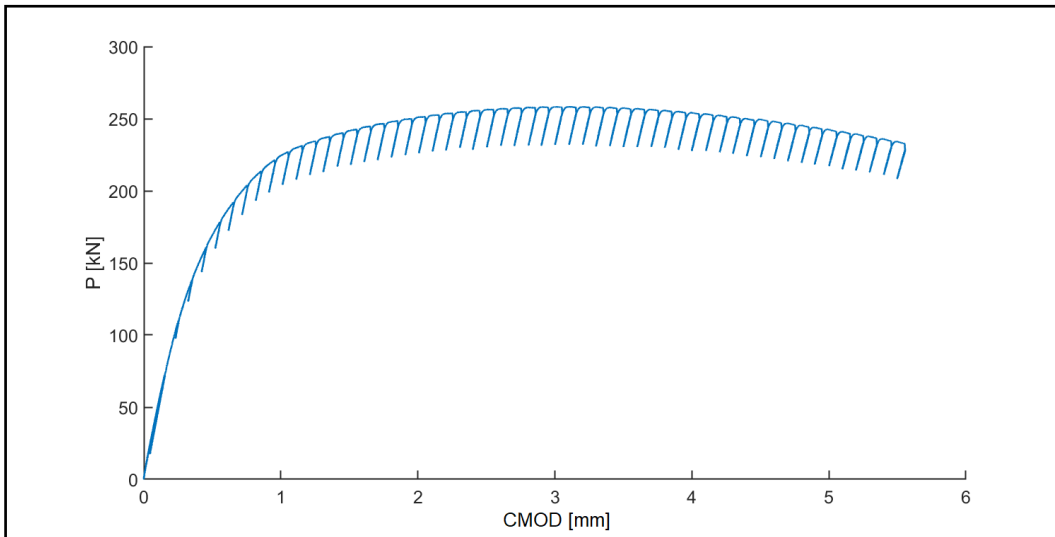
Figure 4.47: Unloading compliance SE(T)-8.
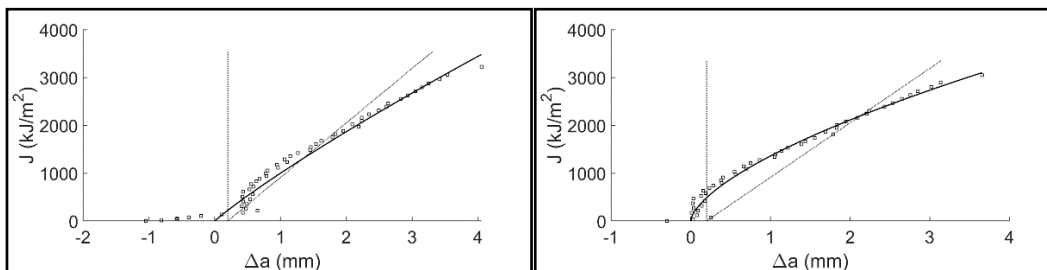
Figure 4.48: SE(T)-8 *J-R* original.   Figure 4.49: SE(T)-8 *J-R* adjusted.

As demonstrated, the ASTM E1820 criterion was not met to define fracture toughness J_{Ic}. The intersection with the offset line provided by the standard gives high values of J_{Ic}, which are not consistent. Austenitic steels specimens tend to defy size requirements to obtain valid resistance curves [56]. Using a Scanning Electron Microscope (SEM) is possible to measure the critical stretch zone width (Δa_{ic}) at the onset of stable ductile crack growth. For the API 5L X80 steel, the Δa_{ic} equals to 0.2 mm is considered to define an approximate value of fracture toughness J_{Ic} [57]. All the previous *J-R* curve plots illustrate a vertical line at 0.2 mm, indicating the intersection with resistance curve. This intersection corresponds to the assumed fracture toughness J_{Ic} in this work. All *J-R* curves are plotted following the Eq. 3-21, and the constant C_1 and C_2 are

shown in Tab. 4.5. Also, the critical K_{JIc} is estimated using Eq. 3-22. Moreover, the specimen with side grooves are denoted with SG.

Table 4.5: Fracture toughness properties measurements.

Specimen	a/W	C_1	C_2	J_{Ic} [kJ/m^2]	K_{JIc} [MPa$\sqrt{m}$]
SEB-1	0.55	x	x	x	x
SEB-2	0.55	1957 + 408i	0.57 + 0.09i	797.67	442.25
SEB-3	0.55	1507 + 261i	0.57 + 0.10i	608.7	386.22
SEB-4	0.65	1611 + 291i	0.42 + 0.11i	830.05	451.01
SEB-5	0.55	1917 + 137i	0.73 + 0.09i	588.58	380.13
SEB-6	0.55	1550 + 287i	0.53 +0.15i	660.29	402.42
SEB-7-SG	0.55	1123 - 1.86i	0.51 + 0.08i	482.35	344.68
SEB-8-SG	0.55	1133 - 4.26i	0.68 + 0.07i	375.78	304.11
SEB-9-SG	0.3	1105 - 41.1i	0.57 + 0.03i	435.13	326.96
SEB-10	0.3	1550 - 20.2i	0.64 + 0.05i	545.33	366
SET-1	0.55	x	x	x	x
SET-2	0.6	1452	0.56	589.9	380.21
SET-3*	0.65	149 - 5.71i	0.74 + 0.03i	44.85*	104.94*
SET-4	0.6	x	x	x	x
SET-5-SG	0.3	838 - 124i	0.67 + 0.10i	270.96	261.04
SET-6	0.3	x	x	x	x
SET-7-SG*	0.55	144 - 14.6i	1.39 + 0.08i	15.03*	61.15*
SET-8	0.55	1356 - 23.3i	0.63 + 0.02i	485.95	345.23

The imaginary part of the *J-R* curve results came from the linear regression approximation function ("*lsqcurvefit*") given by the software MATLAB. A possible reason that it resulted in complex numbers is that the linear analysis is not adequate to evaluate the experimental data obtained in this work. Even with the assumption to estimate J_{Ic} with the intersection of 0.2 mm vertical line, this material revealed high values of fracture toughness. Its K_{JIc} is above 250MPa for all specimens, with the exception of SET-3 and SET-7 (marked with an asterisk in the table), which were considered invalid tests. Only three SE(T)s specimens were considered valid, however, the measured fracture toughness was lower than the SE(B)s specimens for the same *a/W* ratio. This should be on the other way around since SE(T)s specimens have low constraints at the crack

tip. What could justify this result is that the SE(T)s specimens were slipping during the experimental procedure, which would influence the measurement. Also, the experiments were operated manually with LLD control that had a significant impact on the measurements, besides having a clip gage range limitation. Moreover, for the same *a/W*, specimens with side grooves had a lower J_{Ic} than the specimens with plane surface.

5.
Structural integrity assessments

With all the required properties measured, it is possible to evaluate critical loads that would cause failure in cracked components. There are standardized procedures to make such analyses, which have some amount of conservatism to guarantee safety. This chapter uses procedures of API 579 Fitness-for-Service guide [12]. This standard proposes structural integrity assessment procedures to consider crack-like flaw effects on tough structural components, considering three assessment levels with decreasingly conservative procedures. Since level 1 procedures are too conservative, predictions of critical loads are computed following for levels 2 and 3 only. Furthermore, experimental tests are executed to evaluate the actual conservatism of these assessments.

5.1
Structure configuration

The chosen structure is a flat plate with a through-wall crack flaw, which can approximate the behavior of pipelines [4] and is simpler to test, see Fig. 5.1 and 5.2. The plate has a thickness $B = 21.85$ mm, a width $2W = 100$ mm, and a through-wall crack with a length $2a = 70$ mm.
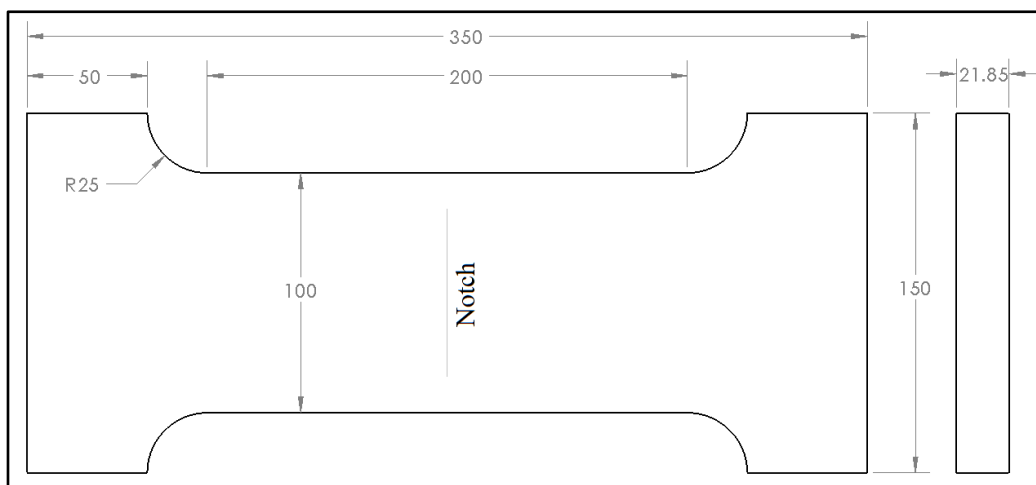
Figure 5.1: Specimen geometry.
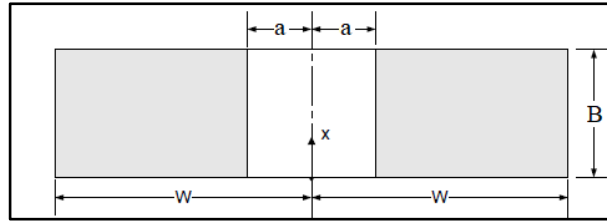
Figure 5.2: Plate with a through-wall crack [12].

5.2
Predictions by API 579 procedures

Level 1 procedures are straightforward, requiring only flaw dimensions and operating temperatures. If the crack size is below an admissible size, it is considered safe. Otherwise, it is necessary to use more accurate analyses specified in level 2. Figure 5.3 shows plots of admissible crack sizes, where the letters indicate how close the crack is to the weld. Moreover, the line type is for different ranges of crack size in relation to the structure thickness.
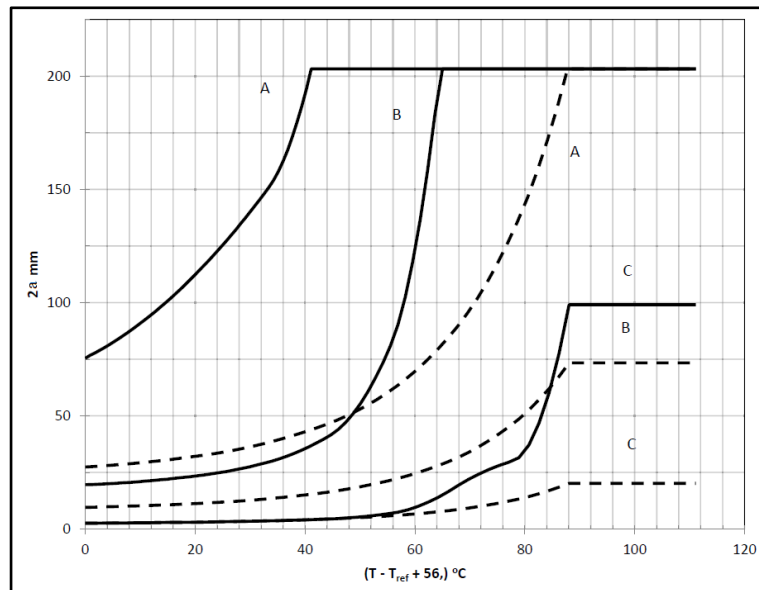
Figure 5.3: Level 1 admissible crack sizes for a flat plate [12].

5.2.1
Level 2 assessments

Level 2 procedures require some calculations and use Failure Analysis Diagrams (FAD), which consider brittle fracture and plastic collapse of the

cracked component. This approach is easy to implement since it only uses two parameters to solve a highly nonlinear problem, the toughness ratio K_r and the load ratio L_r. If the assessment point is below the curve shown in Fig. 5.4, then the component is considered safe. The type of failure is related to where the point falls in the plot. If K_r is high and L_r is low, it indicates a brittle failure, but if K_r is low and L_r is high, the failure mechanism is ductile overload [3].
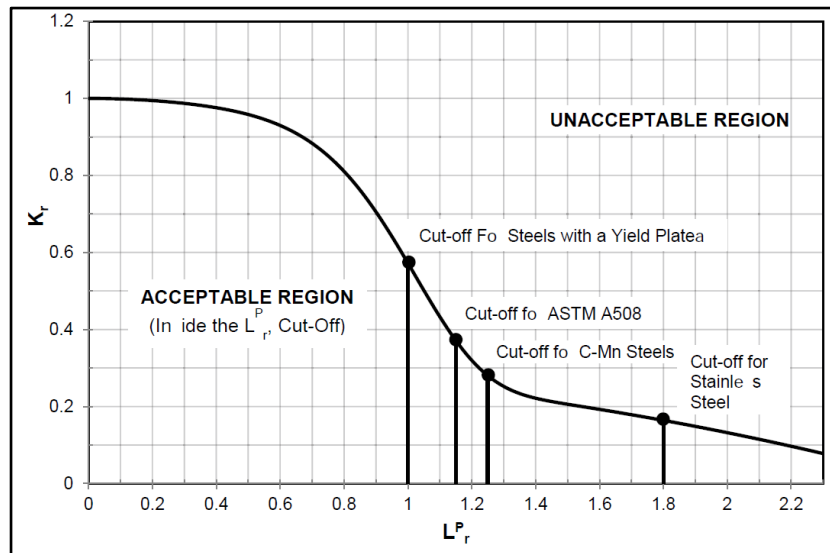
Figure 5.4: FAD level 2 specified in API 579 guide [12].

Structural integrity evaluations require information on loads, crack sizes, and material properties. The stresses applied to the structure can be classified as membrane σ_m or bending σ_b stresses and separated in primary, secondary, or residual components. Primary stresses in pressure vessels and pipes are load-controlled and secondary stresses are displacement-controlled [3]. Examples of secondary stress are thermal stresses and resident or residual stresses induced e.g. by welding or plastic strain gradients. Important material properties are the yield strength σ_{ys}, tensile strength σ_{us}, and fracture toughness K_{Ic}. All the properties used for the failure predictions made following have been properly measured, as studied in Chapter 4. Table 5.1 lists all the inputs used for the fracture assessments. The loadings σ_m and σ_b are assumed for calculation purposes but should be measured in practical applications. Moreover, the K_{Ic} value used in the following structural integrity evaluations is the average of the previously reported fracture toughness measurements K_{JIc}.

Table 5.1: FFS inputs.

σ_m	100	MPa
σ_b	0	MPa
σ_{ys}	527	MPa
σ_{us}	612	MPa
K_{Ic}	380	MPa$\sqrt{\text{m}}$
B	21.85	mm
a	35	mm
W	50	mm

Once these parameters are defined, the next step is to calculate the reference stress σ_{ref}, which combines σ_b, σ_m, and a/W effects. Equation 5-1 is the reference stress for a plate with through-wall crack specified in API 579.

$$\sigma_{ref} = \frac{\sigma_b + (\sigma_b^2 + 9\sigma_m^2)^{0.5}}{3(1 - a/W)} \tag{5-1}$$

In this case $\sigma_b = 0$, and for the initial analysis $\sigma_m = 100$ MPa, thus resulting in $\sigma_{ref} = 333$ MPa. L_r is given by the following equation:

$$L_r = \frac{\sigma_{ref}}{\sigma_{ys}} \tag{5-2}$$

which results in $L_r = 0.63$. The following step is to calculate the primary stress intensity factor K_I^P, which for this case can be found using Eq. 5-3.

$$K_I^P = (\sigma_m + M_b\sigma_b)\sqrt{\pi a}f_w \tag{5-3}$$

where M_b is a coefficient that depends on the crack length and plate thickness, and f_w is the finite width correction factor that can be obtained using Eq. 5-4.

$$f_w = \left(sec\left(\frac{\pi a}{2W}\right) \right)^{0.5} \tag{5-4}$$

hence $K_I^P = 49.2$ MPa$\sqrt{\text{m}}$. The next step would be to compute the plasticity interaction factor Φ to adjust the secondary and residual stress intensity factor K_I^{SR}, however, in this scenario $K_I^{SR} = 0$. Finally, K_r is given by:

$$K_r = \frac{K_I^P + \Phi K_I^{SR}}{K_{Ic}} \tag{5-5}$$

Therefore, $K_r = 0.13$. The final step is to find if this $\{K_r, L_r\}$ point is inside the safe area in the FAD diagram, see Fig. 5.5. Since the point is inside the FAD curve, this cracked component should not fail under $\sigma_m = 100$ MPa. Notice that the FAD stops at $1.25L_r$ for C-Mn steels.
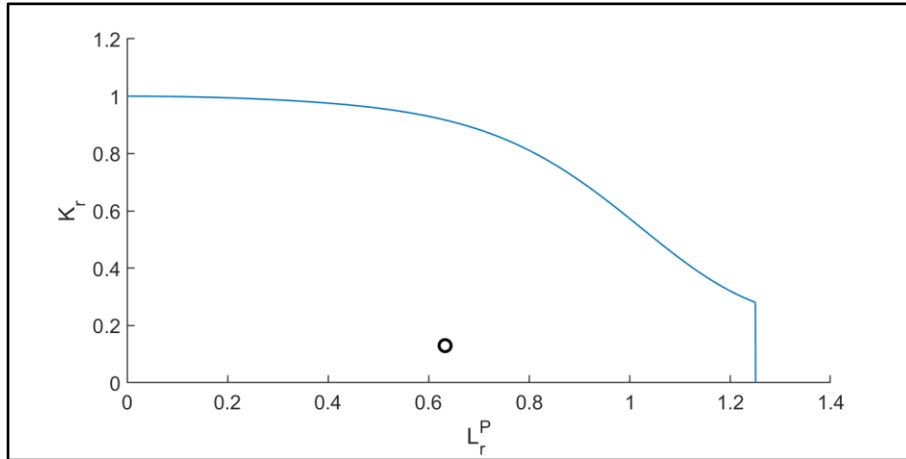
Figure 5.5: Failure analysis diagram level 2 for $\sigma_m = 100$MPa.

An iterative procedure is then used to find which stress would cause this component to fail, resulting in primary membrane stress $\sigma_m = 197.6$ MPa, see Fig. 5.6. Notice that the failure point is on the bottom right part of the FAD, implying in a plastic collapse type of failure.
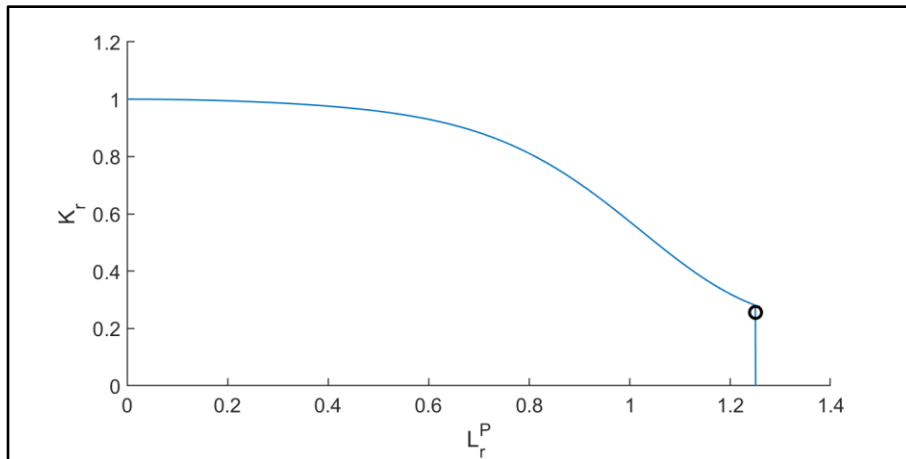
Figure 5.6: FAD level 2 to find the failure stress $\sigma_m = 197.6$ MPa.

5.2.2
Level 3 assessments

API 579 Level 3 procedures use the resistance curve of the material in ductile tearing analyses. Instead of checking only one point in the FAD as in Level 2, it uses several points for each crack depth increment, generating a resistance curve in the FAD. Failure will occur when this curve intersects the FAD limit, see Fig. 5.7.
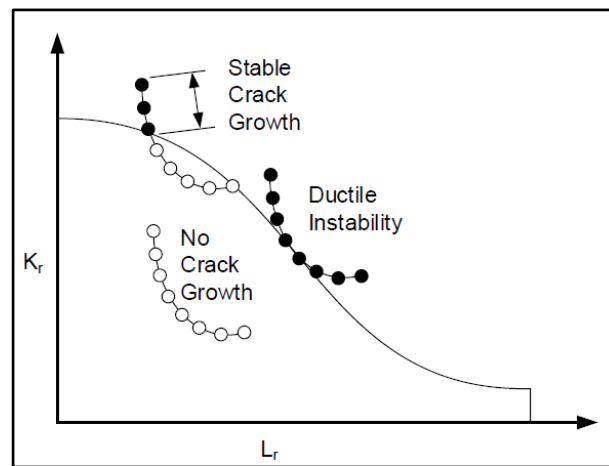
Figure 5.7: FAD level 3 [12].

Fig. 5.8 shows the level 3 assessment for SE(B)-8, which had the most accurately measured resistance curve. The load predicted by this method was also $\sigma_m = 197.6$ MPa, and it is on the bottom right part indicating a ductile type of failure.
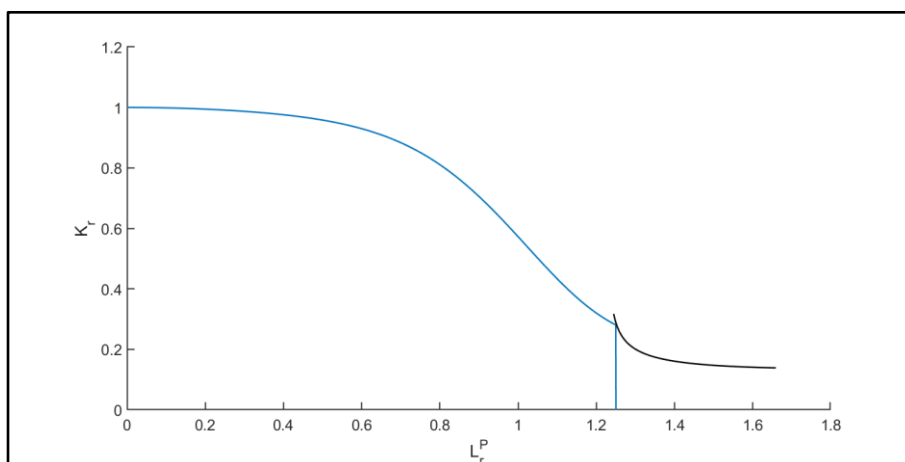
Figure 5.8: FAD level 3 for SE(B)-8, predicting failure under $\sigma_m = 197.6$ MPa.

5.2.3
Predictions results

Using the properties measured for each specimen, their estimated critical stresses are calculated according to API 579 Level 2 and 3 procedures, see Table 5.2. These predictions are on the bottom right of the FAD, which indicates a plastic collapse type of failure under the test conditions. Note that SE(T)-3 and 7 are invalid tests marked with an asterisk in this table.

Table 5.2: Predicted results.

| Specimen	*a/W*	Level 2 [MPa]	Level 3 [MPa]
SEB-1	0.55	x	x
SEB-2	0.55	197.6	197.6
SEB-3	0.55	197.6	197.6
SEB-4	0.65	197.6	197.6
SEB-5	0.55	197.6	197.6
SEB-6	0.55	197.6	197.6
SEB-7-SG	0.55	197.6	197.6
SEB-8-SG	0.55	191.5	196.7
SEB-9-SG	0.3	195	197
SEB-10	0.3	197.6	197.6
SET-1	0.55	x	x
SET-2	0.6	197.6	197.6
SET-3*	0.65	145*	165*
SET-4	0.6	x	x
SET-5-SG	0.3	185	194.5
SET-6	0.3	x	x
SET-7-SG*	0.55	110*	171*
SET-8	0.55	197.6	197.6

5.2.3
Validation tests

The testing machine used in this validation was the same one used for fracture toughness measurements on SE(T)s, a 1 MN MTS with LLD control. The specimen used is a plate with a through-wall crack in the middle illustrated in Fig. 5.1. To create the center notch, a small hole was machined in the middle of the specimen to pass the electrical discharge wire used to machine an EDM notch with 60 mm length across the specimen width. The idea is to propagate a fatigue pre-crack on both sides with 5 mm each, to have a final crack of 70 mm. To measure the pre-crack, the specimen was polished around the notch, see Fig. 5.9(a). The fatigue pre-cracking uses a loading cycle with a range of 14.5 to 145 kN at 5Hz, see Fig. 5.9(b), giving $a/W = 0.7$ and a thickness $B = 21.85$ mm.

5.9(a): Specimen.   5.9(b): Test setup.

Figure 5.9: Experiment.

Figure 5.10 shows Plate-1 load curve, with a peak load of 355 kN, which corresponds to maximum nominal stress $\sigma_n = 162$ MPa. Although due to time limits, the test was interrupted before the plate fracture, it was sufficient to obtain the maximum load it could sustain.

Figure 5.11 shows Plate-2 load curve, with a peak load of 262kN, which is far below than the expected value. This time, it was possible to perform the test until the fracture. The reason for this low load is that a fatigue crack initiated from what appears to be a scratch on the surface, instead of the notch tip. After the fracture, it was possible to see the crack shape, as shown in Fig. 5.12. The fatigue crack had a 2D ellipsoidal shape that was not identified during the pre-cracking phase. Only one side of the specimen was polished to measure the crack, and that was the size with the shorter crack size. On the other side, the

crack initiated from the scratch and propagated without being noticed, which makes this experiment invalid to validate the critical load predictions. Nevertheless, it is interesting to note that a brittle fracture did not occur at any moment during the test. The pre-cracked plate had a ductile tearing phase until the final separation in two parts as the plot shows.
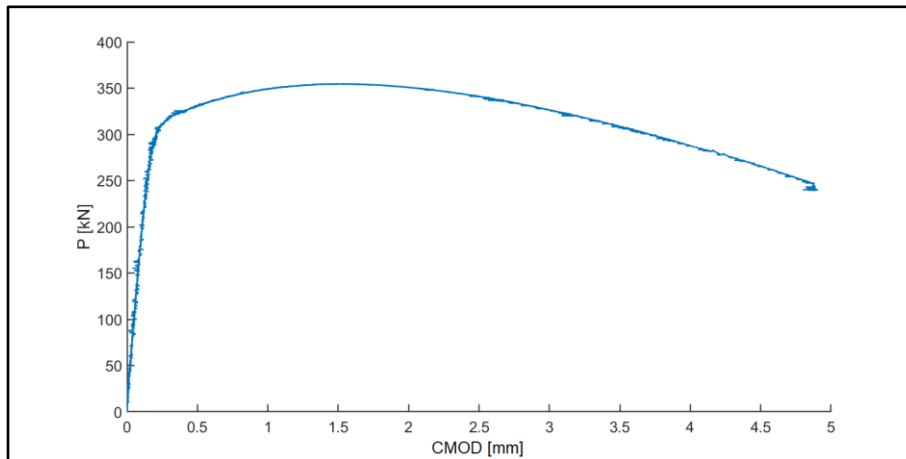
Figure 5.10: Plate 1 test.
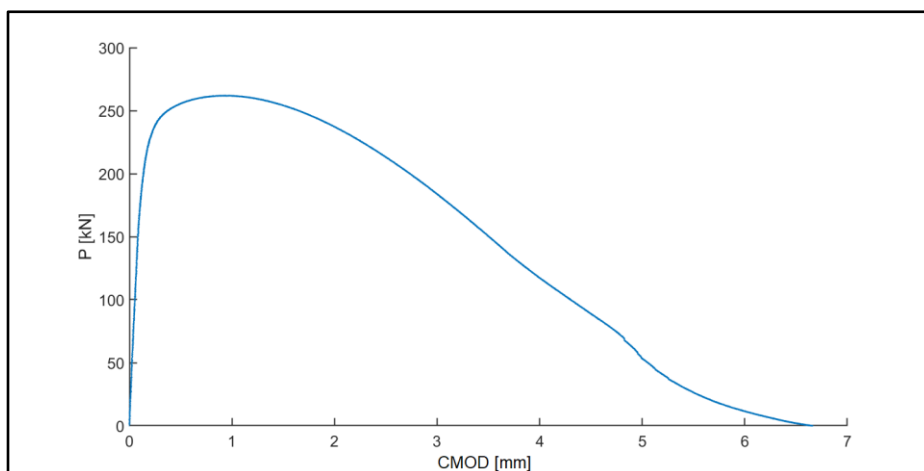
Figure 5.11: Plate 2 test.
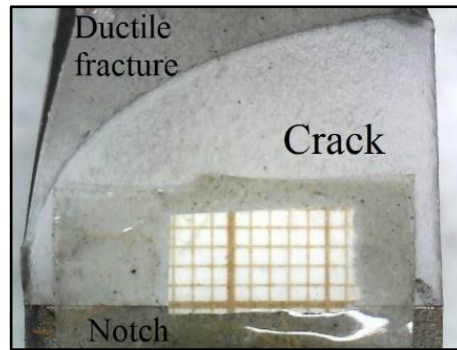
Figure 5.12: Ellipsoidal fatigue 2D pre-crack.

The critical stress predicted by API 579 procedures was 197.6MPa, about 22% higher than the peak stress sustained during this test, 162.4MPa. It should be lower than the measured critical load to guarantee safety, but in this case, the predictions were nonconservative due to the wrong assumption about the crack size, which was supposed shorter than it really was.

6.
Summary of results

6.1
Fracture toughness measurements on SE(B) specimens

Figure 6.1 shows the unloading compliance curves obtained in the tests of all SE(B) specimens. Additionally, Fig. 6.2 illustrates the *J-R* curves computed by ASTM E1820 procedures without the experimental data points.
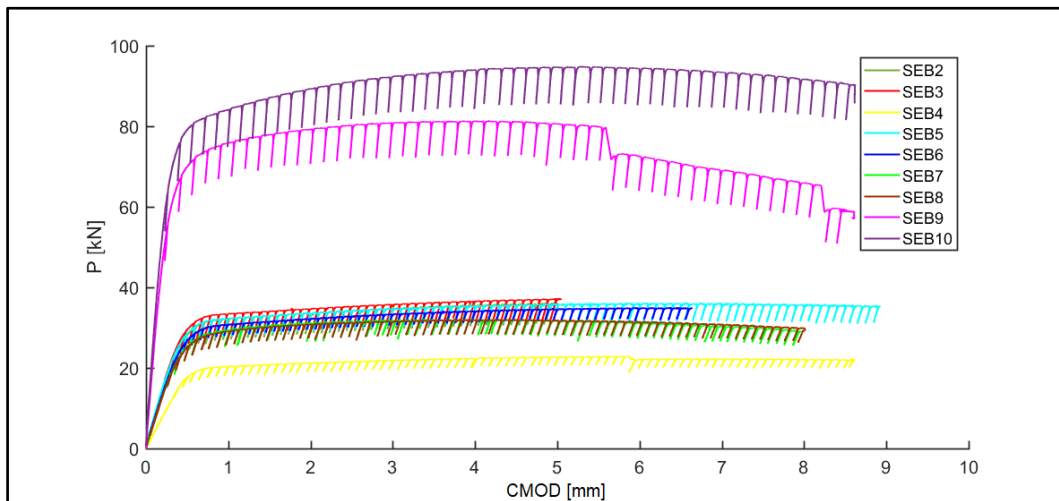
Figure 6.1: Unloading compliance curves of all SE(B) specimens.
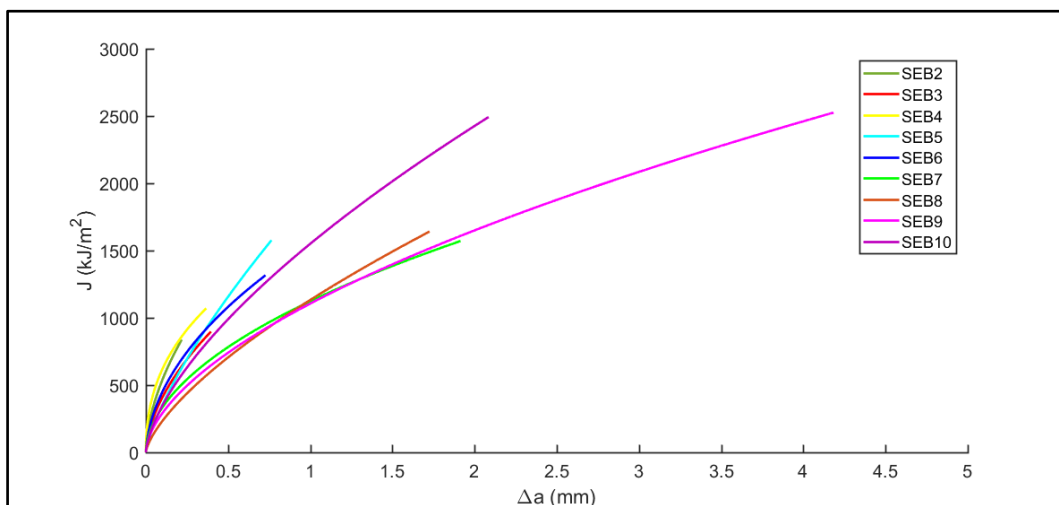
Figure 6.2: *J-R* curves of all SE(B) specimens.

6.2
Fracture toughness measurement on SE(T) specimens

Figure 6.3 shows the compliance curves measured on the tests of all SE(T) specimens and Fig. 6.4 shows their *J-R* curves computed following Cravero and Ruggieri [21] procedure.
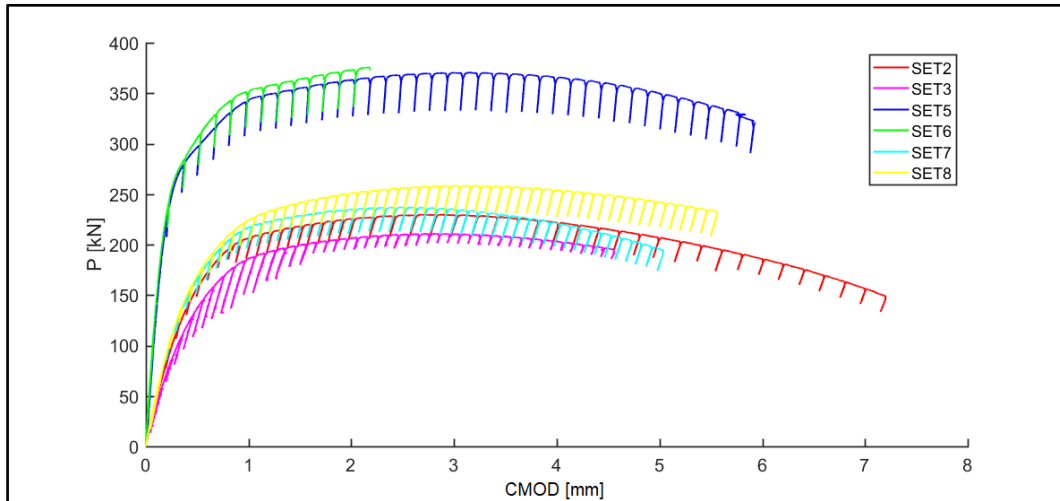
Figure 6.3: Unloading compliance curves of all SE(T) specimens.
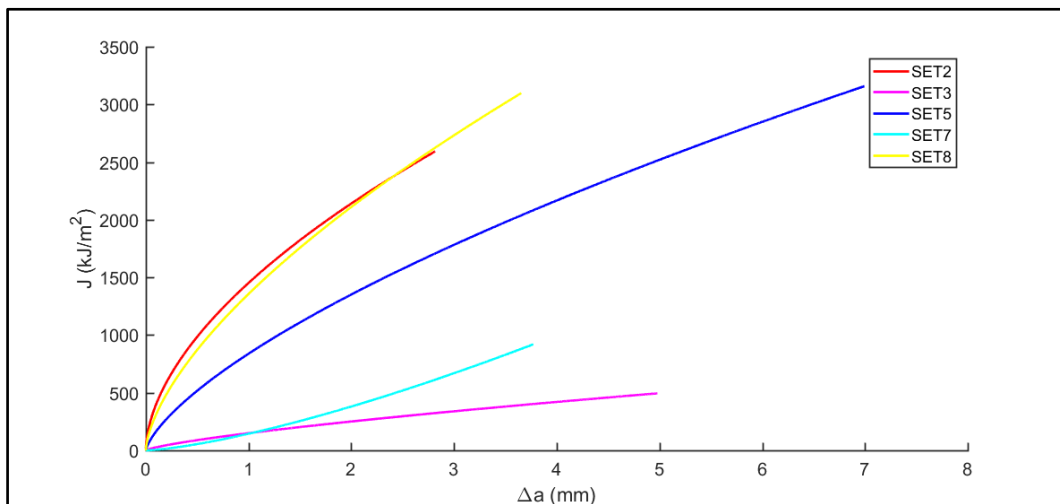
Figure 6.4: *J-R* curves of all SE(T) specimens.

6.3
Failure predictions

Figure 6.5 shows the predictions using the properties of all the specimens on the FAD following API 579 level 2 procedures. The majority of the results are located on the bottom right corner of the FAD. Only the specimens SE(T)-3, 5, and 7 are separated from the others, but SE(T) 3 and 7 tests yielded invalid results. Furthermore, Fig. 6.6 shows the predictions using the properties of all specimens on the FAD following API 579 level 3 procedures.
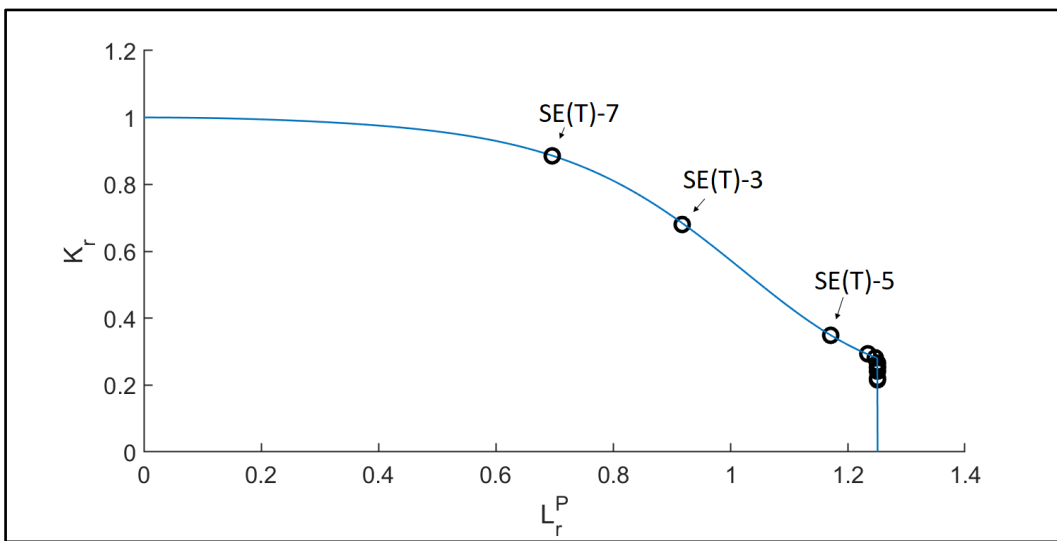
Figure 6.5: FAD – API 579 level 2 predictions.
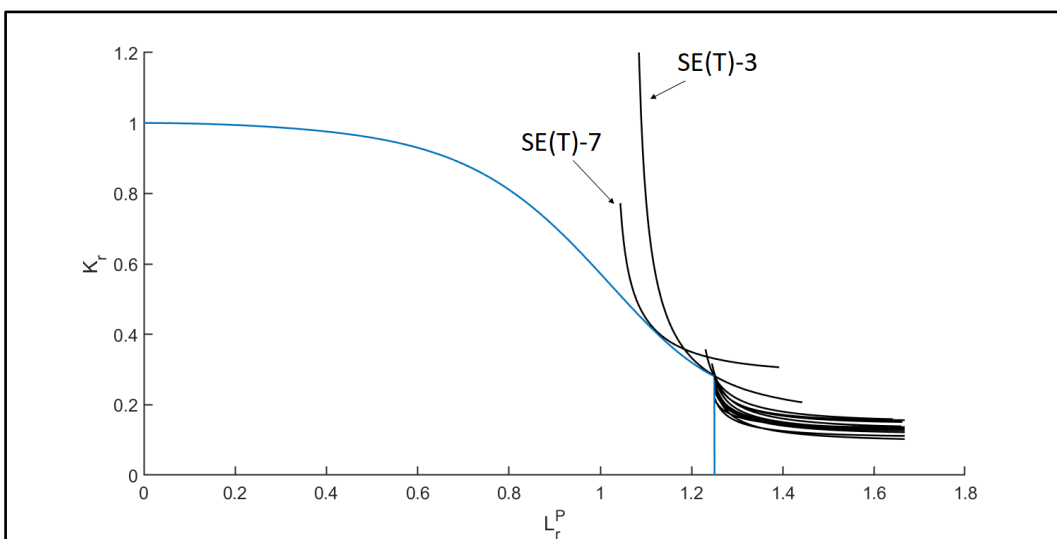
Figure 6.6: FAD – API 579 level 3 predictions.

7.
Conclusions

This work presents fracture toughness measurements on API 5L X80 steel SE(B) and SE(T) specimens, and compute failure predictions by standard API 579 procedures using the measured properties. Finally, suitable tests are used to validate the predicted critical loads.

7.1
Conclusions from the fracture toughness measurements

Fracture toughness tests on SE(B) specimens followed standard ASTM E1820 procedures [7], whereas alternative toughness tests on SE(T) specimens used procedures proposed by Cravero and Ruggieri [21]. The specimens had different a/W ratios to evaluate the influence of crack size on the measurements. Moreover, some specimens had side grooves to assess how they affect the results. The experimental tests lead to the following conclusions:

- The API 5L X80 steel revealed high values of fracture toughness, which made infeasible to measure the resistance curve following procedures of the appendix A9 of the ASTM E1820. Therefore, all J points given by the elastic compliance calculation were considered to develop the J-R curve. This work used the critical stretch zone width ($\varDelta a_{ic}$) as a parameter to measure fracture toughness J_{Ic} [57]. The intersection of the measured resistance curve with a vertical line at $\varDelta a_{ic} = 0.2$ mm gives an approximate value of J_{Ic}.

- All experiments were operated manually with Load Line Displacement (LLD) control. Besides the initials test, it was used two clip gages to obtain the maximum available CMOD range of 9 mm, instead of the recommended 12 mm. The RANSAC method was used to calculate the compliance from the data point since it is more robust than the least square method. All tests reached the maximum clip gage capacity without having a brittle fracture.

- In this work, the optical crack measurement is not in agreement with the standardized procedure due to the notable crack front curvature. It was possible to see the crack extension of only one specimen (SE(B)-5), because of the availability of liquid nitrogen to induce brittle fracture. In this specimen, there was no crack tearing near the specimen surface, causing crack tunneling due to high stress triaxiality at the center section, promoting void nucleation, growth, and coalescence [53].

- All *J-R* curves from SE(T) specimens had to be adjusted because of the scattered *J* points obtained from the compliance. The adjustment is made by not considering the points that were dispersed compared with the rest. The dispersion can be justified due to the use of LLD control, that is affected by the machine flexibility and oscillations in the hydraulic actuator, making the crack increment (Δa) measurement inaccurate. Another possible reason is that the specimen slipped during the experiment. One recommendation to avoid slippage of SE(T) specimens at the grip area is to rotate the specimen position by 90° considering the center axis along the length. Then the grip area would be along with the thickness, instead of the width.

- For the same *a/W* ratio, specimens with side grooves have a *J-R* curve lower than the flat specimen. In effect that they have more constraints and a predominant plane strain state. Also, the data points from these specimens were not as dispersed like the others.

- Formation of splits (parallel delamination) may happen in specimens with a high constraint that causes pop-in during the experiments, as occurred on SE(B)-4 and 9 specimens. Splits may increase material resistance against crack propagation since it can change the stress field from plane strain to plane stress, which requires more energy to propagate the crack. On the other hand, splits also reduce the transversal section that reduces the resistance against plastic collapse [58]. In this situation, the A4 appendix of the ASTM E1820 provides procedures on how to assess these pop-ins for compliance calculation.

- As expected, the SE(T) specimens were able to support higher loads than the SE(B) specimens. Also, once the load reaches the maximum for SE(T) specimens, it starts dropping. A phenomenon that did not occur on SE(B) specimens.

7.2
Conclusions from the failure predictions

Failure predictions followed procedures of the API 579 [12] levels 2 and 3 using the properties measured for each specimen. Moreover, the results were compared with experimental tests using a plate specimen with a through-wall crack in the middle.

- Most of the predictions are the same for level 2 and 3 of the API 579 since the toughness ratio and load ratio point $\{K_r, L_r\}$ are located on the bottom right of the Failure Analysis Diagram (FAD), which indicates ductile failure. In this work, the API 5L X80 steel failure mechanism is plastic collapse.

- Only two tests were performed, which one was considered invalid since the fatigue crack initiated from a scratch on the surface instead of the notch tip. Because of that, the crack size used for the predictions is different from the crack at the specimen. Even with *a/W* ratio of 0.70, brittle fracture did not occur at any moment during the experiment. The pre-cracked plate had a ductile tearing phase until the final separation in two parts.

- All predictions following the API 579 procedure were higher than the maximum stress obtained from the experiment, resulting in nonconservative predictions. A possible reason for that is due to inaccurate properties measurement. Another is the chosen FAD is not adequate for high toughness materials. It is worth noting that only one valid experiment was executed to make this evaluation, which is not recommended. Unfortunately, it was not possible to perform more tests due to time limit.

- On FAD level 2 and 3 only the prediction using SET-5 ($a/W = 0.30$) properties is separated from the other predictions. All predictions using SE(B) measurements have approximately the same result.

- As discussed, the API 5L X80 is very suitable steel for pipelines which can withstand cracks in the base metal. Therefore, the critical region that could occur fracture is at the welding section.

7.3
Recommendations for future work

- Measure the fracture toughness on C(T) specimens to compare with the *J-R* curve results from SE(B).

- Execute more experiments with cracked plates to evaluate the predictions made by the API 579 standard.

- Apply the structural integrity procedure on the welding and evaluate the effect of the heat-affected zone (HAZ).

Bibliography

[1]   BROEK, D. **Elementary engineering fracture mechanics**, Springer Science and Business Media, 2012.

[2]   HERTZBERG, R.W. **Deformation and fracture mechanics of engineering materials**, Wiley, 1989.

[3]   ANDERSON, T.L. **Fracture mechanics:** fundamentals and applications, CRC press, 2017.

[4]   CASTRO, J.T.P.D.; MEGGIOLARO, M.A. **Fadiga:** técnicas e práticas de dimensionamento estrutural sob cargas reais de serviço: Volume I,II, CreateSpace, 2009.

[5]   ASTM E399, **Standard Test Method for Linear-Elastic Plane-Strain Fracture Toughness KIC of Metallic Materials**, 2012.

[6]   ASTM E1290, **Standard Test Method for Crack-Tip Opening Displacement (CTOD) Fracture Toughness Measurement**, 2008.

[7]   ASTM E1820-17a, **Standard test method for measurement of fracture toughness**, 2017.

[8]   BS 7448, **Fracture Mechanics Toughness Tests. Method for Determination of Kic, Critical CTOD and Critical J Values of Metallic Materials**, ISE British Standard, 1991.

[9]   GKSS-RESEARCH, **The GKSS Procedure for Determining the Fracture Behavior of Materials**., EFAM-GTP 02, 2002.

[10] LINK, R.E. **Round-robin Analysis of Standard Data Sets for Fracture Toughness Evaluation in ASTM E1820**, Journal of Testing and Evaluation, 2014.

[11] VERITAS, N. D. **Fracture control for pipeline installation methods introducing cyclic plastic strain**, Recommended Practice DNV-RP-F108, 2006.

[12] API 579-1/ASME FFS-1, **Fitness-For-Service guide**, 2016.

[13] HARRISON, R.; LOOSEMORE, K.; MILINE, I. **Assessment of the integrity of structure containing defects**, Int. J. Pressure Vessel and Piping, 1988.

[14] DILLSTRÖM, P.; BERGMAN, M. **A combined deterministic and probabilistic procedure for safety assessment of components with cracks--Handbook**, SSM report, 2008.

[15] WALLIN, K.; NEVASMAA, P. **Structural Integrity Assessment Procedures for European Industry (SINTAP)**, Sub-Task, 1997.

[16] BS 7910, **Guide to methods for assessing the acceptability of flaws in metallic structures**, British Standard and others, 2015.

[17] **Umm Said LPG Plant Disaster**, [Online]. Available: <https://pt.scribd.com/doc/21090127/UMM-Said-LPG-Plant-Disaster-03-04-77>.

[18] **Alexander L. Kielland platform capsize accident–investigation**, [Online]. Available: <https://officerofthewatch.com/2013/04/29/alexander-l-kielland-platform-capsize-accident>.

[19] **SS Schenectady**, [Online]. Available: <https://en.wikipedia.org/wiki/SS-Schenectady/>.

[20] **Common Comet Misconceptions and Collaborative Contribution to Safety**, [Online].Available: <http://aerossurance.com/safety-management / comet-misconceptions/>.

[21] CRAVERO S.; RUGGIERI, C. **Estimation procedure of J-resistance curves for SE (T) fracture specimens using unloading compliance**, Engineering Fracture Mechanics, 2007.

[22] PEDROSA, I.R.V. et al. **Study of phase transformations In API 5L X80 Steel in order to increase its fracture toughness**, Materials Research, 2013.

[23] BHADESHIA, H.; HONEYCOMBE, R. **Steels:** microstructure and properties, 2017.

[24] ASTM E8/E8M - 16a, **Standard Test Methods for Tension Testing of Metallic Materials**, 2016.

[25] LIU, A.F. **Mechanics and mechanisms of fracture:** an introduction, ASM International, 2005.

[26] HANDROK, J.L.; COMER, J.J.; BANNANTINE, J.A. **Fundamentals of Metal Fatigue Analysis**, Prentice Hall, 1990

[27] CHEN, R.C.J.H. **Micromechanism of Cleavage Fracture of Metals**, Elsevier Inc., 2015.

[28] MEDINA, J.A.H. **Avaliação de Previsões de Fraturas Elastoplásticas**, PUC-Rio, 2014.

[29] MAITI, S. K. **Fracture Mechanics**, Cambridge University Press, 2015.

[30] BURDEKIN, F.; DAWES, M. **Practical use of linear elastic and yielding fracture mechanics with particular reference to pressure**

vessels, Proceedings of the Institute of Mechanical Engineers Conference, 1971.

[31] HUTCHINSON, J. **Singular behaviour at the end of a tensile crack in a hardening material**, Journal of the Mechanics and Physics of Solids, 1968.

[32] RICE, J. **Plane strain deformation near a crack tip in a power-law hardening material**, Journal of the Mechanics and Physics of Solids, 1968.

[33] KIRK, M. T.; KOPPENHOEFER, K. C.; SHIH, C. F. **Effect of constraint on specimen dimensions needed to obtain structurally relevant toughness measures**, Constraint effects in fracture, 1993.

[34] SHIH, C.; GERMAN, M. **Requirements for a one parameter characterization of crack tip fields by the HRR singularity**, International Journal of Fracture, 1981.

[35] BETEGON, C.; HANCOCK, J. **Two-parameter characterization of elastic-plastic crack-tip fields**, Journal of applied mechanics, 1991.

[36] O'DOWD, N.; SHIH, C. F. **Family of crack-tip fields characterized by a triaxiality parameter**—I. Structure of fields, Journal of the Mechanics and Physics of Solids, 1991.

[37] O'DOWD, N.; SHIH, C. F. **Family of crack-tip fields characterized by a triaxiality parameter**—II. Fracture applications, Journal of the Mechanics and Physics of Solids, 1992.

[38] SHEN, G. et al. **Measurement of JR curves using single-specimen technique on clamped SE (T) specimens**, The Nineteenth International Offshore and Polar Engineering Conference, 2009.

[39] KANG, J. et al. **Influence of Constraint on J-resistance Curves for an X100 Pipe Steel**, Procedia materials science, 2014.

[40] CHIESA, M. et al. **Efficient fracture assessment of pipelines. A constraint-corrected SENT specimen approach**, Engineering Fracture Mechanics, 2001.

[41] WILLIAMS, M. L. **The bending stress distribution at the base of a stationary crack**, Journal of applied mechanics, 1961.

[42] YASUFUMI, I.; TOMOKAZU, M. **Effect of side grooves on the elastic-plastic stress state of fracture toughness specimens—three-dimensional finite element analysis**, Engineering Fracture Mechanics, 1982.

[43] ANDREWS, W.; SHIH, C. **Thickness and side-groove effects on J-and δ-resistance curves for A533-B steel at 93° C**, Elastic-plastic fracture, 1979.

[44] JOYCE, J.A. **Manual on elastic-plastic fracture:** laboratory text procedures, 1996.

[45] SHEN, G.; GIANETTO, J.; TYSON, W. **Development of procedure for low-constraint toughness testing using a single-specimen technique**, CANMET Materials Technology Laboratory, Technical Report, 2008.

[46] CIRINO, J. et al. **Caracterização microestrutural do aço API 5L X80 em amostras sumetidas a diferentes ataques quimicos**.

[47] ZHOU, M. et al. **Microstructure characteristics and mechanical properties of X80 pipeline steels**, Journal of Wuhan University of Technology-Mater. Sci. Ed., 2012.

[48] USIMINAS; CONFAB; PETROBRÁS; CEFET-RJ; PUC-RJ, **Estudos de aplicações do aço x80 para tubos**, Programa Nacional de Ciência e

Tecnologia do Setor de Petróleo e Gás Natural – CTPETRO: Projeto cooperativo Universidade-Empresa, 2002.

[49] AMERICAN PETROLEUM INSTITUTE, **API5L Specification for line pipe steel**, 43th, 2004.

[50] DIN 50150, **Conversion of hardness values for metallic materials**, 2000.

[51] JOO, M. S. et al. **Mechanical anisotropy in steels for pipelines**, ISIJ international, 2013.

[52] FISCHLER, M.; BOLLES, R. **Random sample consensus: a paradigm for model fitting with applications to image analysis and automated cartography**, Commum ACM, 24:381, 1981.

[53] LAN, W.; DENG, X.; SUTTON, M.A. **Investigation of crack tunneling in ductile materials, Engineering Fracture Mechanics**, 2010.

[54] ARNOULT, X. et al. **Short review:** Potential impact of delamination cracks on fracture toughness of structural materials, Frattura ed Integrita Strutturale, 2016.

[55] SILVA, M.D.C. **Caracterização das propriedades mecânicas e metaúrgicas do aço API 5L X80 e determinação experimental de curvas JR para avaliação da tenacidade a fratura**, 2016.

[56] SCHWALBE, K.H.; CORNEC, A.; BAUSTIAN, K. **Application of fracture mechanics Principles to austenitic steels**, International journal of pressure vessels and piping, 1996.

[57] ZHU, X.K.; LEIS, B.N. **Application of constraint corrected JR curves to fracture analysis of pipelines**, Journal of Pressure Vessel Technology, 2006.

[58] HIPPERT JUNIOR, E. **Investigação expeirmental do comportamento dúctiol de aços API-x70 e aplicação de curvas de resitência J-Δa para previsão de colapso em dutos**, Escola Politécnica, Universidade de São Paulo, 2004.